Review

SURFACE and INTERFACE ANALYSIS

Received: 7 January 2008 Accepted: 7 March 2008 Published online in Wiley Interscience:

(www.interscience.com) DOI 10.1002/sia.2902

Atomic-level characterization of materials with core- and valence-level photoemission: basic phenomena and future directions

Charles S. Fadley[a,b]*

In this overview, the basic concepts of core and valence photoelectron spectroscopy (photoemission), photoelectron diffraction, and photoelectron holography are introduced. Then some current developments in these techniques that should enhance their utility for atomic-level characterization of new materials and surface chemical processes are discussed, including measurements with hard X-ray excitation, standing-wave excitation, and ambient pressures in the multi-torr regime.

Keywords: photoelectron spectroscopy; XPS; photoemission; synchrotron radiation

Basic Phenomena and Experiments

Photoelectron spectroscopy, often referred to simply as photoemission, has its fundamental origin in the photoelectric effect, which was first explained by Einstein in 1905,[1] led to a Nobel Prize for him in 1921, and was key to the later development of the concept of the photon as the quantum of electromagnetic energy. In the period since the late 1950s, the photoelectric effect has been developed into one of the most powerful tools for studying the composition and electronic structure of matter. Siegbahn received the Nobel Prize for the further development of several aspects of photoelectron spectroscopy in 1981.[2,3]

As currently used, the fundamental energy conservation equation is the following:[4,5]

$$h\nu = E_{binding}^{Vacuum} + E'_{kinetic} = E_{binding}^{Fermi} + \varphi_{spectrometer} + E_{kinetic} \quad (1)$$

in which h is Planck's constant; ν is the photon frequency; $E_{binding}^{Vacuum}$ is the binding energy of a given electron relative to the vacuum level of the sample; $E'_{kinetic}$ is the kinetic energy of the emitted electron just as it leaves the sample; $E_{kinetic}$ is the kinetic energy as measured finally in the spectrometer, and may be different from $E'_{kinetic}$ by a small contact potential difference if the sample is a solid; $E_{binding}^{Fermi}$ is the binding energy relative to the Fermi level or electron chemical potential; and $\varphi_{spectrometer}$ is the work function of the spectrometer used to measure kinetic energy. In very precise measurements, and/or as the excitation energy is increased into the multi-keV regime, both kinetic energies may be reduced by a recoil energy E_{recoil} given to the sample due to momentum conservation; this we discuss below in connection with hard X-ray photoemission. If one measures the electron kinetic energy, and perhaps also knows the spectrometer work function, it is thus possible to measure the binding energies of various inner (or core) electrons, as well as those of the outer (or valence) electrons that are involved in chemical bonding. Such measurements reveal a broad array of phenomena that can be used to characterize a given material, in particular the near-surface regions of solids from which most photoelectrons are emitted. Photoemission is also very fruitfully applied to gas-phase atoms, molecules, and clusters, but we will here focus on work on solid samples.

It is also useful to specify the binding energy more precisely from the point of view of theoretical calculations, and we can write this as:

$$E_{binding}^{Vacuum}(Qn\ell j, K) = E_{final}(N-1, Qn\ell j\ hole, K) - E_{initial}(N) \quad (2)$$

where we for simplicity consider a binding energy for the $n\ell j$ core level from atom Q, with n the principal quantum no., ℓ the orbital angular momentum quantum no., and $j = \ell \pm 1$ the additional quantum no. if spin–orbit splitting is present, $E_{initial}(N)$ is the total initial state energy for the assumed N-electron system, and $E_{final}(N-1, Qn\ell j\ hole, K)$ is the Kth final-state energy for the $(N-1)$-electron system with a hole in the $Qn\ell j$ orbital. As an example, the six electrons in the Mn 2p subshell are split into Mn $2p_{1/2}$ (two electrons with $m_j = -1/2, +1/2$) and Mn $2p_{3/2}$ (four electrons with $m_j = -3/2, -1/2, +1/2, +3/2$). In general, there may be more than one final state associated with a given $Qn\ell j$ hole, with labels $K = 1, 2, \ldots$, as we discuss further below, e.g. in connection with multiplet splitting. Note also that, in the final state with the hole, all of the remaining electrons may relax slightly so as to try to screen the hole, thus lowering the total final energy by some amount that is often called the relaxation energy.[4,5] This relaxation/screening phenomenon has many consequences for the detailed interpretation of spectra. In many-electron theory, these effects are included in what is termed the 'self-energy' correction.

As a final important quantity, we can write the intensity for excitation from a given core level to the Kth final hole-state

* *Correspondence to: Charles S. Fadley, Department of Physics, University of California Davis, Davis, CA 95616, USA. E-mail: fadley@physics.ucdavis.edu*

a *Department of Physics, University of California Davis, Davis, CA 95616, USA*

b *Materials Sciences Division, Lawrence Berkeley National Laboratory, Berkeley, CA 94720, USA*

associated with this level K in the low-energy dipole limit as:

$$I(K) \propto \left|\hat{\varepsilon} \bullet \left\langle \psi_{final}(N-1, Qn\ell\, j\, hole, K + photoelectron) \right.\right. \times \left|\left. \sum_{i=1}^{N} \vec{r}_i \right| \psi_{initial}(N) \right\rangle \Big|^2 \propto |\langle \psi_{final}(N-1, Qn\ell\, j\, \text{hole}, K)|\psi_{Initial} \times (N-1, Qn\ell\, j\, \text{hole})\rangle|^2 \left|\hat{\varepsilon} \bullet \langle \varphi_{photoe}|\vec{r}|\varphi_{Qn\ell\, j}\rangle\right|^2 \quad (3)$$

in which $\hat{\varepsilon}$ is the polarization of the radiation, the notation for initial and final state wave functions is obvious, $\vec{r}$ is one of three forms of the dipole operator that can be used interchangeably,[4] the first line is an N-electron matrix element which emphasizes the inherent many-electron character of photoemission, and the second line involves a common simplifying step via the Sudden Approximation.[4,5] In this Approximation, the intensity is thus a product of the square of a one-electron matrix element which takes an electron from $\varphi_{Qn\ell j}$ to the photoelectron final state φ_{photoe} and the square of a simple $(N-1)$-electron overlap term with no operator between the initial state wave function with a hole in the $Qn\ell j$ subshell but no relaxation/screening and one of the actual final ionic states K which includes such relaxation/screening. The approximation is often made of considering only the last one-electron factor in Eqn (3), but it should be kept in mind that various many-electron effects, or vibrational/phonon effects, or even rotational effects in molecules, can distribute intensity over several states K that go beyond the one-electron picture, as we discuss below.

Having thus considered a formal description of photoemission, we now illustrate in Fig. 1 the various types of experiment possible. A photon of a given polarization, which may be linear, circular, elliptical or unpolarized in character, is incident on the sample surface at some angle θ_{inc}. Photons may be created from either laboratory sources (lasers, UV lamps, X-ray tubes), or synchrotron radiation. The photon is absorbed, exciting a photoelectron into the vacuum with some momentum $\vec{p} = \hbar\vec{K}$, where $\hbar = h/2\pi$, $\vec{K}$ is the electron wave vector, and $\vec{s}$ is the electron spin, and finally into some kind of spectrometer for measuring kinetic energy. We here show the most commonly used spectrometer configuration, which consists of a set of concentric hemispherical deflection electrodes, although several other geometries are possible, including time-of-flight measurements if the exciting source is pulsed. In this hemispherical geometry, electrons of a given energy are focussed to a given radius (i.e. along a given y coordinate in the detection plane of Fig. 1), such that integrating intensity over a given radius yields the first type of measurement: a photoelectron spectrum of number of electrons *versus* kinetic energy or energy distribution curve (EDC), as shown schematically in Fig. 1(a). An actual broad-scan or survey spectrum from a complex oxide sample of $La_{0.6}Sr_{0.4}MnO_3$ is shown in Fig. 2, with various peaks labeled. Note here the presence also of *Auger electron* spectra, which are the result of non-radiative core-hole decay, and whose energies are somewhat more complicated to estimate, but in general involve three binding energies as follows:

$$E^{Auger}_{kinetic}(Z, 123) \approx E_{binding,Z,1} - [E_{binding,Z,2} + E_{binding,Z+1,2}]/2 - [E_{binding,Z,3} + E_{binding,Z+1,3}]/2 \quad (4)$$

where the Auger kinetic energy results from an initial core hole in atomic level 1 of an atom with atomic number Z, which is filled by an electron from level 2 dropping into level 1, thus exciting an electron from level 3, or by an electron from level 3 dropping into level 1, thus exciting an electron from level 2, with these two processes being indistinguishable. Note that the most accurate prediction of these energies involves binding energies for both atom Z and the next higher in atomic number at $Z+1$, via what is often called the Equivalent Core Approximation.[4,5]

If the photoelectron emission direction is varied relative to the crystal axes of a single-crystal sample, by scanning the angles θ and ϕ in Fig. 1, additional effects are seen, due to the scattering

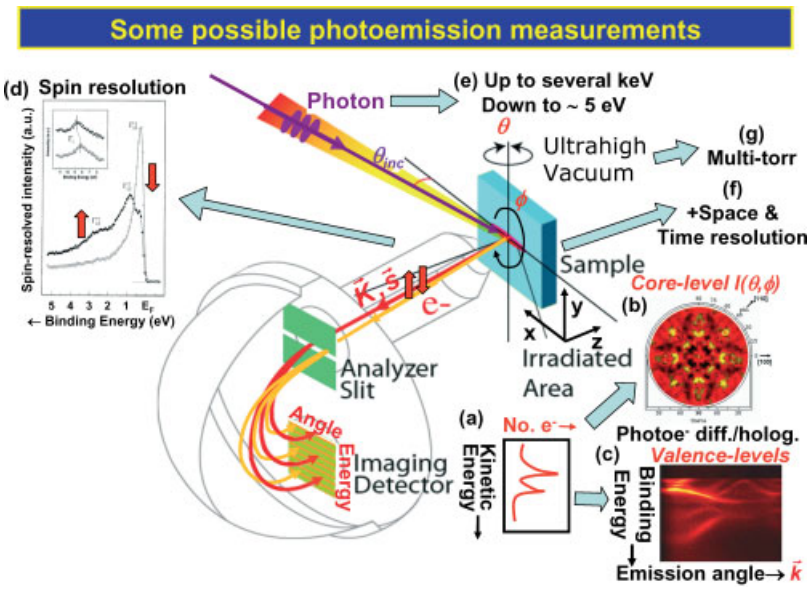

Figure 1. Illustration of a typical experimental configuration for photoemission experiments, together with the various types of measurements possible, including (a) simple spectra or energy-distribution curves, (b) core-level photoelectron diffraction, (c) valence-band mapping or energy *versus* $\vec{k}$ plots, (d) spin-resolved spectra, (e) measurements with much higher or much lower photon energies than have been typical in the past, (f) measurements with space and time resolution, and (g) measurements at high ambient sample pressures of several torr. (With acknowledgement to Y. Takata for part of this figure).

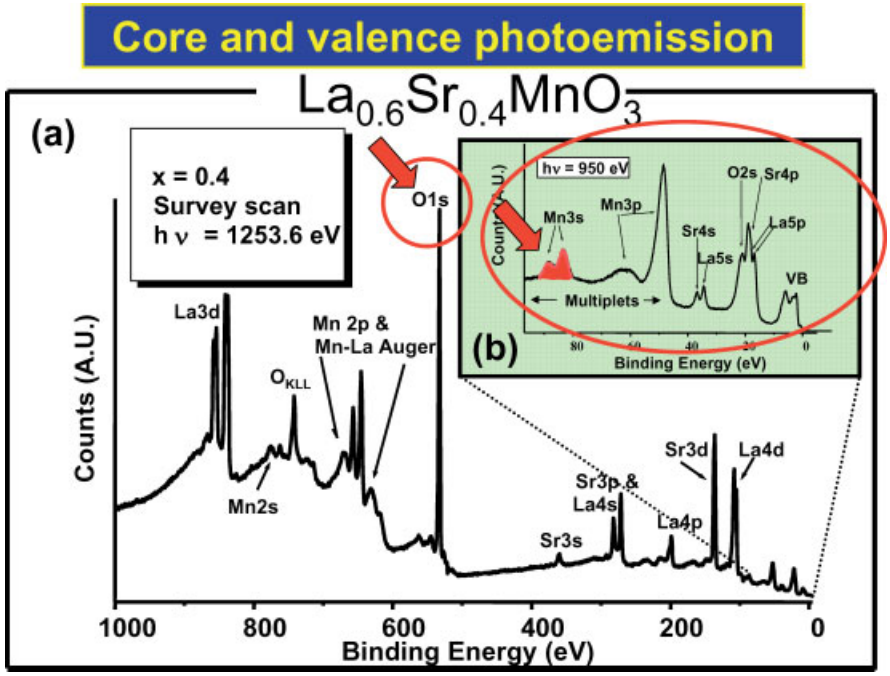

Figure 2. (a) A broad survey spectrum from the colossal magnetoresistive oxide $La_{0.6}Sr_{0.4}MnO_3$ obtained with excitation at 1253.6 eV, together with (b) an inset obtained at 950 eV over the region of the highest lying core levels and the valence levels. The highlighted O 1s and Mn 3s spectra have been studied as a function of temperature (Fig. 5).

of the outgoing electron wave from various atoms in the sample. If the emission is from a core level that is necessarily highly localized on one atomic site, a photoelectron diffraction (PD) pattern is observed.[6] An example of this for O 1s emission from NiO(001) is shown in Fig. 1(b). Such patterns can be used to determine near-surface atomic structures. If the emission is from a valence level that is delocalized over many sites due to chemical bonding and electronic band formation, additional anisotropy in emission is found, and this can be measured, for example, by taking advantage of another property of the hemispherical electrostatic analyzer with a two-dimensional (2D) imaging detector. In this case, a 2D image can be directly related to the binding energy versus electron momentum or electron wave vector inside the crystal $\vec{k}$, which is then in many cases directly relatable to the band structure, or more precisely the quasi-particle excitation spectrum of the material. An example of this for emission from W(110) is shown in Fig. 1(c).

Some other aspects of the measurement possibilities that exist are also shown in Fig. 1. If an additional sensitivity to electron spin is somehow built into the detector (e.g. by taking advantage of spin–orbit scattering of high-energy electrons from a heavy-atom target in Mott scattering), it is possible to measure also the electron spin, providing additional information of particular relevance to magnetic materials. Another inset in Fig. 1(d) shows such a measurement for the valence bands of iron, clearly indicating the difference in the electronic state distributions of spin-up and spin-down electrons for this ferromagnet.[7]

Beyond this, as indicated in Fig. 1(e), one can vary the photon energy, by going significantly above and significantly below the energy regime from ~20 to 1500 eV that has been used in most prior photoemission measurements. Also, Fig. 1(f) indicates that we can expand upon the spectrometer in order to turn it into a microscope, thus yielding spectral images as a function of lateral position on the sample: the *x* and *y* coordinates in Fig. 1. This type of measurement is reviewed in detail elsewhere,[8,9] so we will not consider it beyond one later example here. There are also newer types of measurements involving time resolution (again Fig. 1(f)), in which some perturbation of the sample is made, e.g. by gas reaction with a surface or by short-pulse light excitation, and the spectra are measured as a function of time. Depending on the particular process involved, these measurements can be fruitfully carried out on timescales varying from minutes (for chemical reactions) to seconds to femtoseconds (for laser pump-and-probe experiments).[9–12] Finally, Fig. 1(g) indicates that it is possible with special differential pumping outside the sample region to carry out photoemission studies at up to several torr of pressure.[13]

Of key importance in any such photoemission experiment, however, is the depth of sensitivity in a solid sample, which is controlled primarily by the inelastic mean free path Λ_e, for the photoelectrons, perhaps as modified by elastic electron scattering to yield an effective attenuation length.[14,15] If inelastic scattering is assumed to be isotropic in the material, the intensity from a certain emission depth *z* will decay as $I(z) = I_0 exp[-z/\Lambda_e sin\theta]$, and the mean escape depth below a surface will be given simply by $\Lambda_e sin\theta$, as shown in Fig. 3(a).

Typical curves of Λ_e *versus* electron kinetic energy are shown for graphite and germanium in Fig. 3(b) and (c), with calculations being made via the much-used and reasonably accurate TPP-2M formula due to *T*anuma, *P*owell, and *P*enn.[15] One expects for any material a minimum of Λ_e for energies in the range of 20–50 eV that is only about 5–10 Å in magnitude, and a generally increasing trend away from this, in particular going approximately as $E_{kinetic}^{0.75}$ as energy goes into the multi-keV range. The general shape of this curve is thus in a sense 'universal', applying at least qualitatively to all elements and compounds, but in reality it is 'non-universal' in that the actual values can be quite different from one substance to another, as is clear from Fig. 3(b) and (c). The detailed behavior at very low energies is also expected to

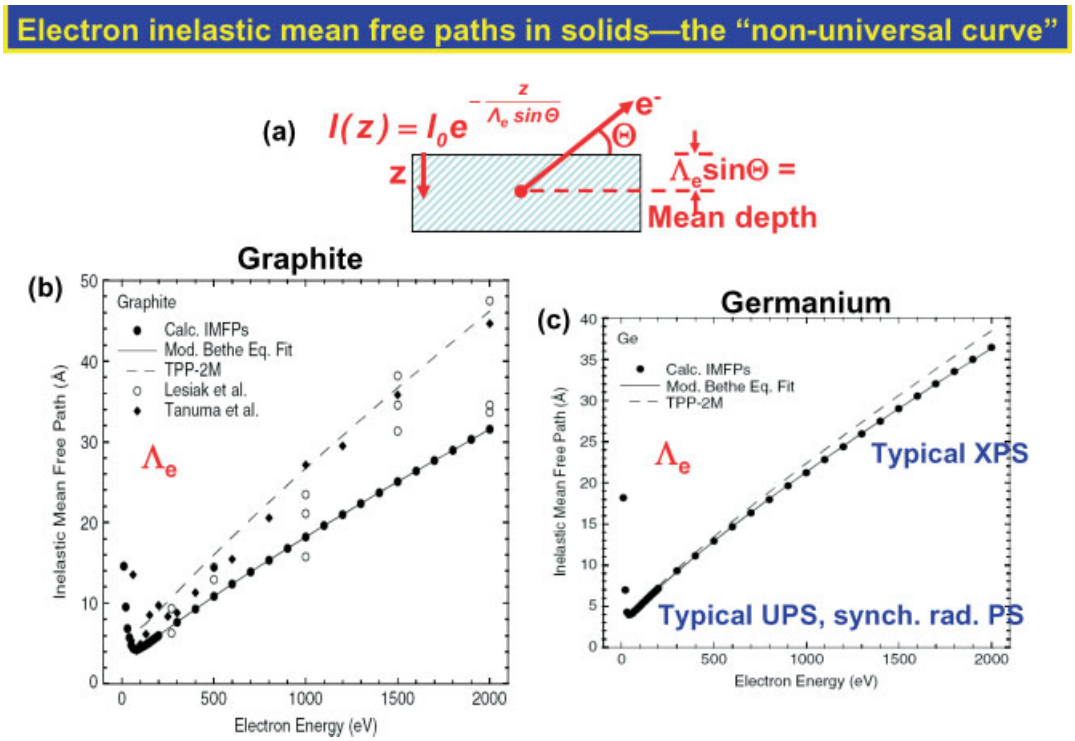

Figure 3. (a) A schematic diagram indicating the mean depth of photoelectron escape if elastic scattering and inner potential effects are neglected, together with electron inelastic attenuation lengths for two representative elemental solids, (b) graphite and (c) germanium. (b) and (c) from S. Tanuma *et al*., *Surf. Interface Anal.* **2005**, *37*, 1. Reprinted with permission.

be different for different materials, a topic of current discussion in connection with photoemission experiments with excitation energies of only 5–10 eV that are aimed at being more bulk sensitive. Historically, photon sources were first divided into two regimes, UV lamps in the *ca* 20–40 eV range, leading to the term ultraviolet photoelectron spectroscopy (UPS), and X-ray tubes in the *ca* 1–2 keV range, leading to the term X-ray photoelectron spectroscopy (XPS). Figure 3 thus makes it clear that one expects very different degrees of surface sensitivity in these two regimes, with typical Λ_e values of $\sim$5 – 10 Å for UPS and $\sim$20–30 Å for XPS. Synchrotron radiation now permits spanning this full range continuously, and in the last few years, has also permitted using photon energies up to 10–15 keV, which yield via the extrapolation above to Λ_e values of 50–200 Å; such measurements are thus appealing for the future as being more bulk sensitive, and represent another emerging area in photoemission to which we will return later.[16,17]

Core-Level Photoemission

Intensities and the Three-Step Model

Because core levels are highly localized on a given atom, they provide various element-specific types of information concerning each atomic species present in a sample. We consider first the intensities of a given photoelectron peak, which will be proportional to the number of atoms of a given type, as weighted by their excitation probabilities. Figure 2 makes it clear that each atom may have several core-level signatures of its presence, including both photoelectron and Auger peaks.

A much-used approach for calculating and using photoelectron intensities from both core and valence levels is the so-called three-step model[4,5] which divides the process into three steps of: (1) penetration of the exciting photon beam into the surface, with some resulting intensity profile $I_{h\nu}(x, y, z)$, and the coordinates defined in Fig. 1, and excitation of photoelectrons from each atom in the sample that are located at various depths z, which will be proportional to the differential photoelectric cross section of the particular level $n\ell j$ of atom Q involved (e.g. Mn $2p_{1/2}$ and Mn $2p_{3/2}$ in Fig. 2), written as $d\sigma_{Qnlj}(h\nu)/d\Omega$ and dependent on photon energy and the experimental geometry; (2) transport of the photoelectron from depth z to the surface, which involves inelastic attenuation via Λ_e, as well as elastic scattering and diffraction and (3) escape from the surface, which involves refraction and reflection at the surface barrier, with the latter controlled by the surface inner potential V_0 having typical values of 5–15 eV, and possible inelastic scattering, as well as elastic scattering and diffraction (surface umklapp processes). The differential subshell cross section can most simply be calculated by using only the last one-electron factor in Eqn (3), averaging over the possible final states reached from each $Qn\ell j$, and summing over the $Qn\ell j$ initial states (e.g. two for Mn $2p_{1/2}$ and four for Mn $2p_{3/2}$). In general, $d\sigma_{Qnlj}(h\nu)/d\Omega$ is a maximum near threshold, when the photon energy is equal to $E^{Vacuum}_{binding}(Qnlj)$, and steadily decreases as the energy increases, although it may not reach a maximum until some distance above threshold, and it may also exhibit local minima called *Cooper minima* for energies not too far above threshold.[4,18] Neglecting elastic scattering and surface refraction for simplicity, one can finally calculate a core-level intensity from:

$$I(Qnlj) = C \int\int\int I_{h\nu}(x,y,z)\rho_Q(x,y,z)\frac{d\sigma_{Qnlj}(h\nu)}{d\Omega} \times exp\left[-\frac{z}{\Lambda_e \sin\theta}\right]\Omega(h\nu,x,y)dxdydz \quad (5)$$

where C is a constant characteristic of the experimental geometry, $\rho_Q(x,y,z)$ is the density of atomic type Q at position x,y,z, and $\Omega(h\nu, x, y)$ is the solid angle of acceptance of the spectrometer for a given photon energy (or equivalently electron kinetic energy) and position on the sample surface. In principle, $I_{h\nu}(x,y,z)$ can be calculated from a knowledge of the source beam spot profile, the incidence angle, and the X-ray indices of refraction of the substances in the sample;[19] $d\sigma_{Qnlj}(h\nu)/d\Omega$ is known from atomic theory, and its evaluation requires knowing the polarization of the exciting radiation (*cf* Eqn (3)),[18,20–22] Λ_e can either be taken from experimental data[23] or estimated from semi-empirical formulas, as e.g. the much-used TPP-2M formula[15]; and $\Omega(h\nu, x, y)$, which is equivalent once integrated over x and y to the spectrometer intensity response function, can be detemined from reference-sample calibration measurements.[24] Thus, it is in principle possible to measure $I(Qnlj)$ and determine the only remaining unknown $\rho_Q(z)$, which amounts to a quantitative chemical analysis of the sample. More detailed discussions of cross-sections and their angular dependence, as well as integrations of Eqn (5) to yield closed-form formulas for various sample configurations (homogeneous semi-infinite sample, single overlayer on a semi-infinite sample, thin overlayer on a semi-infinite sample) are given elsewhere.[4] These form the basic core of quantitative surface analysis by XPS, but with recent reviews pointing out additional considerations in achieving the most accurate results, as e.g. elastic scattering and electron refraction in crossing the inner potential surface barrier V_0.[6,14,15,25–27] User-friendly computer programs in fact exist that include some of these complicating factors, and permit predicting spectra with reasonable accuracy.[28]

A final important effect related to photoelectron intensities is *resonant photoemission* (RPE), in which the photon energy is tuned so as to lie on a strong core-level absorption resonance (e.g. Mn $2p_{3/2}$ or L_3), with this providing a second interfering channel for photoelectron excitation in another level in the same atom (e.g. Mn 3d).[29] The intensity of the second level can thus be dramatically increased or decreased, depending on the relative amplitudes and phases of the interfering channels. This effect can be very useful in enhancing the contributions of a given type of valence character to bonding (e.g. by enhancing the Mn 3d contributions to the valence spectra of a compound such as that shown in Fig. 2[29]). It has also been pointed out that RPE can occur between levels on different atoms, as e.g. between $O1s$ and Mn 3d in the compound MnO,[30] with this type of *multi-atom resonant photoemission* (MARPE) effect providing the potential of uniquely identifying near-neighbors to a given atomic species.

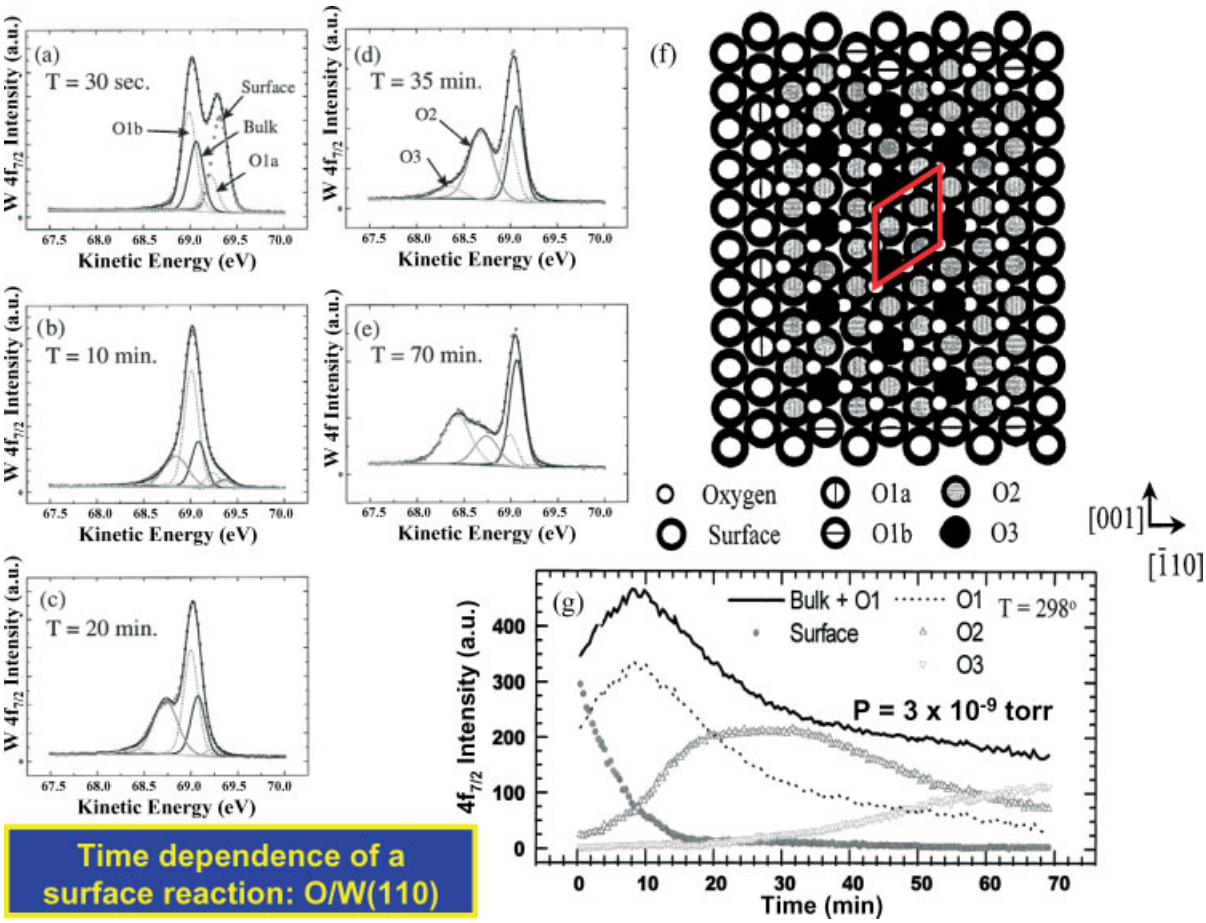

Figure 4. (a)–(e) High-resolution W $4f_{7/2}$ spectra excited with 100 eV radiation from a W(110) surface that was initially atomically clean but was exposed over a period of time to oxygen gas at a pressure of 3×10^{-9} torr. Six distinct chemical or structural states of W can be identified by the observed binding energy shifts: clean-surface W atoms, two types of W bonded to one oxygen atom, one type of W bonded to two oxygen atoms, one type of W bonded to three O atoms, and 'bulk' W atoms located inward from the surface layer. (f) Geometric identification of the different atomic sites involved. The red figure is the unit cell of an ordered (2×2) oxygen structure. (g) Time dependence of the intensities of the resolvable features in a set of these spectra. From R. X. Ynzunza *et al.*, *Surf. Sci.* **2000**, *459*, 69. Reprinted with permission.

Varying Surface and Bulk Sensitivity

From Fig. 3, it is clear that the degree of surface sensitivity can be enhanced/deenhanced systematically in two ways: by going to more grazing/more nearly normal emission angles θ, respectively, often referred to as angle-resolved XPS (ARXPS); or by altering photon energies so as to scan the photoelectron kinetic energy relative to the minimum in Λ_e. Both of these methods are being used successfully to deconvolute the surface and bulk contributions that will always be present in photoemission spectra.[26] We will also later consider a third method, which makes use of X-ray standing waves to selectively probe at specific depths below a surface.[31]

Chemical Shifts

Although core levels are still often thought of as not being affected at all by chemical bonding, and in fact, their orbitals do not mix in a quantum-mechanical sense into the valence bands or molecular orbitals responsible for bonding, core-level binding energies are extremely sensitive to the changes in valence-level charge distributions that take place as bonds form, as first pointed out by Siegbahn *et al*.[2] Roughly speaking, if an atom is placed in an environment in which it effectively loses charge to more electronegative neighbors, its core electrons will experience an increase in the net coulombic attraction (which is always due to the sum of nuclear attraction and other-electron repulsion), and their binding energies will go up. Conversely, if an atom becomes more negatively charged in forming bonds to its neighbors, its core electrons will have lower binding energies. For an *isolated* atom and considering a core level that spatially overlaps very little with the valence level involved (that is, of different principal quantum no. n), the removal/addition of a valence electron will to first approximation result in a binding energy shift given by the following Coulomb integral:[32]

$$\Delta E_{Binding} \approx \pm K_{Core,Val} = \pm \int \varphi^*_{Core}(\vec{r}_1)\varphi^*_{Val}(\vec{r}_2) \times \frac{e^2}{|\vec{r}_1 - \vec{r}_2|}\varphi_{Core}(\vec{r}_1)\varphi_{Val}(\vec{r}_2)dV_1 dV_2 \quad (6)$$

However, this is an overestimate in any real situation, as the bonding charge is not removed or added from infinity, but simply relocated to/from near-neighbor atoms.[32] Final-state effects in which the other electrons relax around a given core hole to screen it can complicate this picture, and the most accurate way to determine core binding energies in different environments and to analyze such 'chemical shift' data is to calculate total all-electron energies with and without a given core hole present, as shown in Eqn (2). But whatever the method of interpretation, the use of core-electron chemical shifts represents a very powerful way of detecting different chemical species in a complex system, with many examples of this in the literature, and several detailed tabulations of chemical shifts for many elements.[33]

As an illustrative example of chemical shifts, we show in Fig. 4(a)–(e) spectra from the very narrow W $4f_{7/2}$ level of a W(110) surface that is initially very clean but has been exposed to molecular oxygen at 3×10^{-9} torr over a sequence of time-resolved measurements.[10] The high resolution of this low-energy synchrotron radiation experiment, combined with careful peak fitting of many spectra through the time sequence, permits resolving six different chemical/structural states of W: those at the clean surface, those in the 'bulk' = layers below the surface,

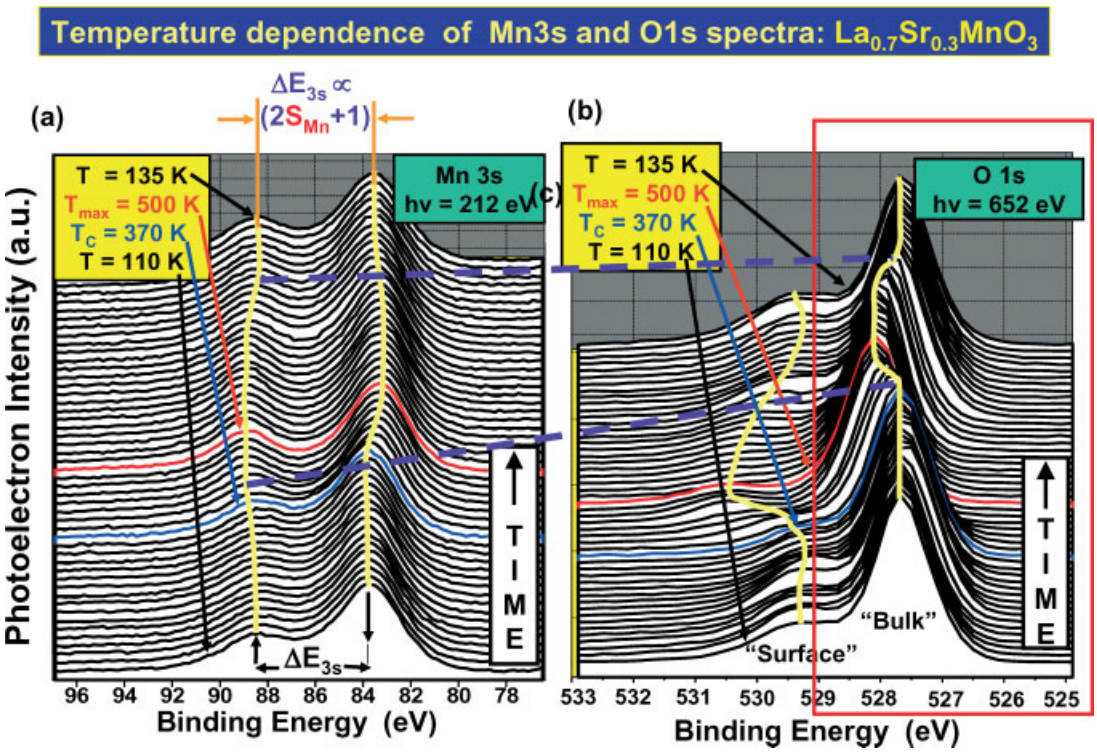

Figure 5. Temperature-dependence of the Mn 3s and O 1s spectra from a freshly fractured surface of $La_{0.7}Sr_{0.3}MnO_3$ (*cf* Fig. 2). The two photon energies indicated have been chosen so that the photoelectrons in both cases have very nearly the same kinetic energy and thus the same inelastic attenuation lengths and surface sensitivity. From N. Mannella *et al*., *Phys. Rev. Lett*. **2004**, *92*, 166401. Reprinted with permission.

two structurally inequivalent types bonded to one adsorbed oxygen atom (O1a and O1b), and those bonded to two or three oxygen atoms (O2 or O3, respectively), with the different atomic geometries for five of these shown in Fig. 4(f). These data thus illustrate the high sensitivity of core levels to chemical state and bonding position relative to the surface. We discuss the time dependence in these spectra in the last section of this paper.

As a second example of the use of such chemical shifts, in Fig. 5(b), we show the temperature dependence of O 1s spectra from a complex metal oxide with formula $La_{0.7}Sr_{0.3}MnO_3$ which exhibits an effect called colossal magnetoresistance.[34] The oxide surface was here prepared by cleaving, or more precisely, fracturing, a single crystal in UHV, in order to avoid surface contamination. Firstly, these O1s spectra exhibit a main peak and a weaker peak at about 1.5 eV higher binding energy. From various measurements, including varying the electron takeoff angle to change the degree of surface sensitivity (*cf* Fig. 3(a)), it is concluded that the peak at higher binding energy is due to O atoms near/at the surface, with the other peak representing O atoms deeper within the material and denoted 'Bulk' in the figure. Now considering the changes in these spectra as temperature is varied from well below to well above the temperature at which long-range magnetic order disappears (the Curie temperature, T_C) and then cooled to near the starting temperature again, we see a distinct shift in the bulk O 1s peak as T goes above T_C, and a concomitant shift, broadening and loss of intensity in the O 1s surface peak. Upon cooling again to below T_C, both features return to their previous states. The bulk peak shift has been interpreted as a transfer of electron charge to Mn from the six octahedral O atoms surrounding each Mn atom.[34] We return to discuss the left panel (a) of this figure involving Mn 3s emission in the next section.

Multiplet Splittings

Another very useful aspect of core photoelectron spectra arises if a given atom exists in a situation in which the valence levels are only partially occupied. In such a case, and with neglect of relativistic effects for simplicity of discussion here, the valence electrons can couple with one another such that there is a net spin S and a net orbital angular momentum L on a given site. In the simplest Russell–Saunders or L–S coupling picture, this yields a state before an electron is emitted of the form that can be described e.g. for the ground state of a $3d^5$ configuration with $S = 5/2$ and $L = 0$ as a ^6S state, where the superscript is the spin multiplicity $2S + 1$ and the main symbol denotes the net orbital angular momentum as S, P, D, for $L = 0$, 1, 2, etc. However, when an electron is emitted from a core level with a given one-electron spin s, corresponding to spin projections $m_s = -1/2$ or +1/2, and a given one-electron orbital angular momentum ℓ, the new $(N - 1)$-electron system of core subshell-with-hole plus partially-filled valence electrons can couple to various final states S_f and L_f of different energies, thus yielding more than one binding energy for emission from a single $n\ell$ core level. This is termed a 'multiplet splitting' of core-level binding energies,[4,35] and it can be generalized to include spin–orbit splitting and to apply to partially filled s, p, d, and/or f subshells.

In Fig. 6(a), we illustrate the origin of a simple type of multiplet splitting, for emission from a 3s subshell of an Mn transition metal atom. In this case, there is no orbital angular momentum in the core electron left behind, so we only need consider the coupling of the net spin on the Mn atom before 3s emission, S_{Mn}, which can be assumed to be carried by its valence 3d electrons, with the spin of the 3s electron left behind. The two final state energies then correspond to total spin quantum nos. of $S_f = S_{Mn} + 1/2$ and $S_{Mn} - 1/2$, and these can be considered to arise primarily from a coupling of

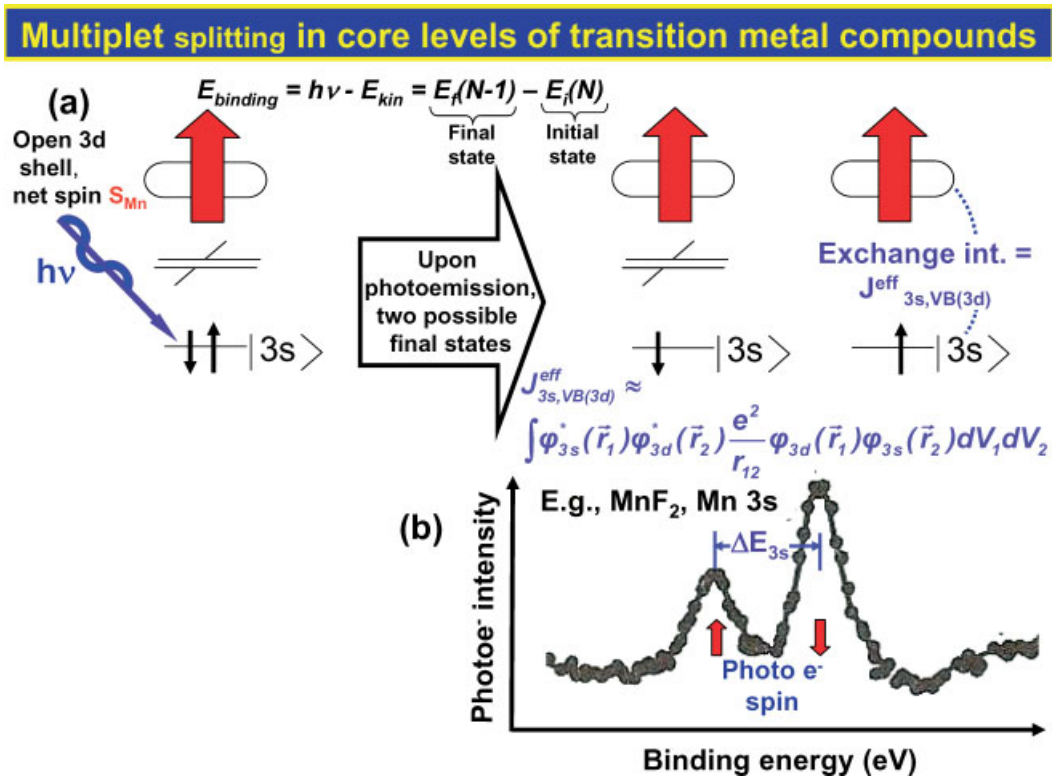

Figure 6. Qualitative explanation of the multiplet splittings seen in 3s emission from some transition metal compounds, here illustrated for an Mn-containing substance. The inset at lower right shows a spectrum from the highly ionic compound MnF_2, excited by 1486.7 eV radiation.

the remaining Mn 3s spin parallel to, or anti-parallel to, the net 3d spin S_{Mn}, respectively. Because the energy-lowering exchange interaction only acts between electrons of parallel spin, and also requires non-zero overlap to be significant, the higher-spin state energy will be lowered through the following effective exchange integral between a 3s orbital φ_{3s} and a valence-band (VB) 3d orbital φ_{3d}:

$$J^{eff}_{3s,VB(3d)} \approx \int \varphi^*_{3s}(\vec{r}_1)\varphi^*_{3d}(\vec{r}_2)\frac{e^2}{|\vec{r}_1 - \vec{r}_2|}\varphi_{3d}(\vec{r}_1)\varphi_{3s}(\vec{r}_2)dV_1 dV_2 \quad (7)$$

where e is the electron charge, and the energy splitting between the two states ΔE_{3s} can finally be estimated from the Van Vleck Theorem of atomic physics as:

$$\Delta E_{3s} \approx (2S_{Mn} + 1)J^{eff}_{3s,VB(3d)} \quad (8)$$

Thus, we see that such splittings can be used to directly derive information on the spin of a magnetic atom, with other details also derivable from more complex multiplets involving $\ell > 0$ and spin–orbit coupling.[36] Fig. 6(b) also shows an experimental spectrum from the compound MnF_2, which is highly ionic and involves an initial state of Mn ... $3s^2$ ... $3d^5$ ^{6}S, and final states of ... $3s^1\uparrow$ ... $3d^5$ ^{7}S and ... $3s^1\downarrow$ ... $3d^5$ ^{5}S, with a large and easily measurable splitting of $\Delta E_{3s} = 5.8$ eV.[35,37]

As a specific example of the use of such multiplets, Fig. 5(a) shows the temperature dependence of the Mn 3s splitting in the colossal magnetoresistive oxide $La_{0.7}Sr_{0.3}MnO_3$, and it exhibits a distinct increase of about 1 eV or 20% over the same temperature range as the O 1s chemical shifts discussed previously. This increase has been interpreted as being caused by an increase in S_{Mn} that is equivalent to a net transfer of one electronic charge from the O atoms to Mn, an effect not observed previously.[34]

Electron Relaxation, Screening, and Satellite Structures

We have noted before that the presence of a core-electron hole, or indeed any electron hole, induces other-electron relaxation, screening or polarization around it. These effects are best described in a full many-electron theory, and they can lead in some cases to additional strong satellite features in spectra which again can provide information on the nature of the valence electronic structure.

One particularly dramatic example of this occurs in the 2p spectra of certain 3d transition metals and their compounds. As an example, we show in Fig. 7 the spin–orbit split Cu $2p_{1/2}$ and $2p_{3/2}$ doublet spectral region for $CuCl_2$.[36] In the simplest ionic picture, one would expect only two peaks here, but there are four, with each member of the doublet showing a very strong satellite at lower kinetic energy or higher binding energy. (Note the reversed energy scale from earlier spectra presented.) The explanation of these satellites lies in the fact that we can consider Cu in this compound to exist as $Cu^{2+}3d^9$, with just one hole in the 3d subshell. In the final state with a 2p hole and no screening, we can have $Cu^{3+}2p^1_{1/2}2p^4_{3/2}3d^9$ or $Cu^{3+}2p^2_{1/2}2p^3_{3/2}3d^9$, where we have italicized the subshell with a hole. Multiplet splitting can occur in these states, as indicated by the vertical bars from a theoretical calculation in the figure. However, screening can also occur in the final state via charge transfer from Cl to Cu, so as to form the closed shell $Cu^{2+}2p^1_{1/2}2p^4_{3/2}3d^{10}$ or $Cu^{2+}2p^2_{1/2}2p^3_{3/2}3d^{10}$ and, since such transfer costs relatively little energy, such screening will lower the binding energy. In this closed-shell system, there is no multiplet splitting and the peaks are narrower. A key point here is that both final states (screened and unscreened) can be reached in photoemission, with their strengths depending upon how they are mixed in a final-state wave function that is in general a configuration–interaction mixture of both. That is, both types of final states are for the specific case of $2p_{3/2}$ emission to a first approximation a mixture of the form:

$$\Psi_{final,K}(N-1) = C_{1,K}\Phi_1(2p^2_{1/2}2p^3_{3/2}3d^9) + C_{2,K}\Phi_2 \times (2p^2_{1/2}2p^3_{3/2}3d^{10} + Cl\ hole) \quad (9)$$

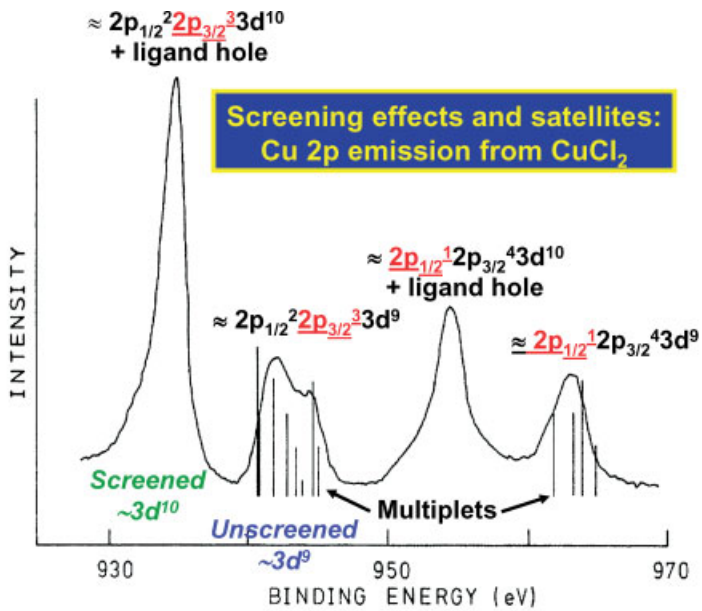

$$\Psi_{final,K}(N-1) = C_{1,K}\Phi_1(2p^2_{1/2}2p^3_{3/2}3d^{10} + C\ell\ hole) + C_{2,K}\Phi_2(2p^2_{1/2}2p^3_{3/2}3d^9)$$

Figure 7. A Cu 2p photoelectron spectrum from $CuCl_2$, excited with 1486.7 eV radiation and with the dominant electron configurations of the ' screened' $3d^{10}$ and the ' unscreened' $3d^9$ satellite peaks indicated. From G. Van der Laan *et al.*, *Phys. Rev. B* **1981**, *23*, 4369. Reprinted with permission.

with $K = 1,2$. This implies, via the Sudden Approximation form of Eqn (3), that, if the initial state is assumed to be pure $3d^9$, the intensity of the two mixed final states will be proportional to $|C_{1,K}|^2$, as the other overlap term will vanish due to the different symmetries of the functions involved. Although the actual wave functions can contain many more terms in principle than we show here, this type of analysis in terms of final-state mixing coefficients is common in both multiplet and satellite theory, and is discussed in more detail elsewhere.[4,36]

More examples of such combinations of satellite structures and multiplet splittings for other compounds and in connection with emission from other core levels, together with theoretical calculations, are shown elsewhere.[35–39]

As another more complex example involving a metallic system, we show the 2p spectral region of ferromagnetic Ni in Fig. 8(a), excited at 1100 eV photon energy and averaged over two different polarizations of the radiation (right circular = RCP and left circular = LCP).[40] Since Ni, like Cu^{+2}, has roughly a configuration of $3d^9$ in its ground state, one sees for both polarizations a screened predominantly $3d^{10}$ peak and a predominantly $3d^9$ unscreened satellite in connection with each member of the doublet.[40,41] The more complex nature of the electronic structure of Ni even leads to some mixing of $3d^8$ into the higher binding energy regions of each member, as discussed elsewhere.[41] Experiment is compared in this figure with (b) one-electron theory[40] and (c) a more accurate many-electron theory,[41] and it is obvious that the many-electron approach much better predicts the satellite structure.

Magnetic Circular Dichroism

In magnetic circular dichroism (MCD), the intensity of a photoelectron peak is somehow found to change when the polarization of the incoming radiation is changed from right circular (RCP) to left circular (LCP). MCD is thus defined as the difference of two intensities or I(RCP) − I(LCP), usually divided by the sum or the average of these two intensities to yield a fractional number. These effects were first observed and qualitatively interpreted in core-level photoemission from Fe,[42] and these first experimental results are shown in Fig. 9(a) and (b). A simple one-electron explanation of these results is illustrated in Fig. 9(c).[42,43] The spin–orbit interaction, represented here by a parameter λ, splits the six 2p states into two $2p_{1/2}$ and four $2p_{3/2}$ states. Beyond this, one assumes a Zeeman-like splitting of the sublevels within each spin–orbit peak induced by an effective internal magnetic field of the ferromagnet and resulting from the exchange interaction; this is associated with a parameter ξ. These interaction parameters can be used in a one-electron Hamitonian, whose diagonalization yields the result that, in the main $2p_{3/2}$ peak, the sublevels $m_j = -3/2, -1/2, +1/2$, and $+3/2$ are no longer degenerate, as shown in the figure. The same is true of the two $2p_{1/2}$ sublevels. These energy splittings are then combined with the different intensities expected for these levels through the appropriate atomic transition probabilities, which scale as a third parameter Δ, and are represented by the heights of the vertical bars in the figure. The interchange of these intensities when the polarization is switched from RCP to LCP (or equivalently, the magnetization $\vec{M}$ is switched in direction as shown in the figure), then yields the expectation of an up-down character for the MCD

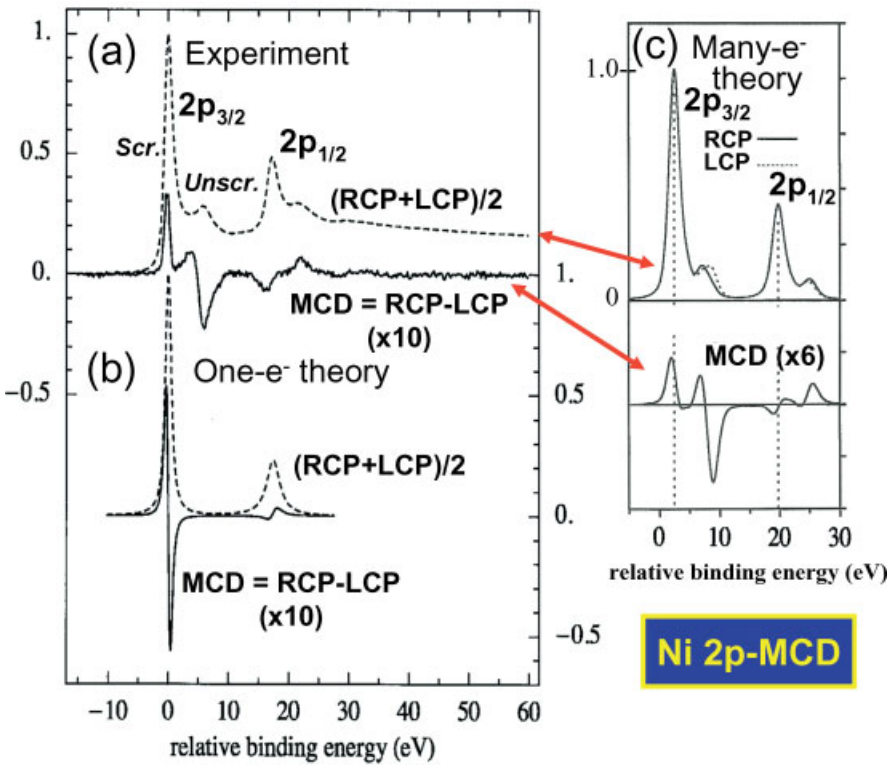

Figure 8. (a) Experimental intensity and magnetic circular dichroism (MCD) results for Ni 2p emission from an epitaxial Ni overlayer with photons of 1100 eV energy, are compared to the results of (b) one-electron theory based on a spin-polarized relativistic KKR method. From G. Van der Laan *et al*., *J. Phys.: Condens. Matter* **2000**, *12*, L275. Reprinted with permission. (c) Intensity and MCD results from a many-electron theory. From. J. Menchero, *Phys. Rev. Lett.* **1996**, *76*, 3208. Reprinted with permission.

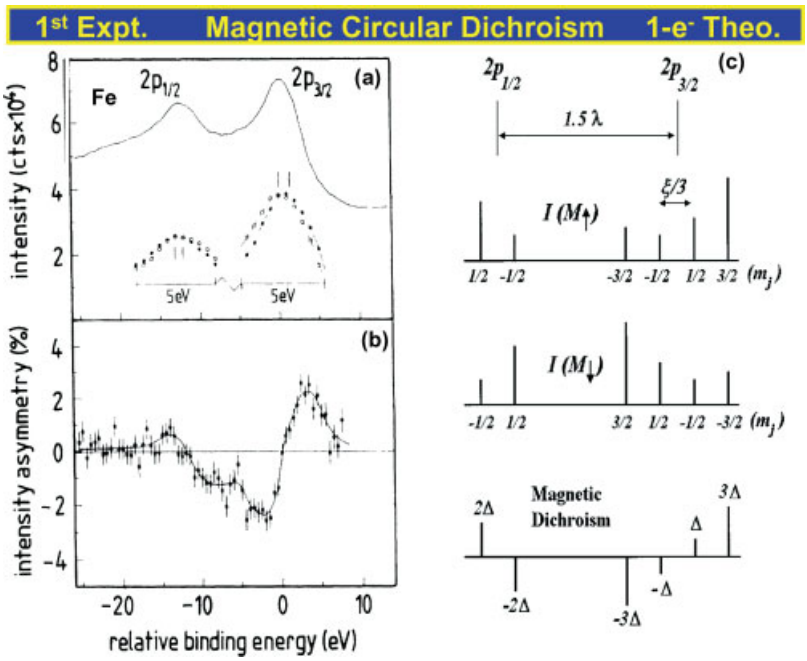

Figure 9. (a) The first magnetic circular dichroism data in core-level photoemission, for Fe 2p emission excited at 800 eV from Fe(110). The total intensity summed over RCP and LCP polarization is shown at the top, above the individual RCP and LCP spectra. (b) The resultant MCD spectrum, here obtained as $[I_{RCP} - I_{LCP}]/[I_{RCP} + I_{LCP}]$. (c) An explanation of the MCD in terms of one-electron theory. Here, the parameter λ represents the spin–orbit interaction, the parameter ξ a Zeeman-like exchange splitting of the different m_j sublevels, and the parameter Δ intensity. (a) and (b) from L. Baumgarten *et al*., *Phys. Rev. Lett.* **1990**, 65, 492; (c) from J. G. Menchero, *Phys. Rev. B* **1998**, *57*, 993. Reprinted with permission.

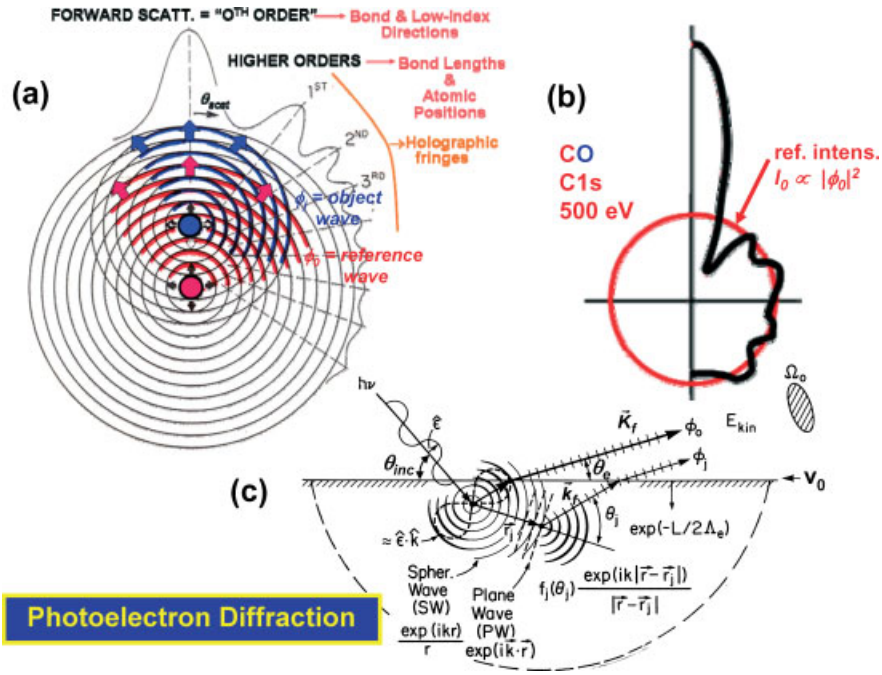

Figure 10. Illustration of various aspects of photoelectron diffraction. (a) Simple diffraction features expected in emission from one atom in a diatomic system. (b) An accurately calculated diffraction pattern for C 1s emission from an isolated CO molecule at a kinetic energy of 500 eV. Note the strong forward scattering peak, and other interference peaks or fringes extending from near the forward scattering direction to the backward scattering direction. (c) The basic theoretical ingredients required to describe photoelectron diffraction. The calculations in (b) were performed using the EDAC program of Ref. [45].

profile across a given peak, as well as an opposite sign of the MCD for the $2p_{3/2}$ and $2p_{/2}$ peaks. This general form of MCD spectra has by now been observed in many 3d transition metal systems.

As a more recent example, we show in Fig. 8 experimental MCD data for 2p emission from Ni,[40] again together with one-electron[40] and many-electron[41] theoretical calculations. Although the MCD curves here are complex, they can be

qualitatively understood in terms of the same model. However, the situation in Ni is more complex due to the presence of the screening satellites discussed previously and the intermixing of various configurations in both the initial and final states. This complexity leads to additional structure in the MCD curves, which is not present in the one-electron theory,[40] but is very well described by many-electron theory.[41]

Because ferromagnetic order is necessary for MCD to be observed, measurements of this provide an element-specific measurement of magnetic order, and this technique has been used to study a variety of magnetic systems, including also rare earths.[38]

Photoelectron Diffraction and Holography

In PD, sometimes referred to as X-ray photoelectron diffraction (XPD) due to the higher excitation energies that are often used, a core-level photoelectron scatters from the atoms neighboring the emission site, so as to produce angular anisotropy in the outgoing intensity.[6] Fig. 10(a) shows the qualitative effects expected for the simple case of emission from the bottom red atom and elastic scattering from the top blue atom in a diatomic molecule, and Fig. 10(b) shows a quantitative calculation for emission from the C 1s subshell in an isolated CO molecule at 500 eV kinetic energy. Electron-atom elastic scattering is typically peaked in the forward direction, with this effect becoming stronger (that is, having a stronger and narrower forward peak) as energy increases.[6] For the CO case in Fig. 10(b), the intensity in the forward direction is in fact enhanced relative to that expected without scattering (I_0 in the figure) by about three times. Thus, one expects in XPD curves both a forward scattering peak (sometimes referred to as forward focussing) along near-neighbor interatomic directions, as well as higher-order diffraction interference effects that one can also consider to be holographic fringes. Back scattering is weaker as energy increases, but Fig. 10(b) shows that, even at 500 eV, there are still interference fringes in the backward direction, and such backscattering effects have in fact been used for adsorbate structure determination.[44]

Such XPD effects can be modeled using the ingredients shown in Fig. 10(c). The polarization $\hat{\varepsilon}$ of the light influences the directionality of the initial photoelectron wave (*cf* Eqn (3)), and, for emission from an s-subshell, the outgoing unscattered wave φ_0 has an amplitude proportional to $\hat{\varepsilon} \cdot \hat{k}$, where $\hat{k}$ is a unit vector in the direction of the photoelectron wave vector, and the photoelectron deBroglie wavelength will be given by $\lambda_e = h/|\vec{p}| = 2\pi/|\vec{k}|$. In convenient units, $\lambda_e(in\ Angstroms) = \sqrt{150.5/E_{kin}(in\ eV)}$. Thus, a 150 eV electron has a wavelength of about 1 Å, and a 1500 eV electron of about 0.3 Å, and these numbers are comparable to atomic dimensions. The outgoing photoelectron will elastically scatter from neighboring atoms j to produce scatterered-wave components ϕ_j. This process is describable in first approximation by plane-wave scattering, or more accurately by spherical-wave scattering. This scattering can be incorporated into a scattering factor f_j, which is furthermore found to be strongly peaked in the forward direction for energies above about 500 eV, as noted previously. The photoelectron wave components will also be inelastically attenuated as they traverse some total pathlength L in getting to the surface, with their *amplitudes* decaying as $\exp(-L/2\Lambda_e)$. Finally, they will be refracted at the inner potential barrier V_0. Summing up all wave components (unscattered and scattered) and squaring then yields the diffraction pattern. Due to the combined effects of the $1/r$ decrease in amplitude of ϕ_0 in moving away from the emitter and the inelastic scattering of all components, only atoms within some cluster surrounding the emitter (the dashed envelope) need to be considered in this sum, with the number of scatterers required varying from 5 or so to a few hundred, depending on the emitter position in the cluster and the photoelectron energy. Electrons can also be multiply scattered from several atoms in sequence, and accurate calculations of the resulting PD patterns require including this for

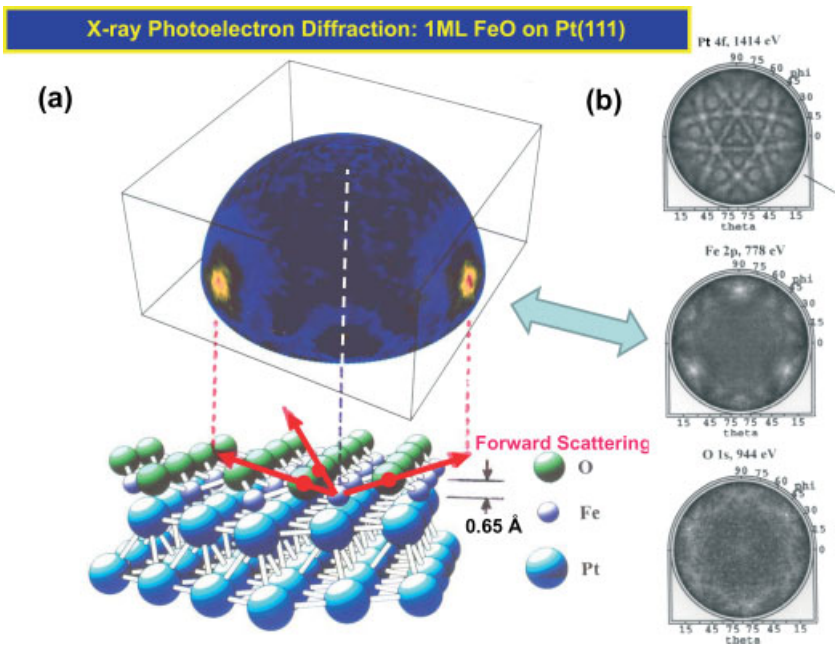

Figure 11. X-ray photoelectron diffraction at 1486.7 eV excitation from a monolayer of FeO grown on Pt(111). (a) A full-hemisphere pattern for Fe 2p emission is shown, above the atomic geometry finally determined for this overlayer. (b) Diffraction patterns simultaneously accumulated for emission from Pt 4f (kinetic energy1414 eV), Fe 2p (778 eV), and O 1s (944 eV). From Y.J. Kim *et al.*, *Surf. Sci.* **1998**, *416*, 68. Reprinted with permission.

many cases, especially if scatterers are somehow lined up between the emitter and the detection direction, as is the case along low-index directions in multilayer emission from a single crystal. Various programs are now available for calculating XPD patterns, with one web-based version being particularly accessible[45] and other programs also available.[46]

As one example of a PD pattern, we show in Fig. 11(a) the full-hemisphere intensity distribution for Fe 2p emission at 778 eV (λ_e = 0.44 Å) from a monolayer of FeO grown on a Pt(111) surface.[47] At this energy, the forward-peaked nature of f_O is observed to create strong peaks in intensity along the Fe–O bond directions. The angle of these peaks can furthermore be used to estimate the distance between the Fe and O atoms in the overlayer, and it is found to be only about half that for similar bilayer planes in bulk FeO, as illustrated in the bottom of Fig. 11(a). Figure 11(b) also illustrates the element-specific structural information available from XPD. The Pt 4f XPD pattern from the same sample is rich in structure due to the fact that emission arises from multiple depths into the crystal, with forward scattering producing peaks and other diffraction features along low-index directions. The Fe 2p pattern is here just a projection onto 2D of the 3D image in Fig. 11(a). The O 1s pattern shows only very weak structure, as the O atoms are on top of the overlayer, with no forward scatterers above them, and only weaker back scattering contributing to the diffraction pattern. Comparing the Fe and O patterns thus immediately permits concluding that Fe is below O in the overlayer, rather than vice versa.

Other examples of PD in the study of clean surfaces, adsorbates, and nanostructure growth appear elsewhere,[6,44,48] including a discussion of an alternative method of PD measurement in which the geometry is held fixed and the photon energy is scanned.[6,49]

Finally, we note that a PD pattern can to a first approximation be considered a hologram,[50] as suggested by the notation of reference wave and object wave in Fig. 10(a).

This has led to a number of studies in which diffraction patterns at various angles and/or various energies have been mathematically transformed so as to directly yield atomic positions in space.[51] More precisely, if the PD intensities $I(\vec{k})$ are measured over several angles and/or energies, equivalent to some volume in $\vec{k}$-space, and then normalized by subtracting out the smoother unscattered intensity profile I_0 corresponding to the reference wave (*cf* Fig. 10(b)) to yield a function $\chi(\vec{k}) = [I(\vec{k}) - I_0(\vec{k})]/I_0(\vec{k})$, then the holographic image of the atoms neighboring the emitter $U(\vec{r})$ can be obtained from

$$U(\vec{r}) = \left| \iiint \chi(\vec{k}) exp[i\vec{k} \bullet \vec{r} - ikr] d^3k \right| \quad (10)$$

where the exponential phase factor is that appropriate to the phase difference between the reference wave and an object wave scattered from point $\vec{r}$, and the integral is over the volume in $\vec{k}$-space covered by the data points.

In Fig. 12, we show a holographic image obtained using Cu 3p photoelectron intensities above a Cu(001) surface, with the emitter (e) as the central reference point.[52] These images were actually obtained using a differential approach in which two holograms at slightly different energies are subtracted from one another so as to suppress forward scattering effects, which are deleterious as far as holography is concerned. Using this approach, it is clear that one can image about 15 near-neighbor atoms below and to the sides of the emitter. Other future possibilities with photoelectron holography are discussed elsewhere.[51]

Valence-Level Photoemission

Band-Mapping in the Ultraviolet Photoemission Limit

At lower energies of excitation, especially below roughly 100 eV, photoemission spectra are routinely used to map the band structure of solids and surfaces, and this is one of the most powerful applications of photoelectron spectroscopy. This ability is due to

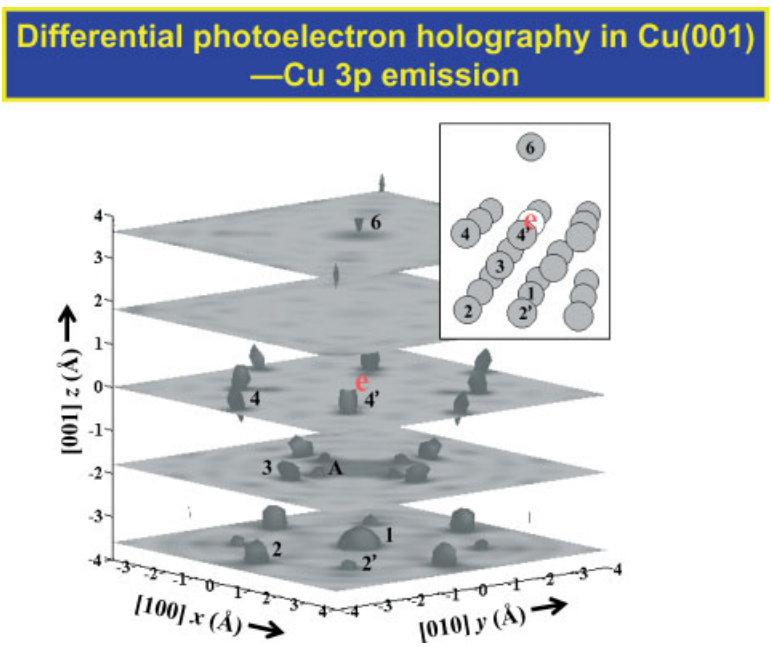

Figure 12. Holographic image of the atoms neighboring a given reference Cu atom below a Cu(001) surface. The typical reference emitter atom is noted by 'e', and the neighboring atoms are indicated in the inset. The data yielding this image consisted of Cu 3p spectra at 25 kinetic energies from 77 to 330 eV and over 65 directions, thus representing about 1600 data points in k-space. Based on work reported in Ref. [50].

the fact that the excitation can be considered to be dominated by so-called 'direct transitions' (DTs) in which an occupied initial one-electron Bloch-wave state $\varphi(E_i, \vec{k}_i)$ at energy E_i and wave vector $\vec{k}_i$ can in the dipole limit only make a transition to a final state with wave vector $\vec{k}_f = \vec{k}_i + \vec{g}$, where $\vec{g}$ is some reciprocal lattice vector associated with the crystal structure under investigation. The relevant vector quantities and conservation equations are illustrated in Fig. 13. Determing $\vec{k}_f$ inside the surface from a measurement of $\vec{K}_f$ outside the surface and then the set of $\vec{g}$ vectors which project it back into the reduced Brillouin zone (BZ) in which the band structure is usually described thus permits directly measuring $E_{binding}(\vec{k}_i) = E_i(\vec{k}_i)$, the band structure, or if final-state screening and many-electron excitations are taken into account, more properly the spectral function as calculated from some sort of many-electron theory.[5] The need to accurately define the direction of $\vec{K}_f$, and thus also $\vec{k}_f$ inside the surface, leads to such measurements often being termed angle-resolved photoemission or ARPES. If the final photoelectron state is high enough in energy, it can be approximated as a free-electron, with $E_f(\vec{k}_f) \approx p_f^2/2m_e = h^2k_f^2/2m_e$, where m_e is the electron mass. This is just the non-relativistic kinetic energy inside the surface, which is higher by V_0 than the kinetic energy outside of the surface (*cf* Figs 10 and 13). In convenient units, $k_f(\text{Å}^{-1}) = 0.512[E_f(\text{eV})]^{1/2}$.

To link the direct-transition picture to fundamental matrix elements via Eqn (3), we can simply convert $|\hat{\varepsilon} \bullet \langle\varphi_{photoe}|\vec{r}|\varphi_{nlj}\rangle|^2$ to a transition between Bloch functions, yielding in a one-electron picture

$$I(E_f, \vec{k}_f) \propto \left|\hat{\varepsilon} \bullet \left\langle\varphi_{photoe}(E_f = h\nu + E_i, \vec{k}_f = \vec{k}_i + \vec{g}|\vec{r}|\varphi(E_i, \vec{k}_i)\right\rangle\right|^2 \quad (11)$$

with obvious notation and an explicit inclusion of energy and wave-vector conservation in the final state. Figure 13 also illustrates that, in traveling from the interior of a solid to the surface, inelastic attenuation can occur (just as in the three-step model of core emission). Two additional things occur in crossing the surface: the electron wave can be scattered from a surface reciprocal lattice vector $\vec{g}_{surf}$ that may be different from the bulk $\vec{g}$ vectors, and finally, in traversing the surface potential barrier V_0, the electron is decelerated and refracted from direction $\vec{k}_f$ into a new direction $\vec{K}_f$, which is actually what is measured. Momentum conservation in this last step assures that the component of $\vec{k}$ parallel to the surface is conserved, and this is very useful in studying systems whose electronic structure can be considered to be approximately two-dimensional and in the surface plane (as for example, surface electronic states and the high-temperature superconductors).

Having thus introduced the basic physics of ARPES, we now consider a couple of illustrative examples, including looking ahead to what happens as the photon energy is gradually increased into the keV or even multi-keV regime. In Fig. 14, we show some recent ARPES results obtained for W(110) with an excitation energy of 270 eV and a display-type detection system such as that shown in Fig. 1(c).[53] In Fig. 14(a), we show the one-electron energy bands for W, plotted along the Γ-to-*N* direction in the reduced BZ, whose high-symmetry points are shown in Fig. 14(b). In Fig. 14(c), we show as a color contour plot experimental data obtained over an emission angle range that corresponds closely to scanning the emission point roughly along Γ-to-*N* in the BZ, or more precisely along the violet curves shown in Fig. 14(b). Also overlaid in Fig. 14(c) are the allowed DTs expected using a simple free-electron model for the final state; the agreement as to the positions and profiles of most of the experimental features, and the close correspondence to Fig 14(a) confirms for this case the usage of ARPES for mapping band structure. But the simple model does not attempt to calculate the actual matrix element in Eqn (11), so there is no information in it concerning intensities. To address this, we show as a color contour plot in Fig. 14(d) the results of a much more sophisticated theoretical calculation which treats the emission process in one-step, explicitly calculating matrix elements within a layer Korringa–Kohn–Rostoker (KKR) formalism.[53] The

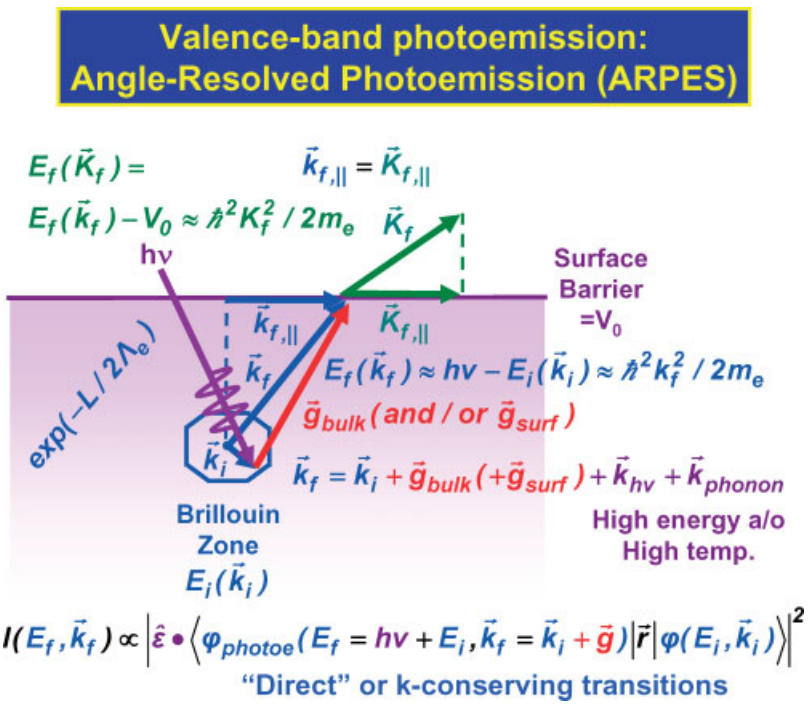

Figure 13. Illustration of the basic processes and conservation laws in angle-resolved photoemission from valence levels.

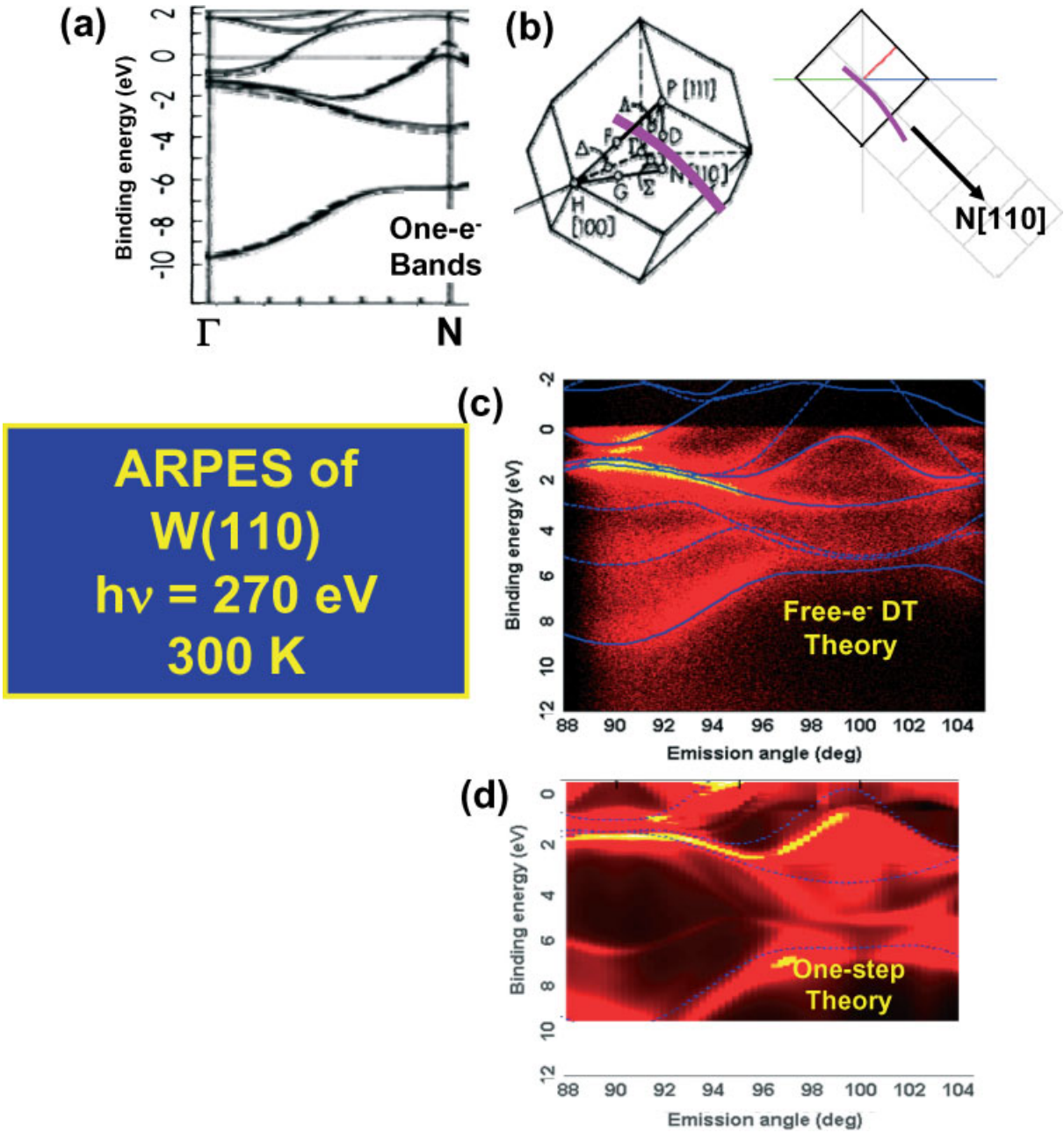

Figure 14. Angle-resolved photoemission from W(110) with a photon energy of 260 eV. (a) The theoretical energy bands of W, plotted along the Γ-to-*N* direction that is very close to that sampled in the experiment. (b) The Brillouin zone of W, with the violet curve indicating the points sampled by direct transitions for the particular experimental geometry and angle scan involved. (c) An energy-*versus*-angle plot, or equivalently energy-*versus*-$\vec{k}$ plot, with brighter contours representing higher intensity. Also shown are the positions allowed via direct-transition wave-vector conservation and assumed free-electron final states. (d) Analogous color plot of more accurate one-step model calculations of this data. L. Plucinski, J. Minar and C. S. Fadley, unpublished data.

calculations in Fig. 14(d) agree well with the experimental results in Fig. 14(c) as to which features should be most intense, indicating the importance of matrix element effects in interpreting ARPES data in the future.

As a final example of ARPES, we consider its application to ferromagnetic Ni.[54] The experimental results in Fig. 15(a), (c), (d) and (e) were obtained in a similar scan of the polar angle above an Ni(111) surface, but with a much lower excitation energy of 21.21 eV that is in fact more typical of many ARPES measurements, and a focus on a smaller range of energies close to the Fermi level. In the room temperature data of Fig. 15(a), which correspond to $T/T_C = 0.80$, one clearly sees two split bands going up to the Fermi level, with intensity in fact visible above that level due to thermal excitation of electrons, and division of the data by the Fermi function from statistical physics. This splitting corresponds to a direct measurement of the expected exchange splitting of spin-up and spin-down bands in nickel, and is in good agreement with the results of theoretical calculations shown in Fig. 15(b), although theory predicts a splitting about 30% too large, probably due to a lack of adequately treating

many-electron effects in the photoemission process. In panels (c)–(e) of Fig. 15 are shown measurements for the same polar scan, but at three temperatures spanning from well below to significantly above T_C. Here one sees what is probably the closing of the exchange splitting as temperature increases to the point where long-range ferromagnetic order is lost, again a most fundamental observation in the electronic structure of a ferromagnet.

There are many other examples of ARPES being used to study the fundamental properties of electronic structure, including strongly correlated materials such as high T_C[55] and colossal magnetoresistive oxides,[56] surface states,[57] and quantum well states in nanoscale layers.[58] A powerful aspect of many of these studies that we have not focussed on here is looking only at the electrons near the Fermi level, with these being key to transport in some of the cited examples. Such Fermi surface mapping is thus another significant aspect of current ARPES studies.

Densities of States in the X-Ray Photoemission Limit

As energy is increased in valence-level photoemission, several factors act to smear out the region in $\vec{k}$-space that is sampled, finally leading to a measurement that in first approximation measures the total density of electronic states at a given binding energy, as summed over all $\vec{k}$ values and modulated by appropriate matrix elements:

- As the magnitude of $\vec{k}_f$ increases, the finite angular resolution of the electron spectrometer implies that the definition of points in the BZ is smeared out, as illustrated in Fig. 16(a) for photoelectron excitation from W along the [010] direction with a typical XPS energy of 1254 eV, and in Fig. 16(b) for excitation at 10 000 eV. With the moderately high angular resolution of $\pm 1.5^\circ$ shown in (a), it is clear via the shaded disk that the set of $\vec{k}_i$ values involved is significantly broadened with respect to the size of the BZ. However, by now, 2D imaging spectrometers such as that shown in Fig. 1(c) have increased the resolution to $\sim 0.1^\circ$, so this may not be the most serious factor, at least

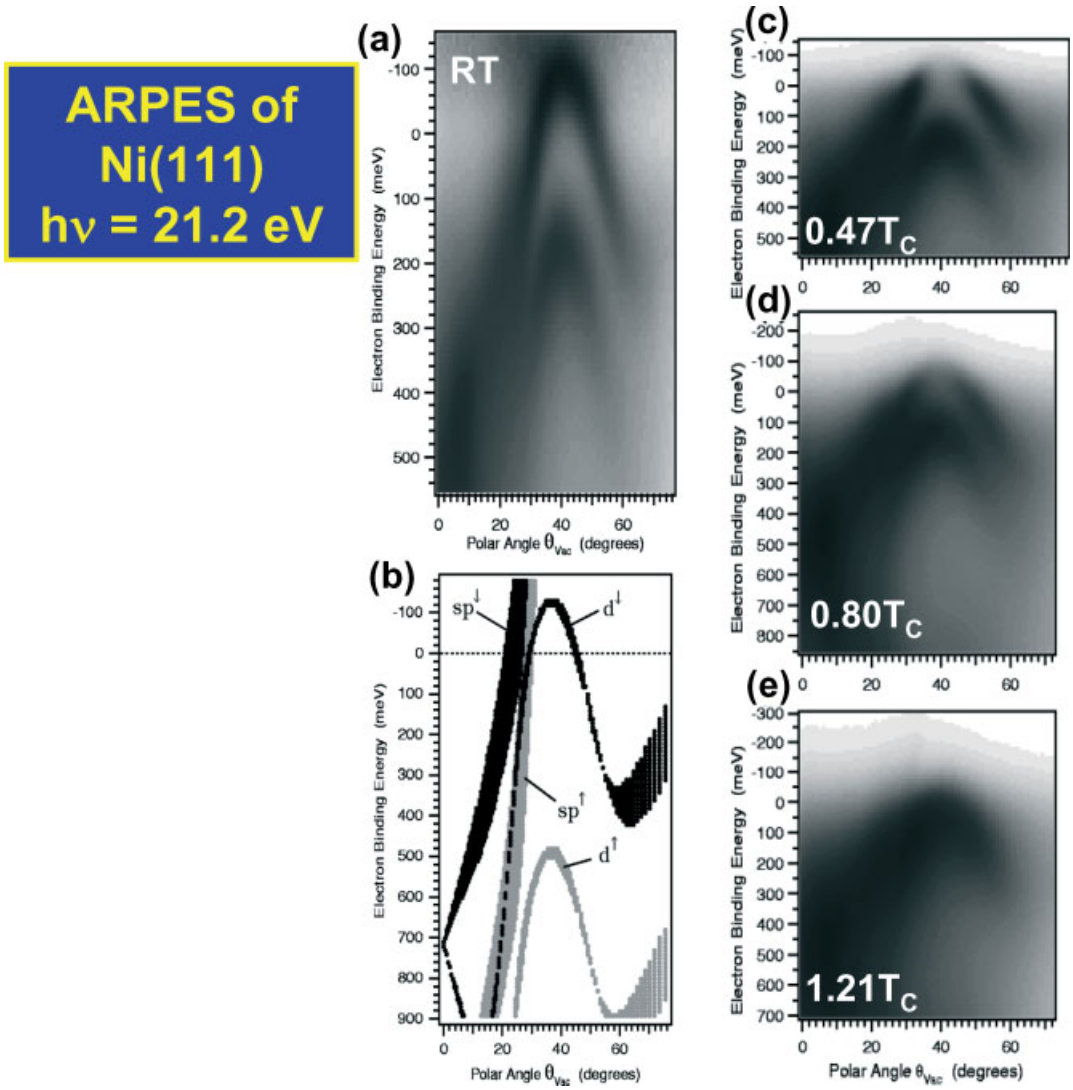

Figure 15. Angle-resolved photoemission from ferromagnetic Ni(111) with a photon energy of 21.2 eV. (a) Experimental data at room temperature and thus below the Curie temperature: the splitting of the bands due to the exchange interaction is seen. (b) Theoretical layer-KKR calculation of the bands involved in (a). (c) The temperature dependence of the spin–split bands, in going from below to above the Curie temperature. From Kreutz *et al.*, Reprinted with permission.

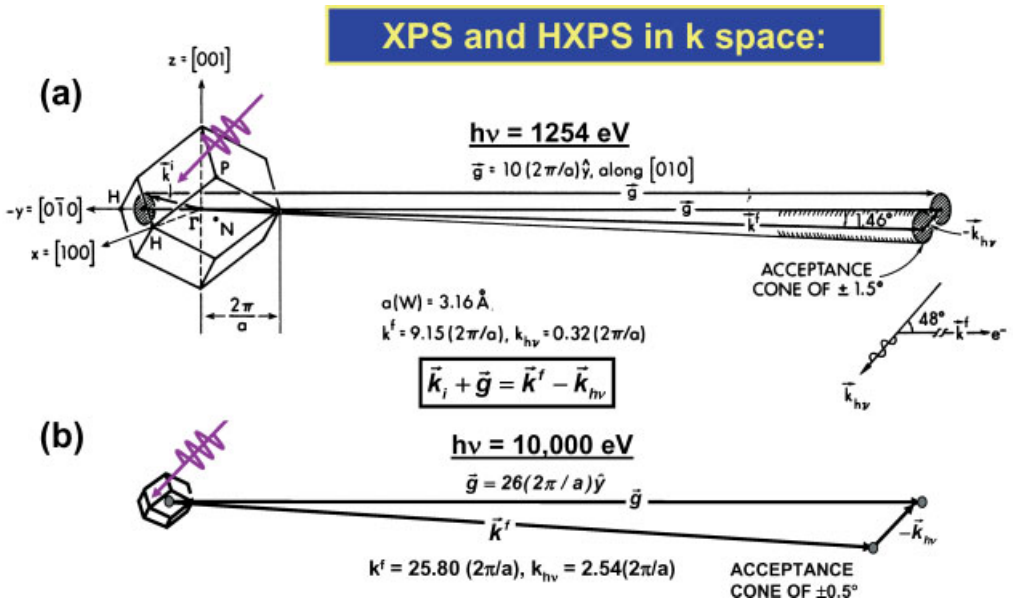

Figure 16. Illustration of $\bar{k}$ conservation in valence photoemission from W at two different photon energies: (a) 1253.6 eV, a typical soft X-ray energy also available with laboratory sources, and (b) 10,000 eV, a hard X-ray energy that is of interest for the future.

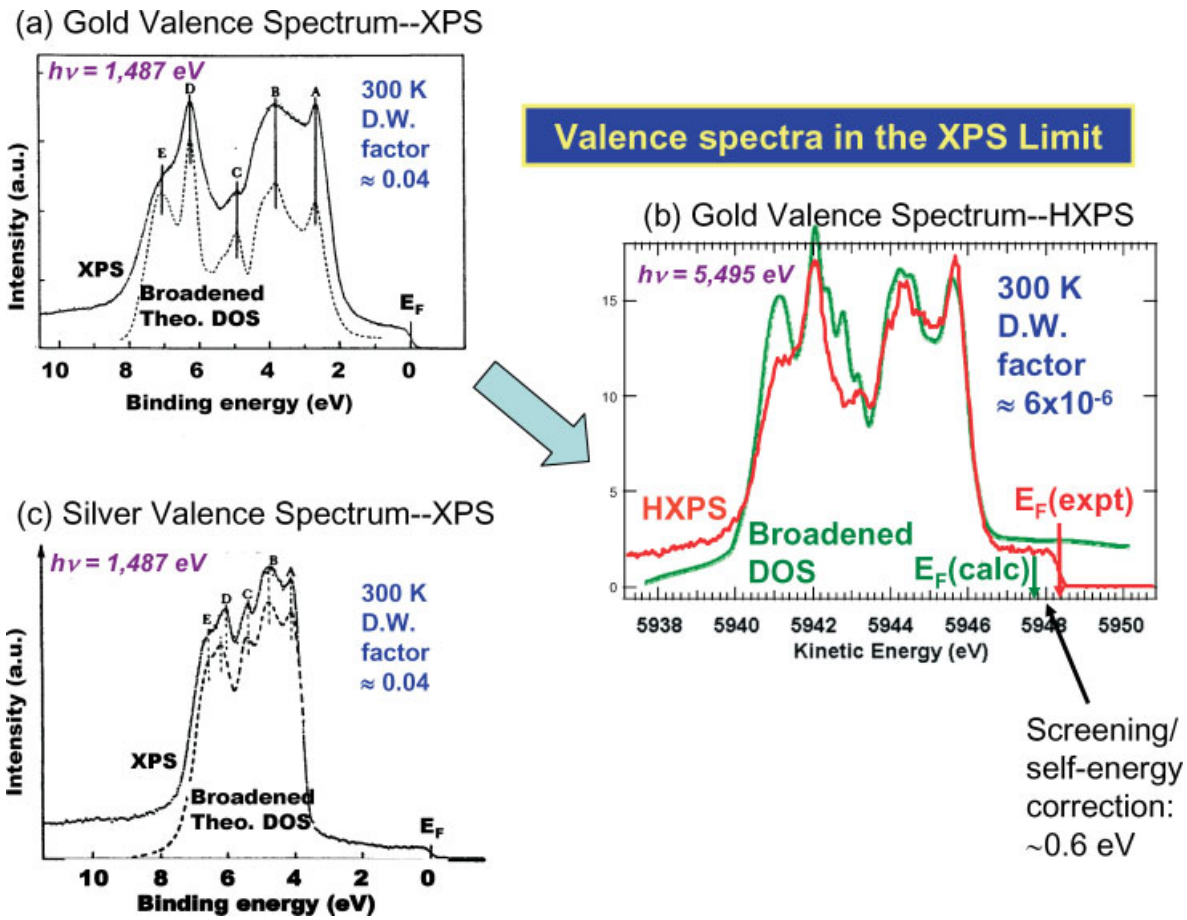

Figure 17. Valence photoelectron spectra from the noble metals Ag and Au in the XPS or density of states limit. In (a) and (b), Au spectra with 1.5 and 4.5 keV excitation are shown. In both cases, the experimental results are compared with theoretical densities of states based on local-density theory. In (c), the same comparison is made for 1.5 keV excitation of Ag. Experimental data in (a) and (b) from K. Siegbahn and Y. Takata, theory in (b) from Z. Yin and W. E. Pickett. (c) is reprinted from A. Barrie and N. E. Christensen, *Phys. Rev. B* **1976**, *14*, 244, with permission.

for energies up to 1 keV or so. Nonetheless, Fig. 16(b) makes it clear that angular resolution must be increased significantly if the excitation energy goes up into the 10-keV regime, for which an angular resolution of 0.5° yields about the same fractional broadening in the BZ as 1.5° does for 1.2 keV excitation.

- Also as the magnitude of $\vec{k}_f$ increases, the effects of phonon creation and annihilation in the photoemission process must be considered. As an alternate view of this, the DTs in photoemission can be considered heuristically as a type of Bragg reflection, with $\vec{g} = \vec{k}_f - \vec{k}_i$ providing the additional momentum to the photoelectron. Thus, by analogy with normal diffraction in crystals, one might expect to suppress the intensity in the DT features due to atomic vibrations that reduce the degree of translation symmetry of the crystal according to a Debye-Waller factor, which can be written as: $W(T) \approx exp[-g^2 < u^2(T) >]$, with $< u^2(T) >$ the mean-squared vibrational displacement at temperature T. This factor effectively allows for the transfer of momentum to phonons, further smearing the specification of $\vec{k}_i$ in the BZ (*cf* Fig. 13). Qualitatively, one expects the Debye-Waller factor to represent the fraction of intensity in DT features that is not influenced by phonons. Calculations of this for various elements indicate that such effects often will give rise to essentially full BZ averaging at excitation energies in the 1–2 keV regime that are typical of classical XPS measurements.[59]
- A final effect at higher excitation energies has to do not with smearing of the $\vec{k}_i$ definition in the BZ, but with a shift of position due to the *photon* momentum or wave vector, as given by $k_{h\nu} = 2\pi\nu/c$. In convenient units, this is $k_{h\nu}(in\ Angstroms^{-1}) = 0.000507(Photon\ energy\ in\ eV)$. The need to consider this in fact involves a breakdown of the dipole approximation for the interaction of the radiation with the system. Thus, the overall wave-vector conservation equation is as given in Fig. 13 or 16(a), with the magnitude of $\vec{k}_{h\nu}$ being explicitly shown for excitation at both 1254 and 10 000 eV. It is clear that such effects need to be allowed for at such high excitation energies, as first pointed out some time ago.[59] However, they are usually neglected at energies less than about 100 eV, for which $k_{h\nu} < 0.05$ Å^{-1}.

Taking the first two of these effects into account, one expects higher-energy valence spectra to reflect the total density of states (DOSs) of the material, modulated by whatever matrix elements are appropriate to the different types of states involved, as e.g. *nd versus* $(n+1)$s and $(n+1)$p states in transition metals, with $n = 3$, 4, or 5. This is often termed the 'XPS limit'.

To illustrate this XPS limit, we show in Fig. 17(a) and (c) the valence spectra for Au[60] and Ag[61] excited by 1.5 keV photons, as compared with broadened theoretical densities of states. For these metals at room temperature, the Debye-Waller factors with

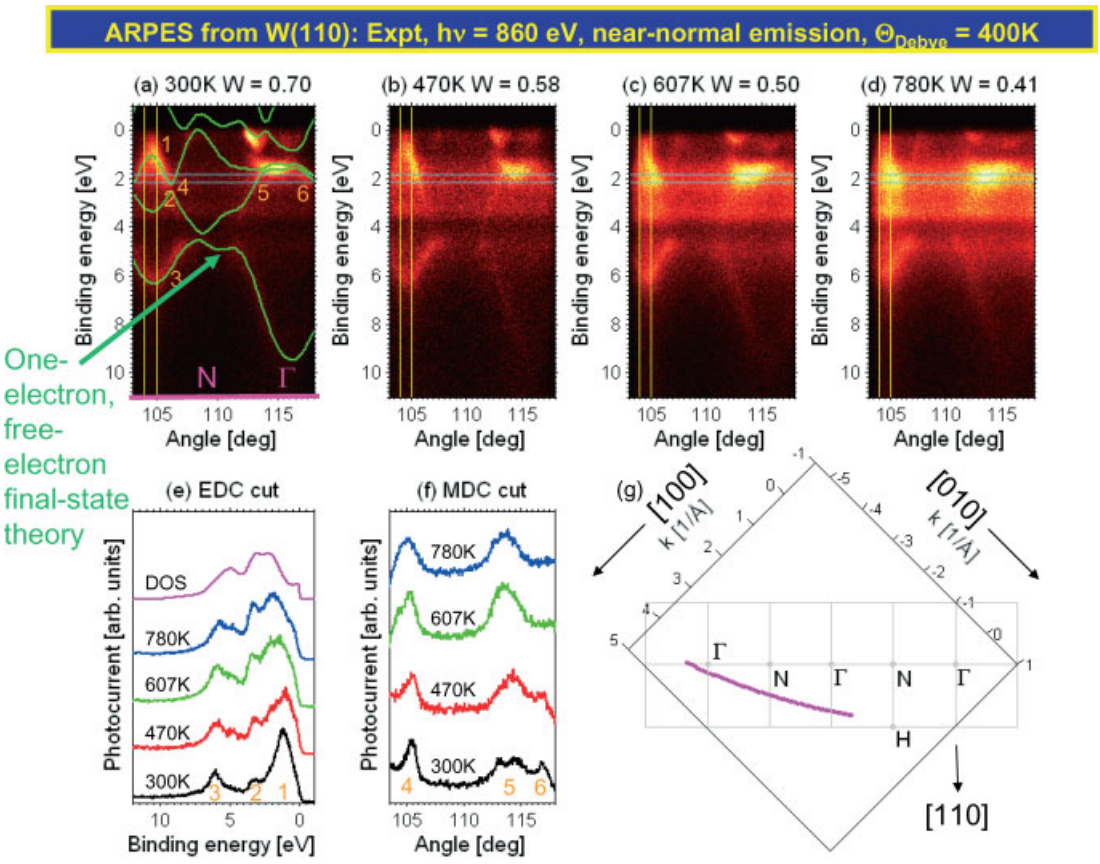

Figure 18. Temperature-dependent angle-resolved photoemission data from W(110) at an excitation energy of 860 eV. (a)–(d) Energy-*versus*-angle (energy-*versus*-$\vec{k}$) plots at four temperatures, with phonon-induced smearing of features evident as T is raised. From left to right in each, the N to Γ line in the Brillouin zone is approximately sampled. (e) Energy distribution curves (EDCs) integrated over a narrow angle (or $\vec{k}_i$) range for all four temperatures, with the curve at highest temperature also compared to a suitably broadened W density of states. (f) Momentum distributions curves (MDCs) integrated over a narrow binding energy range near 2 eV for all four temperatures. (g) The approximate region in $\vec{k}_i$ sampled by this data. From L. Plucinski *et al*., *Phys. Rev. B* **2008**, *78*, 035108. Reprinted with permission.

this excitation energy are very small, at about 0.04, so one expects rather full BZ averaging, especially in view of the rather large angular acceptances of the spectrometers involved. That this is indeed the case is evident from the very good agreement between the spectra and the broadened densities of states. Figure 17(b) further shows what occurs when the photon energy is increased to 5.5 keV,[62] for which the energy resolution is in fact better than for the 1.5 keV data, at about 80 meV; the Debye-Waller factor is only about 6×10^{-6}; and the fine structure is again found to agree rather well with a suitably broadened DOSs from theory based on the local-density approximation (LDA).[63] Note, however, that it is necessary to shift the theoretical DOSs by about 0.6 eV to higher binding energy to best match the position of the dominant 5d-band DOSs features. This kind of discrepancy is well known in such comparisons of experiment with LDA theory, and is due to the fact that the different states in Au (more localized Au 5d *versus* more delocalized and free-electron-like Au 6s,6p) exhibit different screening/self-energy corrections due to many-electron interactions. Also, comparing Fig. 17(a) and (b), we note the same sorts of minor discrepancies between theory and experiment in the dominant Au 5d region, which may have to do with matrix-element effects that are not included when simply comparing experiment to the DOSs.

Thus, even though there is inherently more information content in an ARPES spectrum for which BZ selectivity is involved, spectra in the XPS limit still provide important clues as to the electronic structure of any material, and if they are measured at higher excitation energies, they also more closely express bulk, rather than surface, electronic properties.

As a last topic in this section, we consider an intermediate case for which both BZ selectivity and phonon smearing are involved. We show in Fig. 18(a)–(d) a set of angle-resolved data from W(110) obtained with an intermediate energy of 870 eV, and at four different temperatures, which permits assessing the influence of phonons in a more quantitative way.[53] The four experimental panels clearly show band-mapping features, and in fact are also along the Γ-to-*N* direction sampled at lower energy in Fig. 14, but running in the opposite direction. Note the similar positions and shapes of features between the two figures. However, it is also clear that raising the temperature stepwise from 300 to 780 K, or from 0.75 times the Debye temperature that is characteristic of the W phonon spectrum to 1.95 times that temperature involves a smearing of those features and a significant gain of intensity in other parts of the angle-resolved data. In Fig. 18(e) we show EDCs at different temperatures as derived by integrating intensity over a small band in $\vec{K}_f$ for emission from near a high-symmetry point in the BZ, and in Fig. 18(f) momentum distribution curves (MDCs) derived by integrating over a small band in energy at about 2 eV binding energy. A broadened DOS is also shown in Fig. 18(e) for comparison. Not surprisingly both EDCs and MDCs show a loss of fine structure as temperature is raised, with the highest temperature data beginning to converge to the W DOS, but clearly not reaching it, especially for the MDCs, which would be flat lines in this limit. Thus, the DOS limit is not quite reached by 780 K for this case, consistent at least qualitatively with the Debye-Waller factor of 0.41; that is, roughly 40% of the intensity is still estimated to be via DTs. Not shown here are the results of one-step KKR calculations for comparison to this data, which agree very well with the positions and intensities of all features seen in experiment, but do not at their present level of describing phonon effects correctly predict the smearing of features at higher temperatures.[53]

Looking ahead, we note that the results of Fig. 18 suggest it should be possible to carry out more bulk-sensitive electronic structure studies at higher photon energies than have been typically employed in the past. However, a note of caution is in order, as W is one of the most cooperative materials in this respect,[59] and it will in general require some combination of high angular resolution, not-too-high photon energy, and cryogenic cooling to achieve this for other materials, as discussed recently.[53]

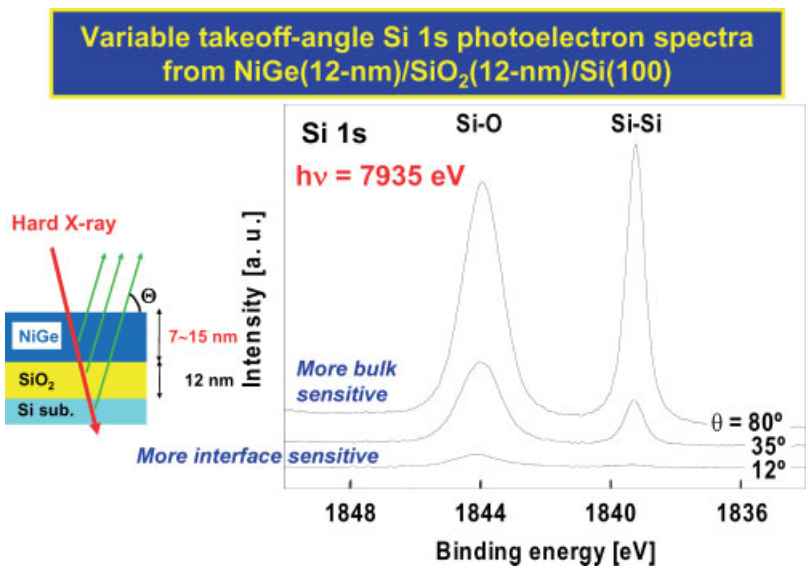

Figure 19. Application of hard X-ray photoemission to a multilayer nanolayer structure combining an Si semiconductor substrate, an insulating SiO_2 layer, and a magnetic NiGe overlayer. Si 1s spectra have been obtained with 7.9 keV photons, and a variation of electron takeoff angle. Chemically-shifted Si and oxidized Si peaks are easily resolvable, and their relative intensities change markedly as the degree of surface sensitivity is enhanced at lower takeoff angles (*cf* **Fig.** 3(a)). From T. Hattori *et al*., *Int. J. High Speed Electron. Syst.* **2006**, *16*, 353. Reprinted with permission.

Some New Directions

Photoemission with Hard X-Rays

Within the last few years, interest has arisen in carrying out core and valence photoemission with excitation energies significantly above those of up to about 2 keV used to date. Such measurements have been carried out in the 3–15 keV regime, and a small number of groups in Europe and Japan have succeeded in designing beamline-end station combinations that permit carrying out such experiments with acceptable intensity/resolution combinations.[16,17]

The principal reason for this emerging interest lies in the extrapolation of curves such as those in Fig. 3 to higher energies, which we have noted involves inelastic Λ_e values of 50–200 Å. Thus, photoemission becomes a much more bulklike probe, and one that can look more deeply into multilayer or complex nanostructures. Two international workshops have so far explored this topic and its future.[16,17]

As one example of what has been termed hard XPS (HAXPES or HXPS), we show in Fig. 19 some Si 1s spectra excited from a multilayer structure of 120 Å of NiGe on top of 120 Åof SiO_2 on top of a deep Si substrate by 7.9 keV photons.[64] The resulting kinetic energies of about 6.1 keV permit seeing both types of Si atoms, with the 1s spectra showing a chemical shift associated with elemental Si in the substrate and oxidized Si in the overlayer. Furthermore, varying the takeoff angle from near normal to more grazing so as to enhance surface sensitivity is found to dramatically change the intensity ratio of element to oxide. These data thus illustrate the power of HXPS, or more particularly angle-resolved HXPS (ARHXPS), to look into multilayer device structures or other structures of relevance to technology or environmental science. Beyond being able to probe more deeply below the surface, ARHXPS has additional advantages as compared to standard ARXPS; in analyzing data, it is possible to much more nearly neglect effects due to elastic scattering (which is much more forward peaked), refraction due to the inner potential (which becomes much smaller compared to the electron kinetic energy), and surface inelastic scattering (which becomes negligibly small).[65,66]

As another example of what has been seen in HXPS, we show in Fig. 20 temperature-dependent Mn 2p spectra from the same type of colossal magnetoresistive oxide sample involved in Fig. 5. Here, data in Fig. 20(a) with an excitation energy of 1090 eV, corresponding to kinetic energies of ~450 eV, and an inelastic attenuation length of ~10 Å,[15,67,68] are compared with data in Fig. 20(b) obtained at 7700 eV, corresponding to kinetic energies of ~7050 eV, and an inelastic attenuation length of ~85 Å.[15,69] Thus, the latter is a much truer sampling of bulk properties. Although the general shape of the doublet is the same at the two energies, there are two significant differences. First and most obvious in the hard X-ray spectrum is a small, but very sharp, satellite that appears below T_C (which is 370 K for this material) on the low binding energy side of the $2p_{3/2}$ peak, but which is absent in the lower-energy more-surface-sensitive spectrum. There is also an indication of the same satellite, although less well resolved, on the $2p_{1/2}$ peak, as indicated by the arrow. This type of satellite has been observed in HXPS from other manganite samples, and it has been interpreted as a screening satellite associated with highly delocalized electrons,[70–72] with the implication that it requires the extended volume of a more bulk-sensitive measurement to see it. This satellite is also observed to slowly disappear as temperature is raised, which implies a connection with either magnetic order or a lattice that is free of the kind of Jahn-Teller distortion above T_C that is thought to produce the effects seen in Fig. 5.[34] A second difference between the hard X-ray and soft X-ray spectra is that a chemical shift with soft X-ray excitation of both Mn 2p components to higher binding energy by about 0.7 eV on lowering the temperature to about 150 K that has been linked to the O-to-Mn charge transfer[67,68] discussed in connection with Fig. 5 is difficult to discern with hard X-ray excitation. This suggests that the effects seen in Fig. 5 are more localized near the surface.

One factor that will however limit the energy resolution achievable with HXPS, particularly for lighter atoms and/or solids with lower Debye temperatures, is the recoil energy involved in

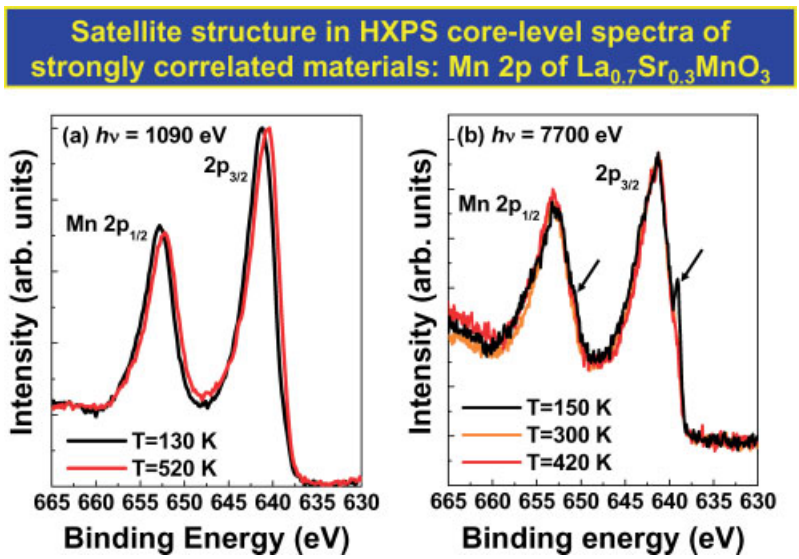

Figure 20. Temperature-dependence of Mn 2p spectra from a freshly fractured surface of $La_{0.7}Sr_{0.3}MnO_3$, of the type studied in Fig. 5. (a) With soft X-ray excitation at 1090 eV, a chemical shift to lower binding energy is seen on going above the Curie temperature. (b) With hard X-ray excitation at 7.7 keV, this shift is not evident, and a sharp low-binding-energy satellite is observed for a temperature below T_C. From F. Offi *et al.*, *Phys. Rev. B* **2008**, *77*, 174422. Reprinted with permission.

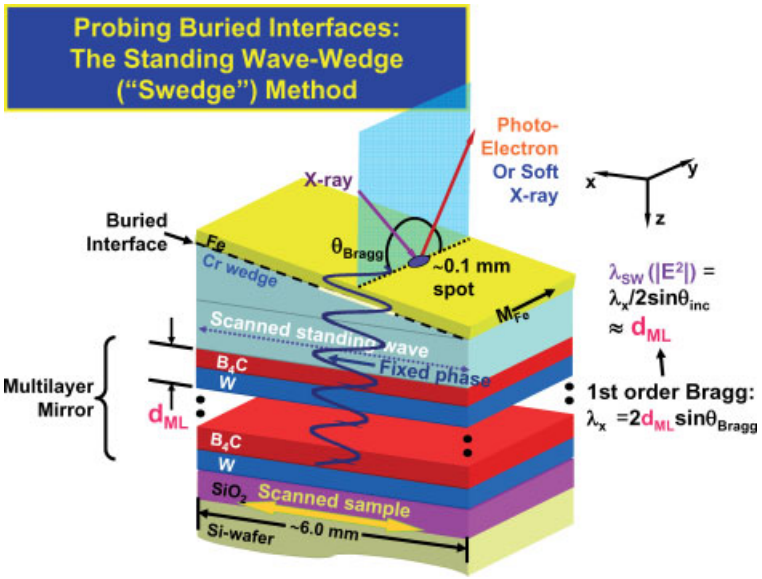

Figure 21. Schematic illustration of the simultaneous use of an X-ray standing wave created by reflection from a multilayer mirror plus a wedge-profile overlayer sample to selectively study buried interfaces and layers – the ' swedge' method. In the example here, a strong standing wave (SW) is created by first-order Bragg reflection from a multilayer made of repeated B_4C/W bilayers, and a Cr wedge underneath an Fe overlayer permits scanning the SW through the Fe/Cr interface by scanning the sample along the *x* direction. The two relevant equations for predicting the period of the standing wave along the *z* direction are also given.

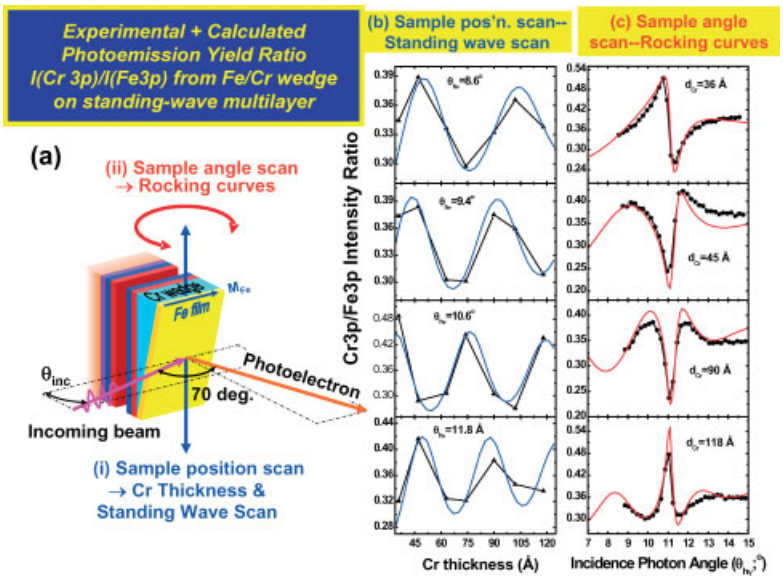

Figure 22. (a) The two types of scans possible in the swedge method: (i) Scanning along *x* or wedge thickness with θ_{inc} fixed at the Bragg angle to yield a direct scan of the standing wave through the layers above the wedge, and (ii) scanning the incidence angle over the Bragg angle with *x* (or Cr thickness) fixed to yield a rocking curve. (b), (c) Experimental and calculated Cr3p/Fe3p ratios for these two types of scans. The best-fit theory curves are for the parameters shown at the left of Fig. 24(a). (b) and (c) reprinted with permission from S.-H. Yang *et al*., *J. Phys.: Condens. Matter* **2002**, *14*, L406.

conserving both energy and momentum during photoelectron emission.[73,74] The recoil energy will be given approximately by

$$E_{recoil} \approx \frac{\hbar^2 k_f^2}{2M} \approx 5.5 \times 10^{-4} \frac{E_{kin}(eV)}{M(amu)} \qquad (12)$$

where *M* is the emitter mass. Recoil has been shown experimentally to contribute to energy shifts and broadenings in both core and valence level spectra.[73,74] As representative numbers at the extreme excitation energy of 10 keV, the recoil energy will be 6.0 eV for H, 0.5 eV for C, 0.1 eV for Ni, and 0.03 eV for Au.

A number of other papers on HXPS have by now appeared, and are presented in overview elsewhere,[16,17] but even at this early stage, it seems clear that such experiments have the potential to answer some key questions concerning the structure and composition of multilayer nanostructures, as well as the true bulk electronic structure of complex materials. As applied to valence spectra, it is likely that most HXPS spectra at moderate or higher temperatures will reflect the DOSs in the XPS limit, but with a spectrometer of high angular resolution (e.g. well below 0.1°), at lower excitation energies in the few-keV range and/or with cryogenic cooling, as well as with adequate correction

for photon momentum, it should be possible to do more bulk-sensitive band mapping for some materials,[53] even if not at the ultrahigh energy and angular resolutions available with much lower photon energies.

Photoemission with Standing-Wave Excitation

We have noted previously two ways to vary the surface sensitivity in photoemission: changing the photon energy so as to move along curves of the type in Fig. 3 and varying the takeoff angle, as indicated e.g. in Fig. 19. Both of these involve electron escape processes, so one can also ask if it is not possible to somehow tailor the photon wave field so as to provide a complementary avenue for varying surface sensitivity. Creating an X-ray standing wave is one method for doing this, and it has been found possible via this approach to selectively look at buried layers and interfaces,[31,75] as well as element-resolved densities of states,[76] in this way.

In Fig. 21, we illustrate one approach for using soft X-ray (or in the future also hard X-ray) standing waves to carry out more precise depth-resolved photoemission from multilayer nanostructures.[31] This approach combines a standing wave created by first-order Bragg reflection from a multilayer mirror of period d_{ML} with a sample that is grown on top of the multilayer, including a base layer of wedge profile. It is a simple matter to show that the profile of the first-order standing wave-modulated intensity, as given by $I_{h\nu}(x,y,z) \propto |\vec{E}(x,y,z)|^2$, where $\vec{E}$ is the electric field vector, will have a sinusoisal form with a period equal to the repeat distance of the diffracting planes or d_{ML}. If the standing wave is created by a typically well-focussed synchrotron radiation beam, then its dimensions will be much smaller than a typical sample, as indicated in the figure. Since the standing wave only exists in the region where the beam hits the sample surface, and its phase is locked tightly to the multilayer mirror, scanning the sample in the photon beam along the x direction in Fig. 21 effectively translates the standing wave along the vertical z direction through the sample. In the example shown, the standing wave would in particular scan through the Fe/Cr interface of interest, at some x positions being more sensitive to the Fe side and at some other positions being more sensitive to the Cr side. This standing wave/wedge approach has been termed the 'swedge' method'.[77,78]

Some results obtained with this method for the Fe/Cr interface are summarized in Figs 22–24. In Fig. 22(a), the two basic types of measurement possible are indicated: (i) a scan of sample position along x with the incidence angle fixed at or near the Bragg angle, as discussed previously; and (ii) a scan of incidence angle through the Bragg angle at fixed x, or equivalently fixed Cr thickness, which can be referred to by the usual term 'rocking curve'. The results of both types of scans on the Cr3p/Fe3p ratio are presented in Fig. 22(b) and (c). The roughly sinusoidal oscillations in this ratio in Fig. 22(b) clearly reflect the passage of the standing wave through the interface. Figure 22(c) shows the more complex forms that are characteristic of rocking curves, with dramatic changes in the

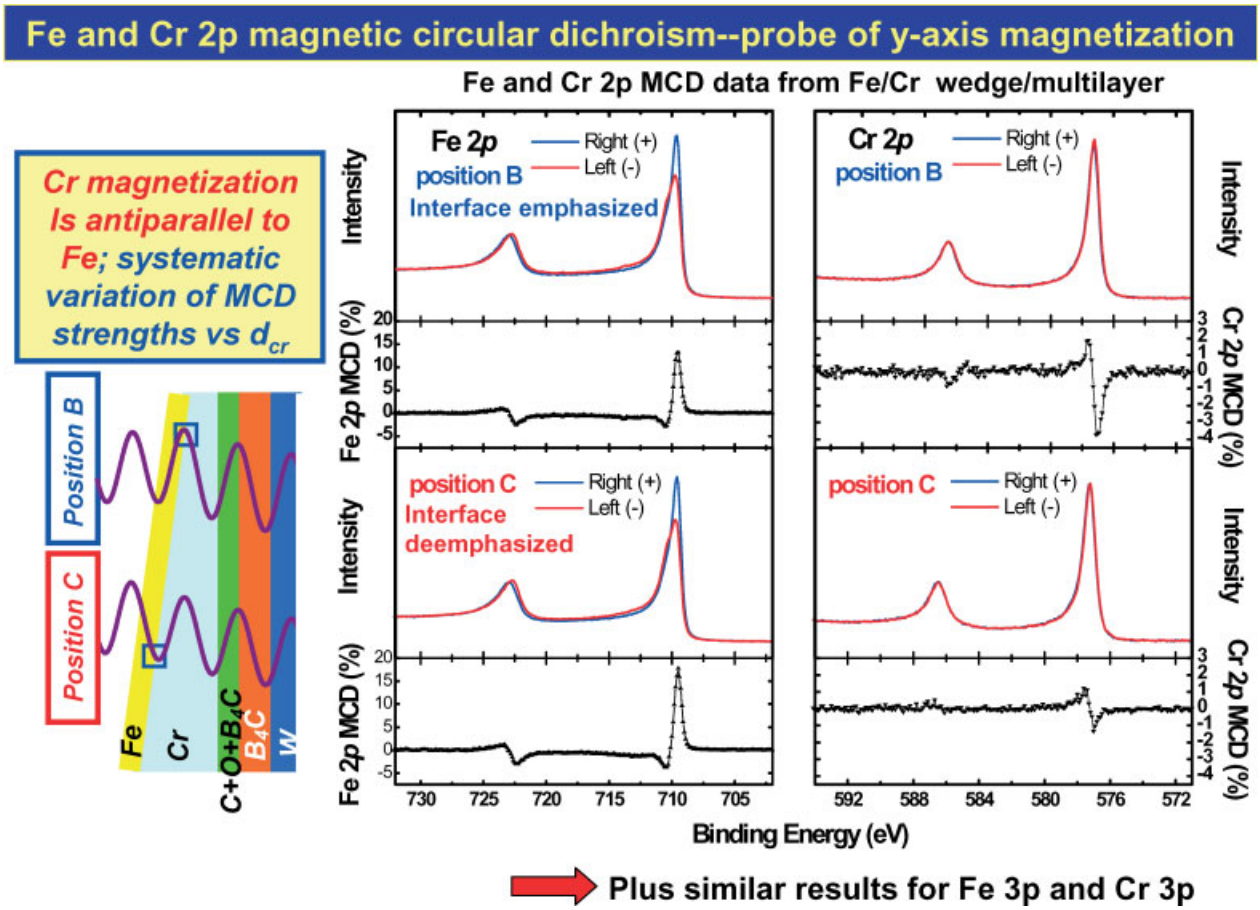

Figure 23. Experimental MCD data for Fe 2p and Cr 2p emission from the sample of Fig. 21, at two positions of the standing wave: emphasizing the interface (position B) and deemphasizing the interface (position C). From S.-H. Yang *et al.*, *J. Phys.: Condens. Matter* **2002**, 14, L406. Reprinted with permission.

ratio in this data also. Self-consistently analyzing these data with X-ray optical calculations of standing-wave photoemission[79] and only two variable parameters (the depth of onset of the change in the Fe composition and the width of a linear gradient as the interface changes from pure Fe to pure Cr) yields the excellent fits shown to both types of data, and the parameters given at the left of Fig. 24(a). In Fig. 23 are shown MCD data for both Fe 2p and Cr 2p emission, which have also been measured as the sample is scanned in the beam, with the variation as *x* or Cr thickness is varied being represented by the curves in Fig. 24(b). The relative signs of the MCD in Fig. 23 can be directly compared to those in Fig. 9(b), and also immediately imply that a small amount of Cr is oppositely magnetized compared to Fe, and that this must be induced by the ferromagnetic Fe layer, since Cr is normally antiferromagnetic. Further analyzing this data via X-ray optical calculations with only two parameters for Fe 2p and 3p MCD and two parameters for Cr 2p and 3p MCD yields the atom-specific magnetization profiles shown at right in Fig. 24(a). Thus, in this first published example, the swedge method permitted non-destructively determining the concentration profile through an interface, as well as the atom-specific magnetization contributions through it.

In more recent work, the swedge approach has also been used successfully to determine layer-specific densities of states that can be linked to changes in magnetoresistance as a function of nanolayer thicknesses.[75] Several other possible applications of it have also been suggested,[19,31,77,78] including going to harder X-ray excitation, for which reflectivities and thus standing wave strengths can be much higher.

Photoemission with Space and Time Resolution and at Higher Pressures

As Fig. 1(f) indicates, other dimensions of photoemission involve adding *spatial resolution in the lateral dimensions x and y*, with one method for achieving additional resolution in the *vertical z dimension* already being discussed in the last section. In other papers in the ALC07 Conference, e.g. by Bauer, Koshikawa, Pavlovska, Quitmann and Schneider, the use of various techniques to add such lateral dimensions has been discussed in detail, and various aspects of such 'spectromicroscopy' methods are reviewed in detail elsewhere.[8,9] Thus, we will here only specifically consider one future direction involving focussing the radiation to a small spot so as to do what has been termed 'nano-ARPES'.[80]

In Fig. 25(a), the basic idea of the experiment is presented.[80] A zone-plate lens is used to focus a soft X-ray synchrotron radiation beam down to a spot of the order of 100 nm. A spectrometer like that shown in Fig. 1 is then used to measure spectra from various regions of the sample by raster-scanning the sample in front of the beam in *x* and *y*. Both core and valence level spectra can be

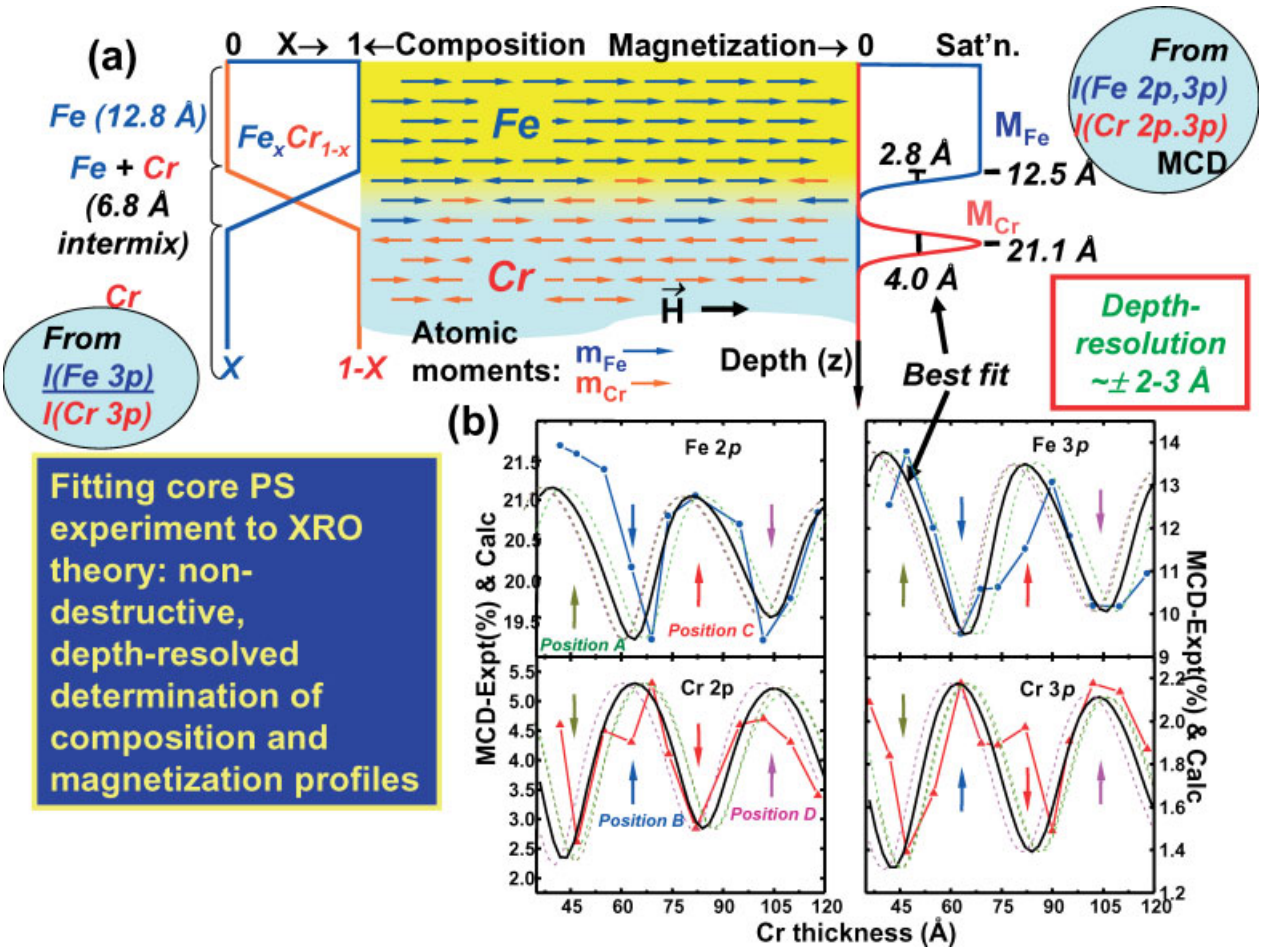

Figure 24. (a) The concentration and atom-specific magnetization profiles through the Fe/Cr interface, as derived by fitting X-ray optical calculations of photoemission[79] to the data of Figs 22 and 23. (b) The variation of Fe 2p and 3p MCD, and Cr 2p and 3p MCD, as about two cycles of the standing wave are scanned through the interface. From S.-H. Yang *et al.*, *J. Phys.: Condens. Matter* **2002**, *14*, L406. Reprinted with permission.

accumulated in this way. Figure 25(b) shows a micrograph from a cleaved sample of highly-oriented pyrolytic graphite (HOPG) in which the intensity in VB spectra has been used as a contrast mechanism. Looking in more detail at the ARPES spectrum from a specific 300 nm region reveals the band structure of the HOPG in that region. It is furthermore observed that the contrast comes about due to a slight tilting of different polycrystalline domains, with the brighter (yellow) regions corresponding to the so-called π-band of graphite being oriented toward the detector. Thus, one can look forward to taking advantage of much of what was discussed above with lateral spatial resolutions that should eventually reach 20 nm or better. In addition, spectromicroscopes making use of sophisticated electron optical elements promise to permit photoemission measurements below 10 nm, and perhaps at a few nm,[81,82] although probably not with the energy and angular resolution of the scheme in Fig. 25.

Time resolution in photoemission, e.g. in pump-probe experiments, that is by now down into the sub-nanosecond regime, and promises to go down into the femtosecond regime, is also considered in other presentations at the ALC07 Symposium and elsewhere.[9,11,83] In some cases, these measurements have even combined lateral resolution with time and spin resolution,[83] thus adding another key dimension for magnetic studies. Carrying out such spectromicroscopy measurements with standing-wave excitation, as demonstrated for the first time in a couple of first experiments[84,85] would add the final *z* dimension, thus permitting what might be considered a 'complete' photoemission experiment in the sense of all of the variables indicated in Fig. 1. These are clearly most promising areas for future development.

As another aspect of time-resolved photoemission, but one that often involves much longer timescales, we consider the *monitoring of surface chemical reactions in realtime*. As an early example of this type of measurement, Fig. 4(g) shows the time evolution of the different types of W atoms on a W(110) surface that has been exposed to an oxygen pressure of 3.0×10^{-9} torr at room temperature, with the spectra in Fig. 4(a)–(e) being snapshots along the way.[10] As noted earlier, the inherent narrowness of the W 4*f* levels, combined with high experimental resolution, permits resolving in these spectra six distinct types of W atoms: those at the clean surface, those in the 'bulk' = layers below the surface, two structurally inequivalent types bonded to one adsorbed oxygen atom, and those bonded to two or three oxygen atoms, with the different atomic geometries shown in Fig. 4(f). Being able to measure the time evolution of each of these features as shown in Fig. 4(g) has permitted analyzing the chemical kinetics of the process, which here takes place on the scale of minutes.[10]

Work in other laboratories has extended this type of reaction kinetics study to faster timescales and more complex chemical reactions,[86,87] as well as to higher effective ambient pressures,[13,86] thus permitting studies of such systems as aqueous solutions[88] and catalytic reactions[89] and representing yet another exciting area for future studies with photoemission.

As one technologically relevant example of these types of time-resolved reaction studies, Fig. 26(a) shows a high-resolution spectrum of an oxidized Si(001) surface, with clear resolution of at least five distinct chemical states from the element to that of SiO_2. Such spectra have been used in the same way as those in Fig. 4 to study the kinetics of oxidation of Si at pressures of about 10^{-6} torr, with resolution in time of all of the oxidation states.[90,91] As a more recent development, Fig. 26(b) shows a high-pressure XPS system in which the sample is separated from the exciting synchrotron radiation beam by a thin Al (or SiN) window and from the analysis section of the electron spectrometer by an electron lens with two stages of differential pumping.[13]

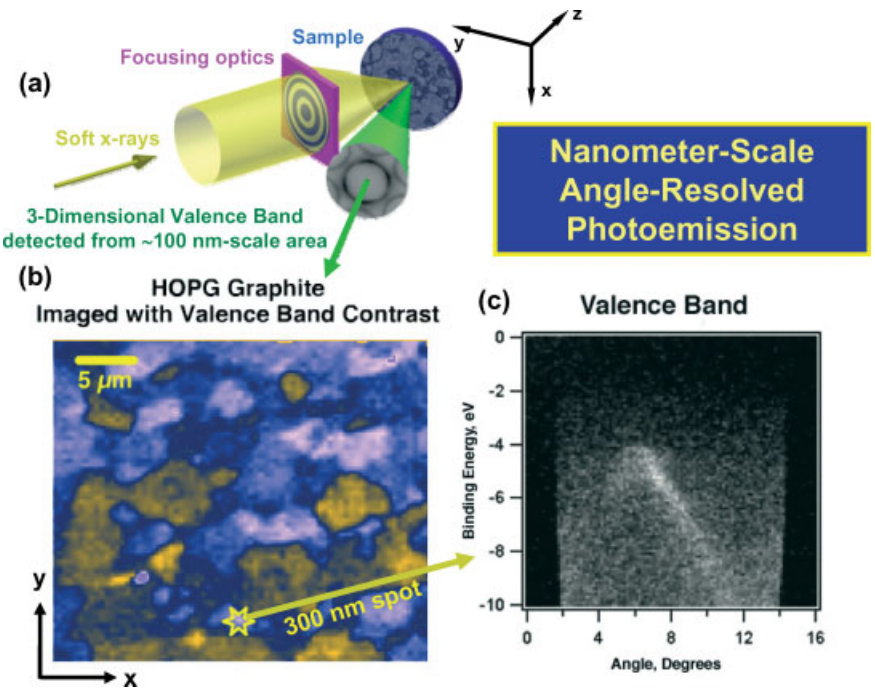

Figure 25. Some first experimental results for spatially-resolved angle-resolved photoemission. (a) The basic experimental geometry, with a zone-plate used to focus the radiation into a small spot. (b) An image obtained by scanning the sample in front of the spot in *x* and *y*, with contrast provided by the intensity of the valence-band spectra. (c) Angle-resolved photoemission results obtained from a 300 nm region indicated in (b). With permission from E. Rotenberg and A. Bostwick, private communication, **2005**.

This configuration permits having the sample region at up to 5–10 torr in pressure during measurements. In this way, surface reactions can be studied at pressures that in some cases are much closer to the actual conditions of industrial processes or systems of relevance to environmental science, thus bridging what has been called the 'pressure gap' between ultrahigh vacuum surface science research and real-world reaction conditions, and leading to the term 'ambient pressure XPS (APXPS).[88,92] As an example of the use of such a system, Fig. 26(c) shows several spectra from a very recent Si oxidation study at 450 C and 1 torr which is of direct relevance to the processing conditions used in the semiconductor industry.[92] Spectra here were recorded every 8 s, compared to every 15 s in Fig. 4, but they are shown here only about every minute. The SiO_2 thickness range covered is 0–25 Å. More detailed analysis of this data as shown in Fig. 27 indicates a clear division of the reaction rates into an initial rapid regime and a much slower quasi-saturated regime, with a break point between them that occurs when the SiO_2 is about 5–15 Å thick. Current models for the reaction kinetics of this process do not describe this regime of thicknesses that is now crucially important in devices.[92]

Looking ahead concerning ambient pressure XPS, we expect that much shorter timescales in the millesecond range and significantly better energy resolutions than those in Fig. 26(c) should be possible with brighter radiation sources, higher throughput spectrometers, and more efficient multichannel detectors that are under development.[93]

Concluding Remarks

The photoelectric effect has indeed come a long way since Einstein, and in its present form, photoelectron spectroscopy/photoemission represents an incredibly diverse range of measurements that can tell us which atoms are present and in what numbers, in what chemical and magnetic states the atoms exist, how the atoms are arranged in space with respect to one another, the detailed picture of how these atoms are bound to one another, and finally how all this varies in space and time, and with ambient gas pressure. It is also clear that present instrumentation developments, for example, of new spectrometers and detectors, as well as brighter photon sources providing also better time resolution, will lead to other exciting new directions and capabilities that even Einstein might not have dreamed of. Finally, but importantly, advances in many-electron theory that we have not discussed in detail here should allow us to interpret these multidimensional data sets in a much more quantitative way.

Acknowledgements

This work was supported by the Director, Office of Science, Office of Basic Energy Sciences, Materials Sciences and Engineering Division, of the US Department of Energy under Contract No. DE-AC02-05CH11231, by the Alexander von Humboldt Foundation and Helmholtz Association through a Helmholtz-Humboldt Award for the author, and by the Jűlich Research Center. The author is very grateful to Claus Schneider of the Jűlich Research Center and Wilfried Wurth of the University of Hamburg for acting as hosts

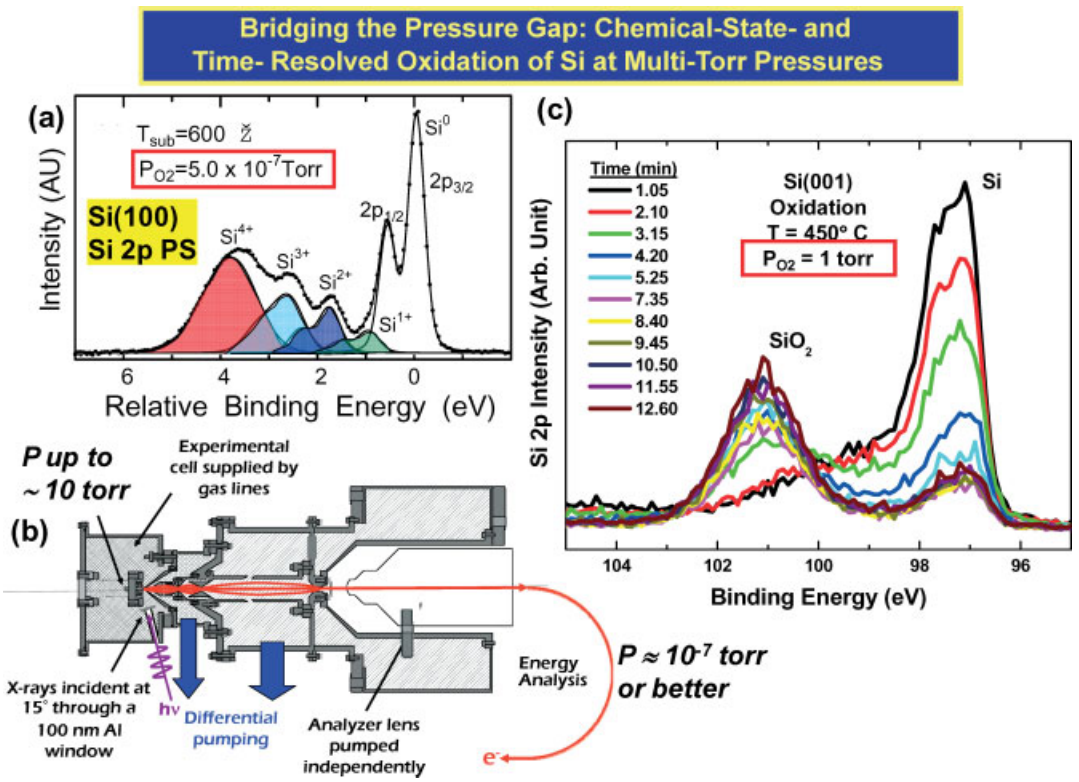

Figure 26. (a) High-resolution Si 2p spectrum from an Si(001) surface that has been oxidized at 600 °C and an ambient pressure of 5×10^{-7} torr. From Y. Enta *et al.*, *Phys. Rev. B* **1998**, *57*, 6294. Reprinted with permission. (b) A spectrometer configuration in which the sample region is isolated from the radiation source by a thin window and from the spectrometer by differential pumping so as to permit ambient pressures up to 5–10 torr. From D.F. Ogletree *et al.*, *Rev. Sci. Instrum.* **2002**, *73*, 3872. Reprinted with permission. c) A series of Si 2p spectra taken at about 1 min intervals during the oxidation of Si(001) at 450 °C and an ambient pressure of 1 torr. Based upon data in Ref. [91].

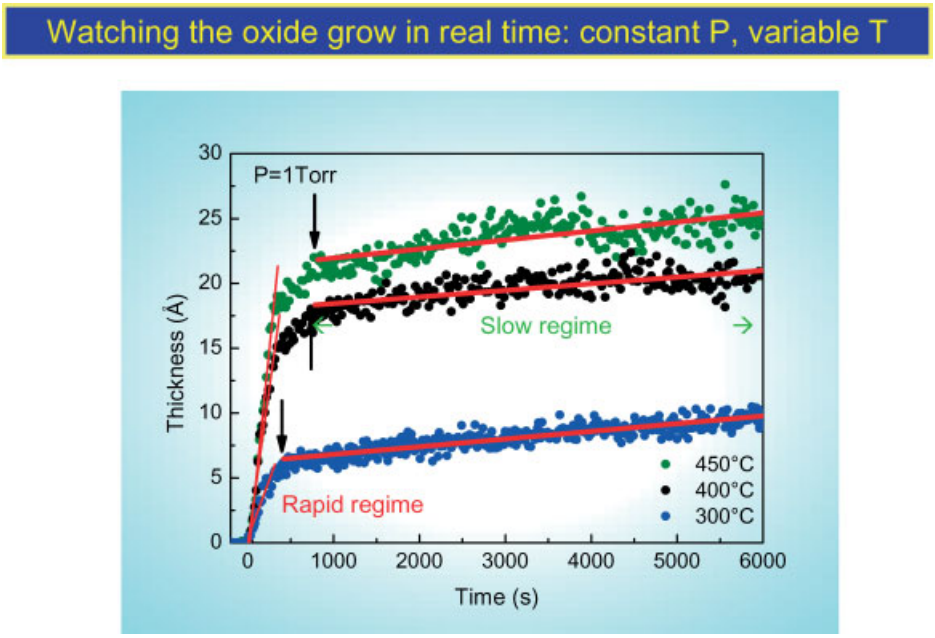

Figure 27. The time-dependent growth of the SiO_2 layer on Si(001) at 450 °C and various pressures, as derived from the relative intensities of the Si^{+4} and Si^0 peaks in spectra such as those in Fig. 26(c). From Y. Enta *et al*., *Appl. Phys. Lett*. **2008**, *92*, 012110. Reprinted with permission.

for this award. The author also thanks N. Mannella, L. Plucinski, J. Minar, Y. Takata, E. Rotenberg, Z. Yin, and W.E. Pickett for providing results prior to publication, and to S. Nunes for proofreading this manuscript.

References

[1] A. Einstein, *Ann. Phys.* **1905**, *17*, 132.
[2] Some of the first developments in x-ray photoelectron spectroscopy are presented in two books: K. Siegbahn, C. Nordling, A. Fahlman, K. Hamrin, J. Hedman, R. Nordberg, C. Johansson, T. Bergmark, S.-E. Karlsson, I. Lindgren, B. Lindberg, *Atomic, Molecular and Solid-state Structure Studied by Means of Electron Spectroscopy*, Nova Acta Regiae Soc. Sci. Ups. 201–282, Almqvist and Wiksells: Uppsala, **1967**.
[3] K. Siegbahn, C. Nordling, G. Johansson, J. Hedman, P.-F. Heden, K. Hamrin, U. Gelius, T. Bergmark, L. O. Werme, R. Manne, Y. Baer, *ESCA Applied to Free Molecules*, North-Holland: Amsterdam, The Netherlands, **1969**.
[4] C. S. Fadley, in *Electron Spectroscopy: Theory, Techniques, and Applications*, vol. II, Chap. 1 (Eds: C. R. Brundle, A. D. Baker), Academic Press: London, **1978**, available also as a reprint at: http://www.physics.ucdavis.edu/fadleygroup/.
[5] S. Hüfner, in *Photoelectron Spectroscopy: Principles and Applications* (3rd edn), Springer: Berlin, **2003**.
[6] C. S. Fadley, Surface structure studies using photoelectron diffraction and Auger electron diffraction, in *Synchrotron Radiation Research: Advances in Surface and Interface Science* (Ed: R. Z. Bachrach), Plenum Press: New York, **1992**.
[7] H.-J. Kim, E. Vescovo, S. Heinze, S. Blügel, *Surf. Sci.* **2001**, *478*, 193.
[8] E. Bauer, C. Koziol, G. Lilienkamp, T. Schmidt, *J. Electron Spectrosc. Relat. Phenom.* **1997**, *84*, 201.
[9] G. Schönhense, H. J. Elmers, S. A. Nepijko, C. M. Schneider, *Adv. Imaging Electron Phys.* **2006**, *142*, 160.
[10] R. X. Ynzunza, R. Denecke, F. J. Palomares, J. Morais, E. D. Tober, Z. Wang, F. J. Garcia de Abajo, J. Liesegang, Z. Hussain, M. A. Van Hove, C. S. Fadley, *Surf. Sci.* **2000**, *459*, 69.
[11] M. Pickel, A. B. Schmidt, M. Donath, M. Weinelt, *Surf. Sci.* **2006**, *600*, 4176.
[12] F. Banfi, C. Giannetti, G. Ferrini, G. Galimberti, S. Pagliara, D. Fausti, F. Parmigiani, *Phys. Rev. Lett.* **2005**, *94*, 037601.
[13] D. F. Ogletree, H. Bluhm, G. Lebedev, C. S. Fadley, Z. Hussain, M. Salmeron, *Rev. Sci. Instrum.* **2002**, *73*, 3872.
[14] C. J. Powell, A. Jablonski, I. S. Tilinin, S. Tanuma, D. R. Penn, *J. Electron Spectrosc. Relat. Phenom.* **1999**, *98*, 1.
[15] S. Tanuma, C. J. Powell, D. R. Penn, *Surf. Interface Anal.* **2005**, *37*, 1.
[16] Special journal issue dedicated to photoemission with hard x-rays, J. Zegenhagen, C. Kunz (Ed.), *Nucl. Instrum. Methods Phys. Res., Sect. A* **2005**, *547*, 1.
[17] *Program and Abstracts of the Second International Workshop on Hard X-ray Photoemission (HAXPES06)*, Spring8, Japan, available at: http://haxpes2006.spring8.or.jp/program.html [Last accessed in 2006].
[18] S. M. Goldberg, C. S. Fadley, S. Kono, *J. Electron Spectrosc. Relat. Phenom.* **1981**, *21*, 285.
[19] C. S. Fadley, S.-H. Yang, B. S. Mun, J. Garcia de Abajo, X-ray optics, standing waves, and interatomic effects in photoemission and x-ray emission, in *Solid-state Photoemission and Related Methods: Theory and Experiment* (Eds: W. Schattke, M. A. Van Hove), Wiley-VCH Verlag: Berlin GmbH, **2003**.
[20] J.-J. Yeh, I. Lindau, *At. Data Nucl. Data Tables* **1985**, *32*, 1, with these results also available in graphical form at: http://ulisse.elettra.trieste.it/services/elements/WebElements.html.
[21] P. H. Scofield, *Theoretical Photoionization Cross Sections from 1 to 1500 keV*, Lawrence Livermore Laboratory Report UCRL-51326, **1973**, out of print, but also available at: http://www.physics.ucdavis.edu/fadleygroup/Scofield.CrossSections.UCRL51326.pdf.
[22] M. B. Trzhaskovskaya, V. I. Nefedov, V. G. Yarzhemsky, *At. Data Nucl. Data Tables* **2001**, *77*, 97; M. B. Trzhaskovskaya, V. I. Nefedov, V. G. Yarzhemsky, *At. Data Nucl. Data Tables* **2002**, *82*, 257.
[23] *The NIST Electron Inelastic-Mean-Free-Path Database*, http://www.nist.gov/srd/nist71.htm; and the *NIST Electron Effective-Attenuation-Length Database*, http://www.nist.gov/srd/nist82.htm, [Last accessed in 2000].
[24] M. P. Seah, S. J. Spencer, *J. Electron Spectrosc. Relat. Phenom.* **2006**, *151*, 178.
[25] A. Jablonski, C. J. Powell, *Surf. Interface Anal.* **1993**, *20*, 771.
[26] C. S. Fadley, *Prog. Surf. Sci.* **1984**, *16*, 275; A. Herrera-Gomez (Ed.), *Proceedings of the 47th IUVSTA Workshop on Angle-resolved XPS*, Riviera Maya, Mexico, March, **2007**, to appear in Surface and Interface Analysis.
[27] S. Oswald, M. Zier, R. Reiche, K. Wetzig, *Surf. Interface Anal.* **2006**, *38*, 590.

[28] For example, the SESSA program by W. Smekal, W. S. M. Werner, C. J. Powell, *Surf. Interface Anal.* **2005**, *37*, 1059, includes all of the effects mentioned here except surface refraction due to V_0 and can be used over a very broad range of photon energies. Further information on this is available at: http://www.nist.gov/srd/nist100.htm and http://www.iap.tuwien.ac.at/~werner/sessa.html. An alternative program emphasizing the exact shape of spectra as produced by inelastic scattering is QUASES™ by S. Tougaard, with information on this available at: http://www.quases.com/.
[29] R. Hashimoto, A. Chikamatsu, H. Kumigashira, M. Oshima, N. Nakagawa, T. Ohnishi, M. Lippmaa, H. Wadati, A. Fujimori, K. Ono, M. Kawasaki, H. Koinuma, *J. Electron Spectrosc. Relat. Phenom.* **2005**, *144–147*, 479.
[30] A. W. Kay, F. J. Garcia de Abajo, S.-H. Yang, E. Arenholz, B. S. Mun, N. Mannella, Z. Hussain, M. A. Van Hove, C. S. Fadley, *Phys. Rev. B* **2001**, *63*, 115119, and earlier references therein.
[31] S.-H. Yang, B. S. Mun, N. Mannella, S.-K. Kim, J. B. Kortright, J. Underwood, F. Salmassi, E. Arenholz, A. Young, Z. Hussain, M. A. Van Hove, C. S. Fadley, *J. Phys.: Condens. Matter* **2002**, *14*, L406.
[32] C. S. Fadley, S. B. M. Hagstrom, M. P. Klein, D. A. Shirley, *J. Chem. Phys.* **1968**, *48*, 3779.
[33] NIST X-ray Photoelectron Spectroscopy Database, available at: http://srdata.nist.gov/xps/ [Last accessed in 2003].
[34] N. Mannella, A. Rosenhahn, C. H. Booth, S. Marchesini, B. S. Mun, S.-H. Yang, K. Ibrahim, Y. Tomioka, C. S. Fadley, *Phys. Rev. Lett.* **2004**, *92*, 166401.
[35] C. S. Fadley, D. A. Shirley, *Phys. Rev. A* **1970**, *2*, 1109.
[36] G. Van der Laan, C. Westra, C. Hass, G. A. Sawatzky, *Phys. Rev. B* **1981**, *23*, 4369.
[37] S. P. Kowalczyk, L. Ley, F. R. McFeely, R. A. Pollak, D. A. Shirley, *Phys. Rev. Lett.* **1973**, *7*, 4009.
[38] R. Denecke, J. Morais, R. X. Ynzunza, G. Fecher, J. G. Menchero, J. Liesegang, J. B. Kortright, Z. Hussain, C. S. Fadley, *Phys. Rev. B* **2002**, *65*, 245421.
[39] F. De Groot, A. Kotani, *Core Level Spectroscopy of Solids*, CRC Press, Boca Raton, FL, **2008**. Together with a user friendly program for calculating spectrum for some cases. http://.www.anorg.chem.uu.nl/people/staff/FrankdeGroot/multiplet1.htm.
[40] G. Van der Laan, S. S. Dhesi, E. Dudzik, J. Minar, H. Ebert, *J. Phys.: Condens. Matter* **2000**, *12*, L275.
[41] J. Menchero, *Phys. Rev. Lett.* **1996**, *76*, 3208; J. Menchero, *Phys. Rev. B* **1997**, *55*, 5505.
[42] L. Baumgarten, C. M. Schneider, H. Petersen, F. Schäfers, J. Kirschner, *Phys. Rev. Lett.* **1990**, *65*, 492.
[43] J. G. Menchero, *Phys. Rev. B* **1998**, *57*, 993.
[44] T. Greber, J. Wider, E. Wetli, J. Osterwalder, *Phys. Rev. Lett.* **1998**, *81*, 1654.
[45] The multiple scattering program *EDAC* due to J. Garcia de Abajo for calculating photoelectron diffraction is available at: http://csic.sw.ehu.es/jga/software/edac/index.html, with the methodology behind it described in F. J. Garcia de Abajo, M. A. Van Hove, C. S. Fadley, *Phys. Rev. B* **2001**, *63*, 075404.
[46] Another general program for photoelectron diffraction calculations *MSCD* due to Y. Chen, M. A. Van Hove, which includes geometry optimization routines, is available at: http://www.ap.cityu.edu.hk/personal-website/Van-Hove.htm [Last accessed in 1999].
[47] Y. J. Kim, C. Westphal, R. X. Ynzunza, Z. Wang, H. C. Galloway, M. Salmeron, M. A. Van Hove, C. S. Fadley, *Surf. Sci.* **1998**, *416*, 68.
[48] J. Osterwalder, A. Tamai, W. Auwarter, M. P. Allan, T. Greber, *Chimia* **2006**, *60*, A795, and earlier references therein.
[49] D. P. Woodruff, *Surf. Sci. Rep.* **2007**, *62*, 1.
[50] A. Szöke, in *Short Wavelength Coherent Radiation: Generation and Applications*, *AIP Conference Proceedings No. 147* (Eds: D. T. Attwood, J. Boker), AIP: New York, **1986**, p 361.
[51] C. S. Fadley, M. A. Van Hove, A. Kaduwela, S. Omori, L. Zhao, S. Marchesini, *J. Phys.: Condens. Matter* **2001**, *13*, 10517, and earlier references therein.
[52] S. Omori, Y. Nihei, E. Rotenberg, J. D. Denlinger, S. Marchesini, S. D. Kevan, B. P. Tonner, M. A. Van Hove, C. S. Fadley, *Phys. Rev. Lett.* **2002**, *88*, 5504.
[53] L. Plucinski, J. Minar, B. C. Sell, J. Braun, H. Ebert, C. M. Schneider, C. S. Fadley, *Phys. Rev. B* **2008**, *78*, 035108.
[54] T. J. Kreutz, T. Greber, P. Aebi, *J. Osterwalder. Phys. Rev. B 58*, **1998**, 1300.
[55] A. Damascelli, Z. Hussain, Z. X. Shen, *Rev. Mod. Phys.* **2003**, *75*, 473.
[56] N. Mannella, W. L. Yang, X. J. Zhou, H. Zheng, J. F. Mitchell, J. Zaanen, T. P. Devereaux, N. Nagaosa, Z. Hussain, Z. X. Shen, *Nature* **2005**, *438*, 474.
[57] E. W. Plummer, J. Shi, S.-J. Tang, E. Rotenberg, S. D. Kevan, *Prog. Surf. Sci.* **2003**, *74*, 251.
[58] E. Rotenberg, Y. Z. Wu, J. M. An, M. A. Van Hove, A. Canning, L. W. Wang, Z. Q. Qiu, *Phys. Rev. B* **2006**, *73*, 075426.
[59] Z. Hussain, C. S. Fadley, S. Kono, *Phys. Rev. B* **1980**, *22*, 3750; R. C. White, C. S. Fadley, M. Sagurton, Z. Hussain, *Phys. Rev. B* **1986**, *34*, 5226.
[60] K. Siegbahn, private communication, **2003**.
[61] A. Barrie, N. E. Christensen, *Phys. Rev. B* **1976**, *14*, 2442.
[62] Y. Takata, private communication, **2006**.
[63] Z. Yin, W. E. Pickett, private communication, **2006**.
[64] T. Hattori, H. Nohira, K. Azuma, K. W. Sakai, K. Nakajima, M. Suzuki, K. Kimura, Y. Sugita, E. Ikenaga, K. Kobayashi, Y. Takata, H. Kondo, S. Zaima, *Int. J. High Speed Electron. Syst.* **2006**, *16*, 353.
[65] C. S. Fadley, *Nucl. Instrum. Methods Phys. Res., Sect. A* **2005**, *547*, 24.
[66] L. Kover, M. Novak, S. Egri, I. Cserny, Z. Berenyi, J. Toth, D. Varga, W. Drube, F. Yubero, S. Tougaard, W. S. M. Werner, *Surf. Interface Anal.* **2006**, *38*, 569.
[67] N. Mannella, *Soft X-ray Spectroscopic and Structural Studies of Strongly Correlated Oxides*, PhD Thesis, University of California Davis, Davis, **2003**.
[68] N. Mannella, C. H. Booth, A. Rosenhahn, B. C. Sell, A. Nambu, S. Marchesini, B. S. Mun, S.-H. Yang, M. Watanabe, K. Ibrahim, E. Arenholz, A. Young, J. Guo, Y. Tomioka, C. S. Fadley, *Phys. Rev. B* **2008**, *77*, 125134.
[69] F. Offi, N. Mannella, T. Pardini, G. Panaccione, A. Fondacaro, P. Torelli, S. Huotari, M. W. West, J. W. Mitchell, C. S. Fadley, *Phys. Rev. B* **2008**, *77*, 174422.
[70] K. Horiba, M. Taguchi, A. Chainani, Y. Takata, E. Ikenaga, D. Miwa, Y. Nishino, K. Tamasaku, M. Awaji, A. Takeuchi, M. Yabashi, H. Namatame, M. Taniguchi, H. Kumigashira, M. Oshima, M. Lippmaa, M. Kawasaki, H. Koinuma, K. Kobayashi, T. Ishikawa, S. Shin, *Phys. Rev. Lett.* **2004**, *93*, 236401.
[71] H. Tanaka, Y. Takata, K. Horiba, M. Taguchi, A. Chainani, S. Shin, D. Miwa, K. Tamasaku, Y. Nishino, T. Ishikawa, E. Ikenaga, M. Awaji, A. Takeuchi, T. Kawai, K. Kobayashi, *Phys. Rev. B* **2006**, *73*, 094403.
[72] M. VanVeenendaal, *Phys. Rev. B* **2006**, *74*, 085118.
[73] Y. Takata, Y. Kayanuma, M. Yabashi, K. Tamasaku, Y. Nishino, D. Miwa, Y. Harada, K. Horiba, S. Shin, S. Tanaka, E. Ikenaga, K. Kobayashi, Y. Senba, H. Ohashi, T. Ishikawa, *Phys. Rev. B* **2007**, *75*, 233404.
[74] Y. Takata, Y. Kayanuma, S. Oshima, S. Tanaka, M. Yabashi, K. Tamasaku, Y. Nishino, M. Matsunami, R. Eguchi, A. Chainani, M. Oura, T. Takeuchi, Y. Senba, H. Ohashi, S. Shin, T. Ishikawa, *Phys. Rev. Lett.* **2008**, *101*, 137601.
[75] S.-H. Yang, B. S. Mun, N. Mannella, A. Nambu, B. C. Sell, S. B. Ritchey, F. Salmassi, S. S. P. Parkin, C. S. Fadley, *J. Phys.: Condens. Matter* **2006**, *18*, L259.
[76] J. Woicik, *Nucl. Instrum. Methods Phys. Res., Sect. A* **2005**, *547*, 227.
[77] S.-H. Yang, B. S. Mun, C. S. Fadley, *Synchrotron Radiat. News* **2004**, *24*, 17.
[78] S.-H. Yang, B. C. Sell, C. S. Fadley, *J. Appl. Phys.* **2008**, *103*, 07C519.
[79] S.-H. Yang, Specially written computer program for standing-wave photoemission from multilayer structures, (in press).
[80] E. Rotenberg, A. Bostwick, private communication, **2005**.
[81] T. Schmidt, U. Groh, R. Fink, E. Umbach, *Surf. Rev. Lett.* **2002**, *9*, 223.
[82] H. Marchetto, U. Groh, T. Schmidt, R. Fink, H. J. Freund, E. Umbach, *Chem. Phys.* **2006**, *178*.
[83] J.-P. Wustenberg, M. Cinchetti, M. Sanchez Albaneda, M. Bauer, M. Aeschlimann, *J. Magn. Magn. Mater.* **2007**, *316*, e411.
[84] J. Maul, J. Lin, A. Oelsner, D. Valdaitsev, N. Weber, M. Escher, M. Merkel, H. Seitz, U. Heinzmann, U. Kleineberg, G. Schonhense, *Surf. Sci.* **2007**, *601*, 4758.
[85] F. Kronast, A. Keiser, C. Wiemann, R. Ovsyannikov, D. Buergler, R. Schreiber, S.-H. Yang, H. Dürr, C. Schneider, W. Eberhardt, C. S. Fadley, *Appl. Phys. Lett.* (in press).
[86] A. Baraldi, G. Comelli, S. Lizzit, M. Kiskinova, G. Paolucci, *Surf. Sci. Rep.* **2003**, *49*, 169.
[87] R. Denecke, *Appl. Phys. A* **2005**, *80*, 977, and references therein.

[88] S. Ghosal, J. C. Hemminger, H. Bluhm, B. S. Mun, E. L. D. Hebenstreit, G. Ketteler, D. F. Ogletree, F. G. Requejo, M. Salmeron, *Science* **2005**, *307*, 5709.
[89] H. Bluhm, M. Hävecker, A. Knop-Gericke, E. Kleimenov, R. Schlögl, D. Teschner, V. I. Bukhtiyarov, D. F. Ogletree, M. B. Salmeron, *J. Phys. Chem. B* **2004**, *108*, 14340.
[90] Y. Enta, Y. Miyanishi, H. Irimachi, M. Niwano, M. Suemitsu, N. Miyamoto, E. Shigemasa, H. Kato, *Phys. Rev. B* **1998**, *57*, 6294.
[91] Y. Enta, Y. Miyanishi, H. Irimachi, M. Niwano, M. Suemitsu, N. Miyamoto, E. Shigemasa, H. Kato, *J. Vac. Sci. Technol., A* **1998**, *16*, 1716.
[92] Y. Enta, B. S. Mun, Y. Enta, M. Rossi, P. N. Ross, Z. Hussain, C. S. Fadley, K.-S. Lee, S.-K. Kim, *Appl. Phys. Lett.* **2008**, *92*, 012110.
[93] J.-M. Bussat, C. S. Fadley, B. A. Ludewigt, G. J. Meddeler, A. Nambu, M. Press, H. Spieler, B. Turko, M. West, G. J. Zizka, *IEEE Trans. Nucl. Sci.* **2004**, *51*, 2341.

Journal of Electron Spectroscopy and Related Phenomena 178–179 (2010) 2–32

Contents lists available at ScienceDirect

Journal of Electron Spectroscopy and Related Phenomena

journal homepage: www.elsevier.com/locate/elspec

X-ray photoelectron spectroscopy: Progress and perspectives

C.S. Fadley[a,b,*]

[a] Department of Physics, University of California, Davis, CA 95616, USA
[b] Materials Sciences Division, Lawrence Berkeley National Laboratory, Berkeley,CA 94720, USA

ARTICLE INFO

Article history:
Available online 4 February 2010

Keywords:
X-ray photoelectron spectroscopy
Photoemission
XPS
Photoelectron diffraction
Photoelectron holography
Angle-resolved photoemission
ARPES
Synchrotron radiation

ABSTRACT

In this overview, I will briefly explore some of the basic concepts and observable effects in X-ray photoelectron spectroscopy, including references to some key first publications, as well as other papers in this issue that explore many of them in more detail. I will then turn to some examples of several present and promising future applications of this diverse technique. Some of the future areas explored will be the use chemical shifts, multiplet splittings, and hard X-ray excitation in the study of strongly correlated materials; photoelectron diffraction and holography for atomic structure determinations; standing wave and hard X-ray excited photoemission for probing buried interfaces and more bulk-like properties of complex materials; valence-band mapping with soft and hard X-ray excitation; and time-resolved measurements with the sample at high ambient pressures in the multi-torr regime.

1. Introduction

X-ray photoelectron spectroscopy (XPS or ESCA) of course owes its quantification to Einstein's explanation of the photoelectric effect in 1905 [1], and the technique in fact has a long history that can be traced to contemporary measurements in which either X-rays or gamma rays were used to excite photoelectrons from solids [2]. In the period since the late 1950s, the photoelectric effect has been developed into one of our most powerful tools for studying the composition and electronic structure of matter, with Kai Siegbahn receiving the Nobel Prize in 1981 for the development of high-resolution XPS. His group's early pioneering work is documented in the two well-known ESCA books [3,4], with many other reviews and overviews appearing later [e.g. [5–8]. There has been much progress in the intervening decades, and new modes of measurement and more precise theoretical interpretation methodologies continue to be developed, with many of these being discussed in the other articles in this issue.

In this article, I will make brief reference to the history of various measurement modes and effects, but focus primarily on some of the most recent developments, pointing to more detailed discussions elsewhere as appropriate, and attempting in some cases to speculate on future interesting directions that have yet to be exploited. I will also focus on measurements of condensed matter phases (solids, surfaces, interfaces, and to some degree liquids [9]), the most interesting domain for basic and applied scientists using XPS. As a convenient operational definition of XPS, I will consider excitation energies above a few hundred eV and going into the hard X-ray regime up to 15 keV. Thus, both core levels and valence levels are readily observable in spectra. The topics considered will reflect to a certain degree my own personal biases, but, together with the other articles in this issue, I believe the reader will have access to a very thorough overview of the current status of XPS, as well as of some of the most exciting directions for its future.

2. Some basic considerations:

Fig. 1 illustrates in a schematic way some of the most important aspects of the XPS experiment, including some new directions of development. These will be discussed in subsequent paragraphs.

As an additional important starting point for quantification, the fundamental energy conservation equation in photoemission is the following [5–8]:

$$h\nu = E_{binding}^{Vacuum} + E'_{kinetic} + V_{charge} + V_{bias}$$
$$= E_{binding}^{Fermi} + \varphi_{spectrometer} + E_{kinetic} + V_{charge} + V_{bias} \quad (1)$$

in which h is Planck's constant; ν is the photon frequency; $E_{binding}^{Vacuum}$ is the binding energy of a given electron relative to the vacuum level of the sample; $E'_{kinetic}$ is the kinetic energy of the emitted electron just as it leaves the sample; $E_{kinetic}$ is the kinetic energy as measured finally in the spectrometer, which may be different from $E'_{kinetic}$ by a small contact potential difference if the sample is a solid; $E_{binding}^{Fermi}$ is the binding energy relative to the Fermi level or electron chemical

* Correspondence address: Department of Physics, University of California, Davis, CA 95616, USA. Tel.: +1 530 752 8788; fax: +1 530 752 4717.
E-mail address: fadley@physics.ucdavis.edu.

0368-2048/$ – see front matter © 2010 Elsevier B.V. All rights reserved.
doi:10.1016/j.elspec.2010.01.006

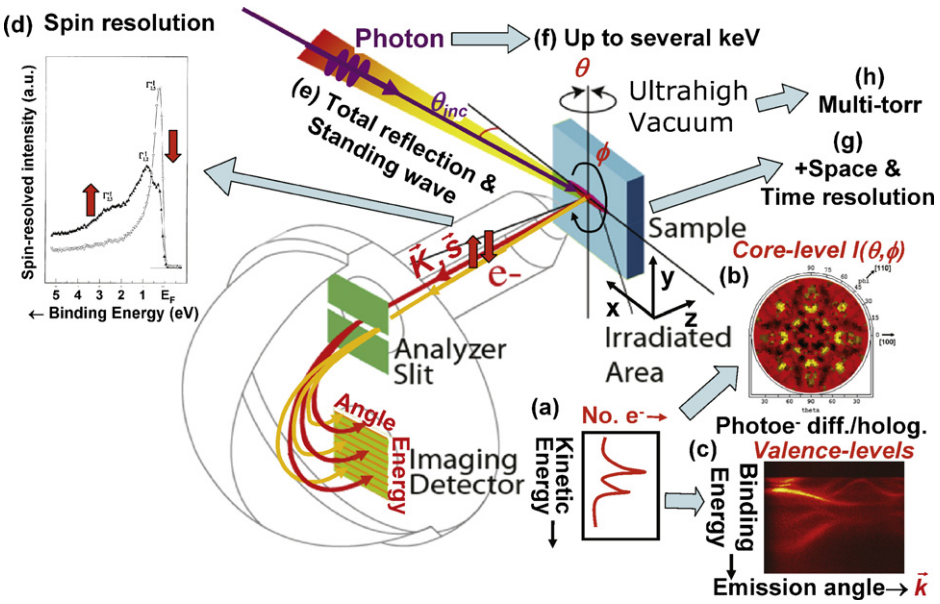

Fig. 1. Illustration of a typical experimental configuration for X-ray photoelectron spectroscopy experiments, together with the various types of measurements possible, including (a) simple spectra or energy distribution curves, (b) core-level photoelectron diffraction, (c) valence-band mapping or binding energy vs $\vec{k}$ plots, (d) spin-resolved spectra, (e) exciting with incident X-rays such that there is total reflection and/or a standing wave in the sample, (f) using much higher photon energies than have been typical in the past, (g) taking advantage of space and/or time resolution, and (h) surrounding the sample with high ambient sample pressures of several torr (with acknowledgement to Y. Takata for part of this figure).

potential; $\varphi_{spectrometer}$ is the work function of the spectrometer used to measure kinetic energy, V_{charge} is a possible charging potential on the sample that may build up if the emitted photoelectron and secondary electron current is not fully compensated by flow from the sample ground, and V_{bias} is a time-dependent bias potential that may be placed between the sample and the spectrometer, here with sign such that a positive bias acts to slow the photoelectrons. The effects of charging are discussed elsewhere in this issue by Cazaux. In very precise measurements, and/or as the excitation energy is increased into the multi-keV regime, both kinetic energies will be reduced by a recoil energy E_{recoil} imparted to the sample due to momentum conservation [4], with this often being negligible in typical XPS applications, but affecting both core and valence-band emission significantly as excitation energies are increased into the multi-keV regime [10]. E_{recoil} can be estimated from:

$$E_{recoil} \approx \frac{\hbar^2 k_f^2}{2M} \approx 5.5 \times 10^{-4} \left[\frac{E_{kin}(\text{eV})}{M(\text{amu})}\right],$$

where $\hbar$ has the usual meaning, k_f is the final photoelectron wave vector, and M is the effective mass of the atom(s) involved.

If one measures the electron kinetic energy, and perhaps also knows the spectrometer work function, it is thus possible to measure the binding energies of various inner (or core) electrons, as well as those of the outer (or valence) electrons that are involved in chemical bonding. Such measurements have been found to reveal a broad array of phenomena that can be used to characterize a given material, in particular the near-surface regions of solids from which most photoelectrons are emitted. Adding a bias potential, including one with time dependence V_{bias} (t), has also been found useful for determining the conductivity and dielectric properties of the sample, as discussed elsewhere in this issue by Süzer et al.

Many papers to date have explored the effects of charging in XPS and in fact a dedicated issue of this journal has recently been devoted to this [11]. Beyond this, a few papers have considered more quantitatively the space charge and image potential effects near surfaces on binding energies and peak widths [12–14], which emerge as a serious consideration as to the realm of applicability of future ultrahigh-brightness sources such as free-electron lasers in photoemission. These papers have demonstrated the general systematics of these effects [12,13], including detailed theoretical modelling [14]. As one example of the limitations uncovered in this work [14], it is concluded that, if the optimum case of metal core levels are to be studied with less than 50 meV resolution, the number of low-energy "cloud" electrons emitted per ultrashort excitation pulse (with the pulse assumed to be shorter than the time for the cloud electrons to significantly disperse and/or be neutralized) must be less than 10,000 e^-/mm spot diameter. Assuming that the low-energy cloud electrons are the dominant source of current, the number per pulse can be estimated simply by dividing the total sample current by the number of pulses per second. The criterion stated above thus implies that an increased number of photons per pulse and/or a highly focussed beam will exaggerate the energy broadening problem. Possible ways to get around this limitation so as to carry out XPS with these high-brightness sources are to increase the repetition rate of the pulses, from the ca. 5 Hz of the FLASH FEL source in Hamburg today [15] into the MHz regime, with the photons per pulse then decreasing by possibly ca. 10^{-5} for the same time-integrated number of photons. Defocussing the beam so as to spread the photons over a wider area would also help. By working with higher harmonics that have significantly lower photons per pulse, such effects can be reduced, while also having the advantage of moving up into the soft X-ray regime for a vuv-regime FEL. And of course, making use of a spectrometer that records a maximum energy and solid angle range for each pulse, as e.g. via time-of-flight would assist as the final stage of the measurement. Taking advantage of all of these possibilities will certainly leave some region of experimental space for high-resolution XPS with FEL excitation, and with exciting future possibilities. Sample damage due to the radiation is a consideration beyond space charge effects, however, with one solution to this being to raster the sample in front of the beam. But such damage will be very sample specific, and should be studied for each individual case, e.g. by somehow varying the effective number of photons per pulse over a large dynamic range.

It is also useful to specify the binding energy more precisely from the point of view of theoretical calculations, and we can write this as:

$$E_{binding}^{Vacuum}(Qn\ell j, K) = E_{final}(N-1,\ \ Qn\ell\, j\, hole, K) - E_{initial}(N), \qquad (2)$$

where we for simplicity consider a binding energy for the $n\ell j$ core level from atom Q, with n the principal quantum number, ℓ the orbital angular momentum quantum number, and $j = \ell \pm 1$ the additional quantum number if spin–orbit splitting is present, $E_{kinetic}\ (N)$ is the total initial state energy for the assumed N-electron system, and $E_{final}(N-1,\ \ Qn\ell j\, hole, K)$ is the Kth final-state energy for the $(N-1)$-electron system with a hole in the $Qn\ell j$ orbital. As an example, the six electrons in the Mn 2p subshell are split into Mn $2p_{1/2}$ (two electrons with $m_j = -1/2, +1/2$) and Mn $2p_{3/2}$ (four electrons with $m_j = -3/2, -1/2, +1/2, +3/2$). In general, there may be more than one final state associated with a given $Qn\ell j$ hole, with labels $K = 1, 2, \ldots$, as we discuss further below, e.g. in connection with multiplet splitting. Note also that, in the final state with the hole, all of the remaining electrons may relax slightly so as to try to screen the hole, thus lowering the total final energy by some amount that is often called the relaxation energy [5,6]. In many cases, this screening can also take the form of a change in orbital occupation numbers, with resulting configuration interaction in the final state. I return to discuss these effects briefly below. This relaxation/screening phenomenon has many consequences for the detailed interpretation of spectra. In many-electron theory, these effects are included in what is termed the "self-energy" correction, and accurate methods for calculating binding energy are discussed in the article by Olovsson et al. in this issue.

Beyond measuring photoelectron energies, the intensity of each peak or feature is of critical importance in most uses of XPS. A much-used approach for calculating and using photoelectron intensities from both core and valence levels is the so-called three-step model [5,6] which divides the process into three steps of: (1) penetration of the exciting photon beam into the surface, with some resulting intensity profile $I_{h\nu}(x, y, z)$ and the coordinates defined in Fig. 1, and excitation of photoelectrons from each atom in the sample that are located at various depths z, which will be proportional to the differential photoelectric cross-section of the particular level $Qn\ell j$ of atom Q involved (e.g. Mn $2p_{1/2}$ and Mn $2p_{3/2}$), written as $d\sigma_{Qn\ell j}(h\nu, \hat{\varepsilon})/d\Omega$ and dependent on photon energy, radiation polarization $\hat{\varepsilon}$, and the experimental geometry; (2) transport of the photoelectron from depth z to the surface, which involves inelastic attenuation via an inelastic mean free path Λ_e, as well as elastic scattering and diffraction; and (3) escape from the surface, which involves refraction and reflection at the surface barrier, with these effects being controlled by the inner potential V_0 having typical values of 5–15 eV, and possible surface inelastic scattering, as well as elastic scattering and diffraction (surface umklapp processes). In general, $d\sigma_{Qn\ell j}(h\nu, \hat{\varepsilon})/d\Omega$ is a maximum near threshold, when the photon energy is equal to $E_{binding}^{Vacuum}(Qn\ell j)$, and steadily decreases as the energy increases, although it may not reach a maximum until some distance above threshold, and it may also exhibit local minima called Cooper minima for energies not too far above threshold [5,16]. Neglecting elastic scattering and surface refraction in crossing the inner potential surface barrier V_0 for simplicity, one can finally calculate a core-level intensity from:

$$I(Qnlj) = C\int_0^\infty I_{h\nu}(x,y,z)\rho_Q(x,y,z)\frac{d\sigma_{Qn\ell j}(h\nu,\hat{\varepsilon})}{d\Omega}$$
$$\exp\left[-\frac{z}{\Lambda_e \sin\theta}\right]\Omega(h\nu,x,y)dxdydz, \qquad (3)$$

where C is a constant characteristic of the experimental geometry, $\rho_Q(x, y, z)$ is the density of atomic type Q at positions x, y, z, and $\Omega(h\nu, x, y)$ is the solid angle of acceptance of the spectrometer for a given photon energy (or equivalently electron kinetic energy) and positions x, y on the sample surface. In principle, $I_{h\nu}(x, y, z)$ can be calculated from a knowledge of the source beam spot profile, the incidence angle, and the X-ray indices of refraction of the substances in the sample [17]; $d\sigma_{Qn\ell j}(h\nu, \hat{\varepsilon})/d\Omega$ can be calculated from atomic theory, and its evaluation requires knowing the polarization of the exciting radiation [16,18–20], Λ_e can either be taken from tabulations of experimental and calculated data [21] or estimated from semi-empirical formulas, as e.g. the much-used TPP-2M formula [22,23]; and $\Omega(h\nu, x, y)$, which is equivalent once integrated over x and y to the spectrometer intensity response function or transmission, can be determined from reference-sample calibration measurements [24]. For excitation energies in the keV regime, if not even below this, non-dipole or retardation corrections are needed for a fully accurate description of $d\sigma_{Qn\ell j}(h\nu, \hat{\varepsilon})/d\Omega$, as first demonstrated by Krause [25], and discussed in much more detail elsewhere [26]. Ultimately, it is in principle possible to measure $I(Qnlj)$ and determine the only remaining unknown $\rho_Q(x, y, z)$, which amounts to a quantitative chemical analysis of the sample. These form the basic core of quantitative surface analysis by XPS, but with many prior papers and recent reviews pointing out significant additional considerations in achieving the most accurate results, as e.g. including the effects of elastic scattering and electron refraction [22,23,27–29]. These more accurate approaches are discussed elsewhere in this issue by Powell and Jablonski, and Werner. These methods also include attempts to create expert systems for analyzing XPS data that minimize the need for operator intervention and resulting subjectivity, as discussed by Castle in this issue.

It is also worth noting here that, if the X-ray incidence angle is such that a significant degree of reflection results, either by being near the critical angle for one of the interfaces in the sample or being near the Bragg angle for reflection from a set of crystal planes or a multilayer mirror, the form of $I_{h\nu}(x, y, z)$ can be significantly altered, as indicated in Fig. 1(e), and discussed further below. The interference of incident and reflected waves will create a standing wave above the surface and/or inside the sample. And if one goes well below the critical angle, the penetration depth of the radiation is also drastically reduced, resulting in what has been termed total reflection XPS (TRXPS) or grazing-incidence XPS (GIXPS), a technique for enhancing the signal from the surface region and reducing the inelastic background underneath spectra [30]: this is reviewed elsewhere in this issue by Kawai. The presence of X-ray reflectivity, even at the 1% level, will create a significant standing wave modulation of the exciting radiation, thus providing additional depth sensitivity that has been used to determine surface atomic positions [31]; resolve valence densities of states into their element-specific components [32], as discussed by Zegenhagen in this issue; or determine depth profiles in nanometer-scale layered structures [33], as discussed in more detail later in this article.

Turning again to Fig. 1, we can describe the XPS measurement as starting when a photon with variable polarization is incident on the sample surface at some angle θ_{inc}. Photons in the XPS regime can be generated from either laboratory sources (X-ray tubes or higher harmonic generating laser sources), or synchrotron radiation. The photon is absorbed, exciting a photoelectron into the vacuum with some momentum $\vec{p} = \hbar\vec{k}$, where $\vec{k}$ is the electron wave vector, and $\vec{s}$ is the electron spin, and finally into some kind of spectrometer for measuring kinetic energy. The energy of the photoelectron inside the surface is greater by the inner potential V_0, such that the wave vector $\vec{k}$ outside is somewhat smaller in magnitude, and perhaps of slightly different direction due to refraction, if compared to the wave vector $\vec{k}$ inside the surface.

In Fig. 1, I show the most commonly used spectrometer configuration, which consists of a set of concentric hemispherical deflection electrodes and adjustable slits to regulate both source

size and angular acceptance [34], although several other geometries are possible, including time-of-flight measurements if the exciting source is pulsed. In this hemispherical geometry, electrons of a given energy are focussed to a given radius (i.e. along a given y coordinate in the detection plane of Fig. 1), such that integrating intensity over a given radius yields the first type of measurement: a photoelectron spectrum of number of electrons vs kinetic energy or energy distribution curve (EDC), as shown schematically in Fig. 1(a). Alternate modes of operating the retarding lens in such a spectrometer permit resolving one of the electron emission angles along a two-dimensional detector, as shown in Fig. 1(b) [34]; this is the most common current method of recording angle-resolved photoemission (ARPES) from valence electronic states, a type of measurement that is now being extended into the soft and hard X-ray regime, as discussed below. The commercial instrument from Scienta based on this principal [34] has been used for most ARPES measurements to date, but other options are now on the market. Alternatively, by suitably choosing the voltages on the retarding lens, this second axis in the detector can be used to determine the y-axis position of origin of the electrons, providing a one-dimensional type of photoelectron microscopy that is also well established in commercial systems.

Other spectrometer configurations, including those with electron optical elements permitting direct two-dimensional angular resolution or two-dimensional photoelectron microscopy also exist [34–37]. These are available both as commercial products with resolutions down to a micron (1000 nm), and synchrotron radiation based instruments that can achieve about 20 nm resolution, but with the promise of 5–10 nm, if not less, in the near future. The additional information that such microscopes provide, particularly with synchrotron radiation as the excitation source, will certainly lead to enhanced applications of them in the future, and I will later show some results obtained with one such instrument. In other articles in this issue, Escher, Artyushkova, and Margaritondo review the current status of photoelectron microscopy with both laboratory sources and synchrotron radiation excitation. It has also been demonstrated that photoelectron microscopy can be carried out with hard X-ray excitation [38,39] and this will certainly be a future area of exploitation. I will also discuss later the possibility of adding the third vertical dimension to such microscope images by using standing wave excitation.

As a final basic consideration related to measuring peak intensities, the degree of non-linearity in the final detector system needs to be taken into account. Straightforward methods for measuring and correcting for non-linearity have been discussed [40,41], but it seems like these are not widely practiced or appreciated. In measurements made over a large dynamic range, as e.g. in tuning photon energy on and off a resonance absorption process, such non-linearities can alter the observed intensities appreciably [42], but even in more routine analytical XPS applications where peaks can still range in intensity over 1–2 orders of magnitude, these effects need to be corrected for. Probably the most linear detectors operating to rates of several MHz are individual channeltrons, but the more efficient multiplexing systems provided by microchannel plates backed by phosphor/CCD combinations, resistive anodes or cross-wires to achieve spatial information begin to saturate at ~1 MHz. Looking to the future, detectors going well beyond this and into the GHz regime are clearly needed to be able to handle even the electron fluxes of certain current sources (either laboratory XPS or high-brightness synchrotron radiation sources), not to mention the much brighter free-electron laser sources now beginning to be used. Although some development steps have been made in this direction, with a one-dimensional prototype detector actually having demonstrated performance into the GHz range [43], much more is needed. This is currently a significant bottleneck to the future development of XPS.

3. Electron inelastic scattering and surface vs bulk sensitivity

Of key importance in any photoemission experiment is the depth of sensitivity in a solid sample, which is controlled primarily by the photoelectron inelastic mean free path (IMFP) Λ_e, but also with significant modifications due to elastic electron scattering and surface escape to yield an effective attenuation length [22], as discussed by Powell and Jablonski in this issue. If inelastic scattering is assumed to be isotropic in the material, and these other effects are neglected, the intensity from a certain emission depth z will decay as $I(z) = I_0 \exp[-z/\Lambda_e \sin\theta]$, where θ is the takeoff angle with respect to the surface and the mean escape depth below a surface will be given simply by $\Lambda_e \sin\theta$. Although this is an oversimplification of the physics, as discussed by Powell and Jablonski, and Werner elsewhere in this issue, there is in general a monotonic decrease in emission depth with decreasing takeoff angle that can be used both qualitatively and quantitatively to study the depth distributions of species near surfaces. This variation of mean depth has resulted in angle-resolved XPS (ARXPS) by now being a widely used method in surface and interface science method for selectively varying depth sensitivity and deriving concentration profiles of different species [28]. Various methods of analyzing ARXPS data now exist, ranging from the qualitative to the quantitative, with each having what are often conflicting advantages of simplicity vs accuracy [28]. These are reviewed in detail elsewhere in this issue by Powell and Jablonski, Werner, and Brundle.

As a useful summary of the variation of IMFP with kinetic energy, Fig. 2 shows a recent compilation of values calculated using the TPP-2M formula for 41 elemental solids [23]. The well-known form of these curves, with a minimum between roughly 20 and 100 eV, a general increase on going above this to higher energies, and a less pronounced increase on going to energies below the minimum, is a critical ingredient in the analysis of XPS data. The IMFP increases above 1 keV roughly as $E_{kin}^{0.75-1.10}$ over a variety of elements and compounds, but with the majority of elements in Fig. 2 suggesting

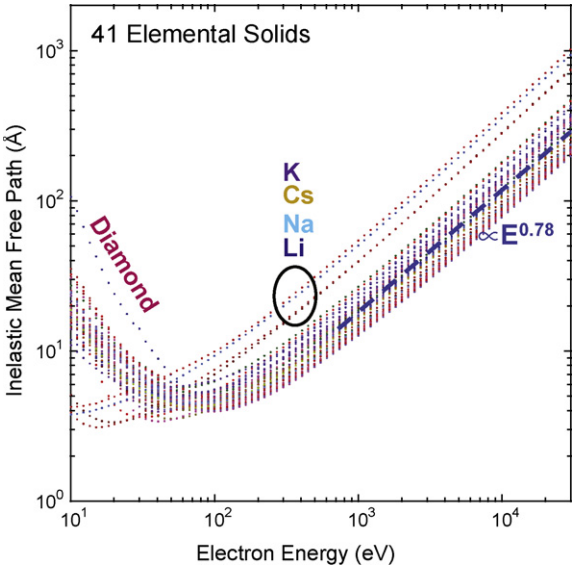

Fig. 2. Inelastic mean free paths (IMFPs) for 41 elements, calculated using the TPP-2M formula: Li, Be, three forms of carbon (graphite, diamond, glassy C), Na, Mg, Al, Si, K, Sc, Ti, V, Cr, Fe, Co, Ni, Cu, Ge, Y, Nb, Mo, Ru, Rh, Pd, Ag, In, Sn, Cs, Gd, Tb, Dy, Hf, Ta, W, Re, Os, Ir, Pt, Au, and Bi. Five "outlier" elements are indicated to provide some idea of what electronic structure characteristics can give rise to deviations from the majority behavior: diamond and the alkali metals. The dashed straight line for higher energies represents a variation as $\Lambda_e \propto E_{kin}^{0.78}$, and is a reasonable first approximation to the variation for all of the elements shown (from Ref. [23]).

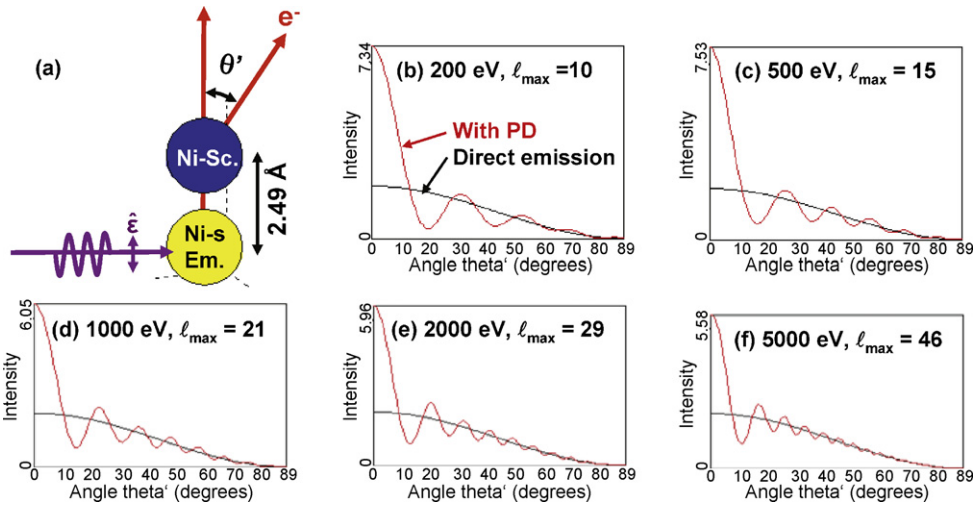

Fig. 3. Single scattering calculations of Ni dimer photoelectron diffractions patterns for s-level emission into a p outgoing wave at various photon energies. (a) The model geometry, with polarization along the Ni–Ni bond direction, and only one Ni atom considered as emitter. (b)–(f) Diffraction patterns for energies from 200 to 5000 eV are shown in red, with the direct emission in the absence of scattering also shown in black. In each panel, the number of partial wave phase shifts needed to assure full convergence is indicated, with this leading to one limitation of using the cluster approach at energies beyond about 5000 eV (calculations using the EDAC program of Ref. [44]). (For interpretation of the references to color in this figure caption, the reader is referred to the web version of the article.)

$E_{kin}^{0.78}$ as a convenient estimation formula. It is also noteworthy that the only element here which shows an unusually large increase in its IMFP at energies down to 10 eV is diamond, with a very large bandgap of 5.5 eV. Four other outliers over the full energy range are the alkali metals. These results thus strongly suggest that the only way to significantly enhance the bulk sensitivity of photoemission beyond what is achieved routinely in XPS at ca. 1 keV is to go into the multi-keV regime, with the only type of material expected to show a strong increase in IMFP at very low energies being an insulator with fairly large bandgap. This provides a major impetus for the new developments in hard X-ray photoemission, as discussed by Köver later in this article.

Inelastic scattering at the surface is also an important consideration in XPS, as discussed elsewhere in this issue by Nagatomi and Goto. This is expected to decrease in importance as the kinetic energy increases, as discussed also in the later article by Köver.

Note also that the form of the inelastic tail and background in an XPS spectrum can provide an immediate qualitative, and with further analysis even quantitative, idea of the depth distribution of the emitting species. Qualitatively, a peak with a very high intensity in its inelastic tail must have its origin in an atom well below the surface, whereas a peak with a very low inelastic tail must have its origin in an atom near to or on the surface. Analyzing such effects quantitatively was pioneered by Tougaard [29(b)], who discusses it elsewhere in this issue.

Finally, it is also worthwhile in this section to discuss some significant advantages that accrue to using hard X-rays in the multi-keV regime for excitation in ARXPS, a topic that is also explored in depth here by Köver. To first illustrate the effects of elastic scattering on ARXPS, Fig. 3 shows a set of calculations at different photoelectron energies from 200 to 5000 eV obtained with the photoelectron diffraction program EDAC [44]. The atomic cluster (Fig. 3(a)) is a simple diatomic of two Ni atoms separated by the Ni nearest-neighbor distance. The polarization is oriented along the Ni–Ni bond, and electrons emitted from an s-level ($\ell = 0$) in one of the atoms are detected by moving the spectrometer relative to the bond direction. The black curves represent the unscattered intensity in the absence of the Ni scatterer; they clearly show the influence of the s-level differential cross-section, which goes as $\cos\theta'$, with θ' being the scattering angle. With scattering and interference of direct and scattered waves, the red photoelectron diffraction patterns result. They show the well-known forward scattering peaks along the bond direction, and higher-order interference fringes that we will later see can be related to a holographic interpretation of such data [45]. In the simplest single-scattering picture, the maxima of these holographic fringes should appear when the following equation is satisfied:

$$2\pi m = \left[\frac{2\pi}{\lambda_e}\right] d_{sc}(1 - \cos\theta') + \varphi_{sc}, \quad m = 1, 2, \ldots \tag{4}$$

where λ_e is the electron de Broglie wavelength, d_{sc} is the distance between emitter and a given scatterer, and φ_{sc} is the phase shift associated with the scattering process, often small compared to the first term in Eq. (4). It is important for the present discussion that these forward scattering peaks become much narrower, and the higher-order fringes decrease in magnitude, as energy increases. This is a result of the narrowing of the forward peak in the differential elastic scattering cross-section, and the decrease in importance of larger scattering angles. Thus, large-angle scattering effectively becomes negligible for angles greater than approximately by 15–20° at 5000 eV, and this trend is expected to continue for higher energies.

Another aspect of high-energy photoelectron escape from a solid that has recently been emphasized is that extrinsic loss processes such as plasmons do not lead to a significant change in the direction of electron motion [39]. Thus, the effects of both elastic and inelastic scattering on ARXPS are expected to diminish as energy increases, leaving the straight-line trajectory as a better approximation.

The implications of the above discussions for ARXPS are illustrated in Fig. 4. At typical XPS energies of 500–1500 eV (Fig. 4(a)), one must allow for elastic scattering in estimating the effective emission depth, as mentioned above. For very low angles, refraction of the electrons as they surmount the inner potential can act to further reduce the degree of surface sensitivity in measured spectra. Finally, surface inelastic scattering processes can further complicate analyses. As Fig. 4(b) indicates, all three of these effects tend to be markedly reduced as energies mount into the hard X-ray regime. Forward elastic scattering which does not change propagation direction significantly becomes dominant (cf. Fig. 3). The inner potential is much smaller than the photoelectron energy, such that refraction is negligible until very low angles of exit. Thus, obtaining more directly interpretable data down to takeoff angles of 5–10° should be possible in hard X-ray ARXPS; by contrast, at typical

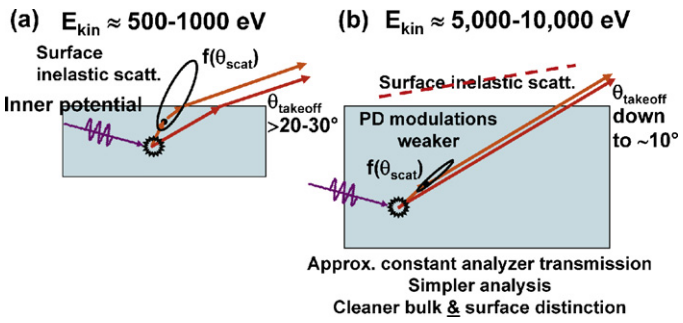

Fig. 4. Illustration of basic effects encountered in quantitatively interpreting angle-resolved XPS (ARXPS) data at (a) typical laboratory XPS energies and (b) hard X-ray energies into the 5–10 keV range. Several simplifications are possible with hard X-rays: less influence of high angle-to-low angle elastic scattering, reduced or negligible surface inelastic scattering, less effect of refraction in crossing the surface barrier, and a more constant spectrometer transmission function if the range of energies considered is not too large compared to the mean energy.

XPS energies, the usual recommendation is to limit this angle to no less than 20–30° [27,28]. Surface inelastic scattering is also much reduced. Thus, ARXPS or more precisely ARHXPS with hard X-rays, promises to be easier to analyze quantitatively, while having the advantage of allowing a broader angular range of data acquisition that will still allow significant surface enhancement at the lowest angles. We later show some recent experimental results of this kind.

4. Core-level spectra

From XPS energy distribution curves or spectra, a number of useful effects have been extracted, and, although these are well known to most XPS users, I discuss them here briefly for completeness and to establish vocabulary for subsequent sections:

- *Core-level chemical shifts* certainly represent one of the most often-used aspects of XPS. From the first clear confirmation of core-level chemical shifts, for the case of sodium thiosulfate-$Na_2S_2O_3$ [46], a very convenient compound that has S in two distinct chemical states that are resolved in the spectrum (actually serendipitously chosen for this experiment [47]), such chemical shifts have by now been measured for thousands of systems, providing unique information on the distributions of chemical and structural sites near surfaces. Such shifts can now be measured with resolutions in the 50 meV range using synchrotron radiation, yielding extremely sensitive decompositions of spectra into the chemical and structural components of a sample. The detailed theoretical prediction and interpretation of such shifts must always allow for the variety of final-state effects implicit in the discussion of Eq. (2) above. In other articles in this issue, the measurement and theoretical interpretation of such shifts for a variety of systems are discussed: the calculation of such shifts from local-density theory by Takahata and Dos Santos Marques, and by Olovsson et al.; the use of such shifts and the peak broadenings they produce to investigate metal alloys by Cole and Weightman; the combination of core-level photoelectron and Auger electron shifts into the Auger parameter by Moretti; and the use of chemical shifts in the study of nanostructures by Baer, self-assembled monolayers by Zharnikov, polymers and composites, adhesion by Watts, and semiconductor multilayer structures by Brundle.
- *Core-level multiplet splittings*: Another core-level effect is multiplet splittings in core-level emission from systems with unfilled valence shells [48,49]. The core subshell from which emission occurs can couple its spin and orbital angular momenta in different ways to the net spin and orbital angular momenta of the unfilled valence shells, resulting in more than one final state K in the language of Eq. (2) and thus more than one binding energy. The first measurements of this type were by Siegbahn et al. for the O_2, NO, and N_2 molecules [48], with the O 1s and N 1s binding energies for the paramagnetic molecules O_2 and N_2 being split into two components due to the spin-dependent exchange interaction of the 1s electron remaining after photoemission with the net valence electron spin. Soon afterwards, such splittings were measured for the transition metal atom Mn in several compounds [49], with the Mn 3s spectra in particular exhibiting doublets whose splittings are roughly proportional to the net 3d spin on Mn. These splittings and other final-state effects are now routinely used to probe the nature of the valence states and chemical bonding in magnetic and other complex materials, and they can be quantitatively analyzed using Anderson impurity model theory, with convenient computer programs for analyzing such data now available [50]. Some of these effects are illustrated in a case study below.
- *Core-level satellites and final-state configuration interaction*: Beyond the well-known shake-up and shake-off intensity first explored in noble gases and observed frequently in molecular systems, the first dramatic truly many-electron effect seen in XPS was final-state configuration mixing involving ligand-to-metal charge transfer [51]. By now, such measurements constitute a key tool in the study of transition metal, rare earth, and actinide compounds, with special importance for magnetic and strongly correlated systems. The interpretation of such data, which naturally include multiplet effects, is reviewed elsewhere, along with many experimental examples [50]. There is no doubt that the measurement and interpretation of such effects will be a major aspect of XPS in the future, including what one hopes will be even more accurate theoretical modelling involving also metallic systems. Closely related to these satellites are the so-called intrinsic loss processes that can create both electron–hole pair and plasmon excitations, and which can exhibit quantum mechanical interference with the normal extrinsic loss processes during electron transport. Theory and experiment concerning these effects are discussed elsewhere in this issue by Fujikawa and Köver.
- *Core-level vibrational fine structure*: It has long been realized that vibrational broadening can play a role in XPS spectra [52], but by now such effects have been resolved in adsorbates [53] and in many gas-phase molecular systems [54]. It is thus clear that such effects, and their temperature dependence, will play a role in the future quantitative analysis of XPS spectra.
- *Photoelectron diffraction and holography*: If the photoelectron emission direction is varied relative to the crystal axes of a single-crystal, epitaxial, or textured sample, for example by rotating the sample about the θ and ϕ axes in Fig. 1, additional effects are seen, due to the anisotropic elastic scattering and interference of the outgoing electron wave components from various atoms in the sample. If the emission is from a core level that is necessarily highly localized on one atomic site, a photoelectron diffraction pattern is observed [45]. The first X-ray photoelectron diffraction (XPD) patterns were measured for a NaCl crystal [55] and for a Au single crystal [56]. A more recent example of this for O 1s emission from NiO(0 0 1) is shown in Fig. 1(b). Such scanned-angle patterns can be used to determine near-surface atomic structures, and XPD has become one of the standard methods for determining surface structures [45], as we will consider in more detail below. Woodruff in this issue discusses the complementary synchrotron radiation based method of using scanned-energy photoelectron diffraction to determine adsorbate structures on surfaces. Photoelectron holography, in which a set of scanned-angle or scanned-energy photoelectron diffraction patterns are treated as a volume hologram in three-dimensional $\vec{K}$ space, has also been demonstrated in a number of experimental studies and

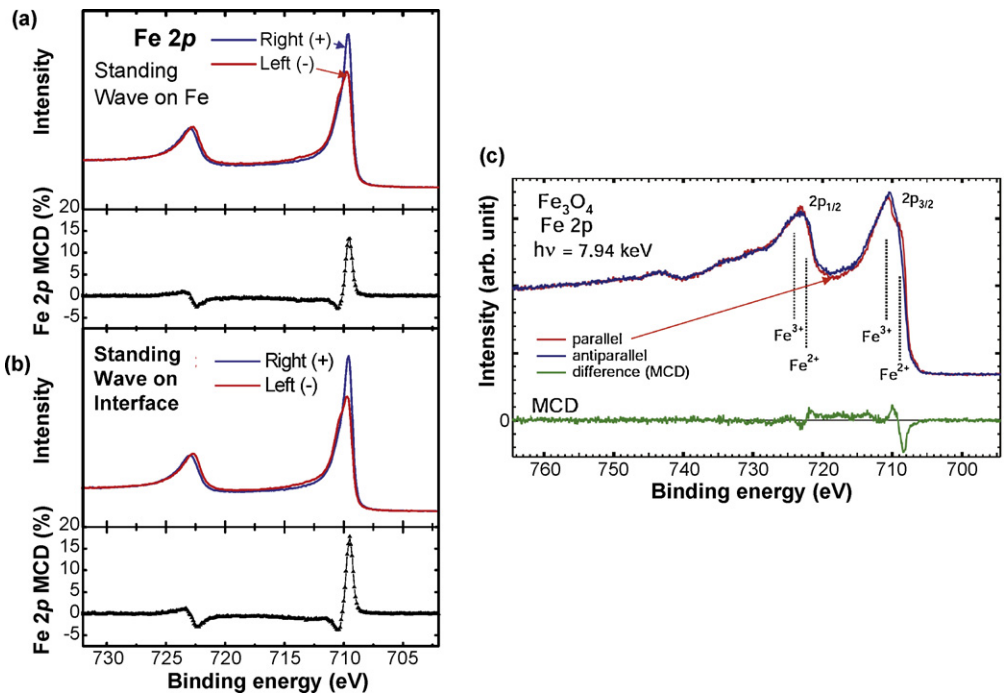

Fig. 5. Magnetic circular dichroism in Fe 2p emission. (a) and (b) MCD data for Fe emission from a 16 Å overlayer of Fe on a Cr wedge, excited by a soft X-ray standing wave at 825 eV that has been positioned either (a) maximally on Fe or (b) maximally on Cr near the Fe/Cr interface (from Ref. [33]). (c) MCD for Fe emission from hematite at 7.94 keV, demonstrating for the first time that these effects can be measured with hard X-rays (from Ref. [61]).

is reviewed elsewhere [57]. Matsushita et al. in this issue also discuss a newly developed method for holographic reconstruction. I will return later to consider both photoelectron diffraction and photoelectron holography (PD and PH) for a couple of illustrative examples, including the implications of taking the photoelectron kinetic energy into the multi-keV regime, with a preliminary theoretical look at what is expected in this already in Fig. 3.

- *Circular and linear dichroism*: Dichroism, in which a photoelectron intensity changes if the polarization of the incident radiation is changed, is ubiquitous in XPS due to the differential cross-sections that control the emission intensity. But beyond this are two significant effects that deserve attention here. First is something that is often referred to as circular dichroism in angular distributions (CDAD) [58]. This represents a combination of the preferential excitation of certain states of angular momentum (certain combinations of total angular momentum ℓ and z-component m_ℓ) by circularly polarized (CP) radiation, combined with forward-peaked elastic photoelectron scattering from nearby atoms. It results in what are often referred to as "peak rotations" in the PD patterns in the plane of the rotating electric field vector [58b]. It has also been pointed out that the two XPD patterns resulting from right and left CP (RCP and LCP) radiation can be considered in first approximation as a stereoscopic view of the atoms surrounding a given emitter [59], and Matsui et al. discuss this method later in this issue.

  If a given core level furthermore exhibits resolvable spin–orbit splitting, and the system also has long-range magnetic order relative to the radiation source and spectrometer coordinate system, magnetic circular dichroism (MCD) results. Here, the intensity of a photoelectron peak is found to change when the polarization of the incoming radiation is changed from right circular (RCP) to left circular (LCP). MCD is thus defined as the difference of two intensities or I(RCP) − I(LCP), usually divided by the sum or the average of these two intensities to yield a fractional number. These effects were first observed and qualitatively interpreted in core-level photoemission from Fe by Baumgarten et al. [60]. As more recent examples, Fig. 5(a) and (b) shows results obtained for Fe 2p emission from an Fe overlayer on a substrate of Cr, excited by a soft X-ray standing wave (SW) at 825 eV whose maximum has been located at two positions relative to the Fe/Cr interface [33]. Fig. 5(c) shows very recent results for Fe 2p emission from Fe_3O_4 at the much higher photon energy of 7.94 keV, a first demonstration that such effects persist in hard X-ray photoemission [61]. A simple one-electron explanation of these results [62] proceeds by noting that the spin–orbit interaction splits the six 2p states into two $2p_{1/2}$ and four $2p_{3/2}$ states. Beyond this, one assumes a Zeeman-like splitting of the sublevels within each spin–orbit peak induced by an effective internal magnetic field of the ferromagnet and resulting from the exchange interaction. These energy splittings are then combined with the different intensities expected for these $2p_{1/2}$ and $2p_{3/2}$ levels through the appropriate atomic transition probabilities. The expectation from this simple model is an up-down character for the MCD profile across a given peak, as well as an opposite sign of the MCD for the $2p_{3/2}$ and $2p_{1/2}$ peaks, as seen in Fig. 5. This general form of 2p MCD spectra has by now been observed in many 3d transition metal systems, and it clearly also exists up to much higher excitation energies [61]. Combining SW excitation with MCD will be discussed in more detail below. Because ferromagnetic order is necessary for MCD to be observed, measurements of this type provide an element-specific measurement of magnetic order, and this technique has been used to study a variety of magnetic systems.
- *Resonant photoemission*: A final important effect related to photoelectron intensities is resonant photoemission (RPE), in which the photon energy is tuned so as to lie on a strong core-level absorption resonance (e.g. Mn $2p_{3/2}$ or L_3), with this providing a second interfering channel for photoelectron excitation in another level in the same atom (e.g. Mn 3d) [63]. The intensity of the second level can thus be dramatically increased or decreased, depending on the relative amplitudes and phases of the interfering channels. This effect can be very useful in enhancing the contributions of a given type of valence character to bonding (e.g. by enhancing

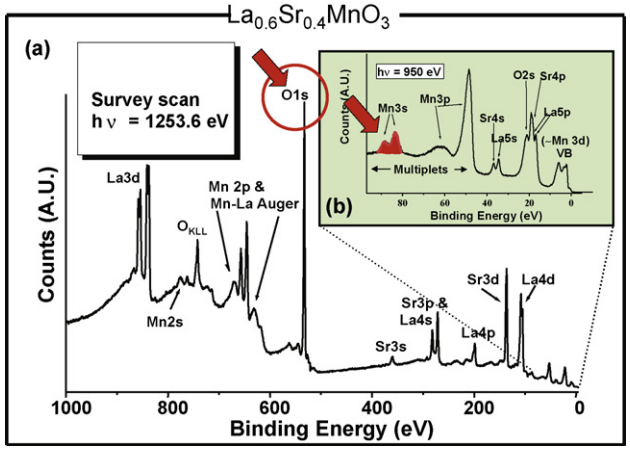

Fig. 6. (a) A broad survey spectrum from the colossal magnetoresistive oxide $La_{0.6}Sr_{0.4}MnO_3$ obtained with excitation at 1253.6 eV, together with (b) an inset obtained at 950 eV over the region of the highest lying core levels and the valence levels. The highlighted O 1s and Mn 3s spectra have been studied as a function of temperature, as shown in the next figure (from Ref. [84]).

the Mn 3d contributions to the valence spectra of a compound such as the colossal magnetoresistive oxide shown in Fig. 6 [63]). Extending this kind of resonant photoemission study into the hard X-ray regime has also been discussed recently [64]. It has also been pointed out that resonant photoemission can occur between levels on different atoms, as e.g. between O 1s and Mn 3d in the compound MnO [42], with this type of multi-atom resonant photoemission (MARPE) effect providing the potential of uniquely identifying near-neighbors to a given atomic species. In the later article of Fujikawa, the theory of MARPE is discussed in detail. As a final interesting new aspect of RPE, it has been pointed out that XPD carried out at a resonant energy can be used to enhance the emission from certain types of atoms in a system [65]; thus resonant X-ray photoelectron diffraction (rXPD) has recently emerged as a potentially useful new technique for the future, and we discuss one example of its application below.

5. Valence-level spectra-angle-resolved photoemission (ARPES) and the XPS limit

If the emission is from a valence level that is delocalized over many sites due to chemical bonding and molecular orbital or electronic band formation, additional anisotropy in emission is found, and this can be measured, for example, by taking advantage of another property of the hemispherical electrostatic analyzer with a two-dimensional (2D) imaging detector, as shown in Fig. 1(c) for emission from *W*(1 1 0) [66]. In this case, a 2D image in the detector plane can be directly related to the binding energy vs electron momentum or electron wave vector inside the crystal $\vec{k}$, which is then in many cases directly relatable to the band structure, or more precisely the quasi-particle excitation spectrum of the material. Such angle-resolved photoemission (ARPES) measurements are numerous in the literature, they have typically been carried out at energies below ~150 eV, and thus they are not strictly speaking XPS. We consider below some recent promising developments involving energies in approximately the 1–6 keV range.

For most materials at room temperature, the combined effects of phonons and angular averaging in the spectrometer yield X-ray excited ARPES spectra that are directly related to the total density of valence electronic states; this situation has often been referred to as the XPS limit. The existence of this limiting behavior was realized in very early experiments on a family of transition metals [67,68], and there are by now many examples of its application. The effects of phonons in reaching this limit have also been discussed previously [69]. The use of XPS to study densities of states is thus another very productive aspect of the technique, and the article by Knippenberg and Deleuze in this issue discusses this for conjugated aromatic systems.

6. Additional variations on the XPS experiment

6.1. Spin-resolved XPS

If an additional sensitivity to electron spin is somehow built into the detector, e.g. by taking advantage of spin–orbit scattering of high-energy electrons from a heavy-atom target in Mott scattering [70], or low-energy electrons from a heavy atom [71], or a magnetic atom [72], it is possible to measure also the electron spin, providing additional information of particular relevance to magnetic materials. Such measurements were pioneered by Siegmann and co-workers [73]. As an example of such data, Fig. 1(d) shows a more recent measurement of this kind for the valence bands of iron, clearly indicating the difference in the electronic state distributions of spin-up and spin-down electrons for this ferromagnet [74]. The extent of development of this aspect has been limited by the ~10^3 to 10^4 times greater data acquisition times required, but such measurements can provide unique information concerning magnetic systems, and with brighter radiation sources and faster detectors involving low-energy scattering mentioned above, spin-resolved XPS should see expanded usage in the future.

6.2. XPS with hard X-ray excitation

Fig. 1(f) further indicates the option of varying photon energy significantly above and significantly below the energy regime from ~20 to 1500 eV that has been used in most prior photoemission measurements, with the aims of increasing the degree of bulk sensitivity and/or improving energy resolution. As noted in connection with the discussion of Fig. 2, hard X-ray photoemission (HXPS or HAXPES) represents a very promising and rapidly growing new direction which is overviewed in several recent sources [75–77], and discussed in detail by Köver in this issue. I also return to consider a few additional aspect of HXPS later in this article.

6.3. Time-resolved photoemission

There are also newer types of measurements (again Fig. 1(g)) in which some perturbation of the sample is made, e.g. by gas reaction with a clean surface, by short-pulse light excitation, or by short-pulse field exposure and the spectra are measured as a function of time. Depending on the particular process involved, these measurements can be fruitfully carried out on timescales varying from minutes (for surface chemical reactions at higher ambient pressures) down to femtoseconds (for laser or synchrotron radiation pump-and-probe experiments) [78–80]. Some time-resolved studies in conjunction with photoelectron microscopy are considered by Oelsner in a later article in this issue. Looking ahead in the time domain, it seems clear that one exciting application of time-resolved XPS will be to use PD and PH to do time-resolved atomic imaging of small-to-medium sized molecules or of the local environment of atoms around an emitter near a surface. It has been obvious from the beginning of solid-state PD that it represents a way to look at local atomic structure in an element-specific way "from the inside out", and this has more recently also been recognized by the molecular physics community [81]. In this case, the exciting source would be a very short X-ray pulse from a free-electron laser or next generation X-ray source, and this could be moved in time delay relative to some other pulse which initiates an electronic or atomic structural change. Such "molecular movies"

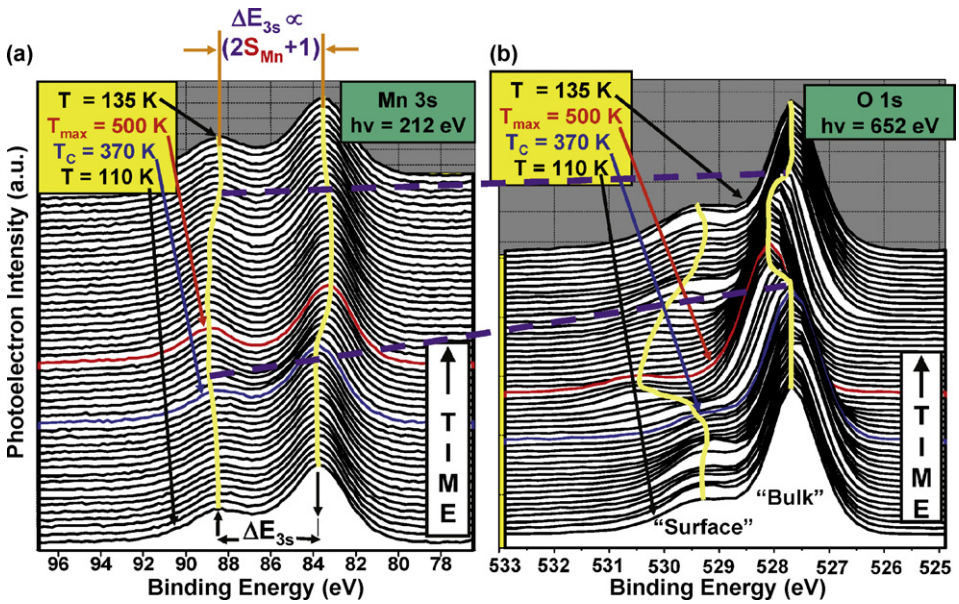

Fig. 7. Temperature dependence of the Mn 3s and O 1s spectra from a freshly fractured surface of $La_{0.7}Sr_{0.3}MnO_3$ (cf. Fig. 6). The two photon energies indicated have been chosen so that the photoelectrons in both cases have very nearly the same kinetic energy and thus the same inelastic attenuation lengths and surface sensitivity (from Ref. [84]).

would enable for the first time directly viewing atomic and electronic dynamics on their inherent timescales. It is not yet clear how easy it will be to use such ultrabright sources on solid samples and surfaces, but with future developments in large-scale multiplexing analyzer/detector combinations, e.g. by using time-of-flight methods, it is definitely in the realm of possibility. Gas-phase experiments from which small-molecule atomic movies will result seem certain to succeed to some degree in the not-too-distant future, as discussed further below.

6.4. XPS at multi-torr pressures

Finally, Fig. 1(h) indicates that it is possible with special differential pumping outside the sample region to carry out studies at up to several torr of pressure [82,83], and this is another rapidly growing area of activity, as discussed in more detail later in this article.

There is thus an extremely rich and steadily growing array of effects and methods in X-ray photoelectron spectroscopy and I will now turn to a few recent examples, drawn both from the work of my group and its collaborators and from other groups as appropriate, to illustrate some promising applications and future directions.

7. Applying multiple electron spectroscopies to a complex strongly correlated oxide—$La_{1-x}Sr_xMnO_3$

As a recent example of the use of a variety of effects in XPS spectra, including spectra obtained with hard X-ray excitation, I consider some recent studies of the colossal magnetoresistive oxide $La_{1-x}Sr_xMnO_3$ with $x = 0.3$ and 0.4 [84–86]. This is a strongly

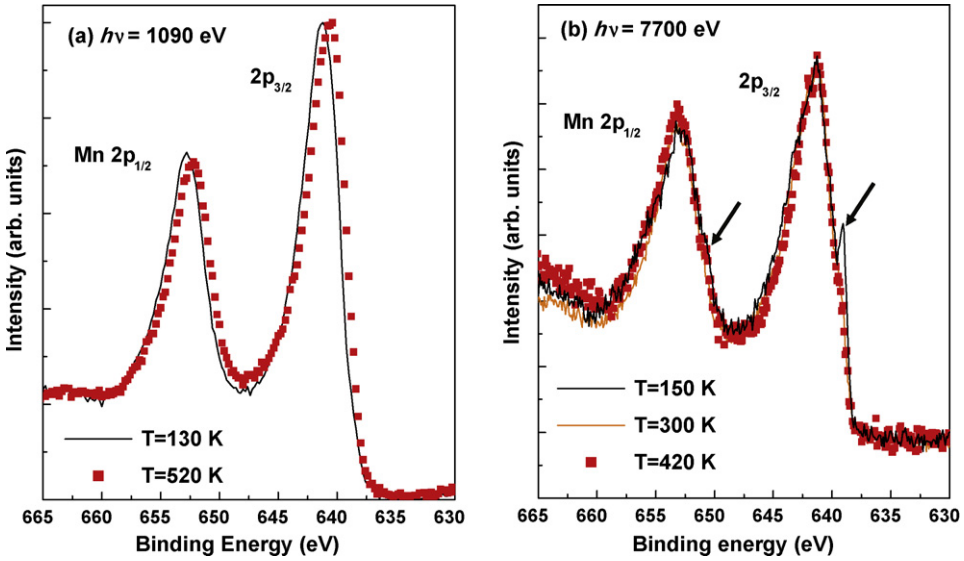

Fig. 8. Mn 2p photoelectron spectra from fractured $La_{0.7}Sr_{0.3}MnO_3$ surfaces at two different photon energies of (a) 1090 eV and (b) 7700 eV, and for temperatures below and above the Curie temperature of 370 K. The arrows in (b) highlight two low-binding-energy satellite features, a very sharp one on $2p_{3/2}$ and a small shoulder on the $2p_{1/2}$ peak, that are thought to arise from bulk-like long-range screening processes (from Ref. [86]).

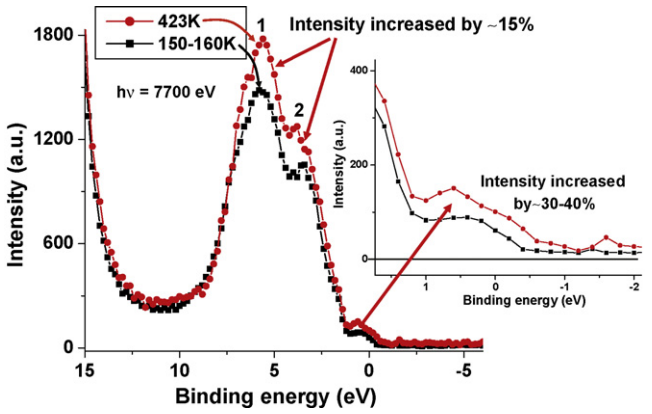

Fig. 9. Valence photoelectron spectra excited at a photon energy of 7700 eV from a fractured $La_{0.7}Sr_{0.3}MnO_3$ surface at two different temperatures above and below T_C. The only normalization done between the two spectra is to force the close-lying Sr 4p and La 5p intensities to be equal. The inset shows an expansion for the region near the Fermi level (from Ref. [86]).

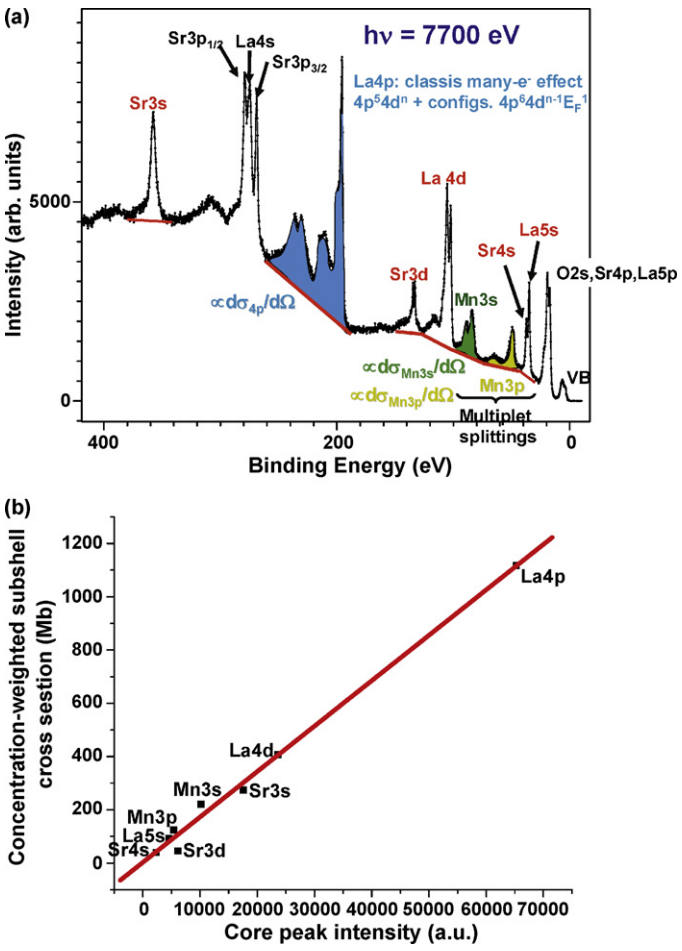

Fig. 10. (a) High-lying core and valence-level survey spectrum from a fractured $La_{0.7}Sr_{0.3}MnO_3$ sample, with the origins of all features labelled, including multiplet splittings of Mn 3s and 3p, as well as many-body final-state mixing for La 4p. Peak areas were measured for eight of the labelled peaks. (b) Peak areas from (a) are compared to a product of stoichiometric concentration and differential photoelectric cross-section, thus assuming a constant analyzer transmission function and that the IMFPs for all peaks are identical (from Ref. [90]).

correlated material that is also thought to be a half-metallic ferromagnet and is of interest for spintronic applications. The chemical and magnetic state of the Mn atoms is thus a key factor influencing the behavior of this material. In Fig. 6 are (a) broad and (b) zoomed survey spectra indicating all the relevant photoelectron and Auger peaks observed with excitation of $La_{0.7}Sr_{0.3}MnO_3$ in the typical XPS regime of ~1 keV [84]. The valence-band (VB) region in Fig. 6(b) is expected to be dominated by Mn 3d character, as the 3d cross-section at 950 eV is about 5× larger than that of O 2p that is admixed with it. The oxide surface was here prepared by cleaving, or more precisely, fracturing, a single crystal in UHV, in order to minimize surface contamination. In Fig. 7(b), we show the temperature dependence of the O 1s spectra from the same sample. Firstly, these O1s spectra exhibit a main peak and a weaker peak at about 1.5 eV higher binding energy. From various measurements, including varying the electron takeoff angle to change the degree of surface sensitivity (see earlier discussion), it is concluded that the peak at higher binding energy is due to O atoms near/at the surface, with the other peak representing O atoms deeper within the material and denoted "Bulk" in the figure. Now considering the changes in these spectra as temperature is varied from well below to well above the temperature at which long-range ferromagnetic order disappears (the Curie temperature, T_C, which is 370 K for this material) and then cooled to near the starting temperature again, a distinct shift in the bulk O 1s binding energy to higher values is observed as T goes up to about 150 K above T_C, together with a concomitant shift, broadening and loss of intensity in the O 1s surface peak. Upon cooling again to below T_C, both features return to their previous states. The bulk peak shift has been interpreted as a transfer of electron charge to Mn from the six O atoms arranged in an octahedron around each Mn atom, via classic qualitative reasoning for chemical shifts and charge transfer [84].

Fig. 7(a) further shows the temperature dependence of the Mn 3s splitting in $La_{0.7}Sr_{0.3}MnO_3$, and it exhibits a marked increase of about 1 eV or 20% over the same temperature range as the O 1s chemical shifts discussed previously. This increase has been interpreted as being caused by an increase in the Mn spin that is equivalent to a net transfer of one electronic charge from the O atoms to Mn, an effect not observed previously [84].

As an example of what can been seen in addition for this system with hard X-ray photoemission, we compare in Fig. 8 temperature-dependent Mn 2p spectra from the same type of colossal magnetoresistive oxide sample involved in Figs. 6 and 7, excited by (a) soft X-rays and (b) hard X-rays [86]. The data in Fig. 8(a) obtained at an excitation energy of 1090 eV, corresponding to kinetic energies of ~450 eV and an inelastic mean free path of ~10 Å [23], are compared with data in Fig. 8(b) obtained at 7700 eV, corresponding to kinetic energies of ~7050 eV and an inelastic mean free path of ~85 Å [23]. Thus, the latter represents a much truer sampling of bulk properties. Although the general shape of the doublet is the same at the two energies, there are two significant differences. First and most obvious in the hard X-ray spectrum is a small, but very sharp, satellite that appears below T_C on the low-binding-energy side of the $2p_{3/2}$ peak, but which is only hinted at in the lower-energy more-surface-sensitive spectrum. There is also an indication of the same satellite, although less well resolved, on the $2p_{1/2}$ peak, as indicated by the arrow. This type of satellite has been observed in HXPS from other manganite and strongly correlated oxide samples, and it has been interpreted as a screening satellite associated with highly delocalized electrons [87–89], with the implication that it requires the extended volume of a more bulk-sensitive measurement to see it. This satellite is also observed to slowly disappear as temperature is raised, which implies a connection with either magnetic order or a lattice that is free of the kind of lattice distortion above T_C that is thought to produce the effects seen in Fig. 7 [84]. A second difference between the hard X-ray and soft X-ray spectra is that a chemical shift with soft X-ray excitation of both Mn 2p components to higher binding energy by about 0.7 eV on lowering the temperature to about 150 K, and

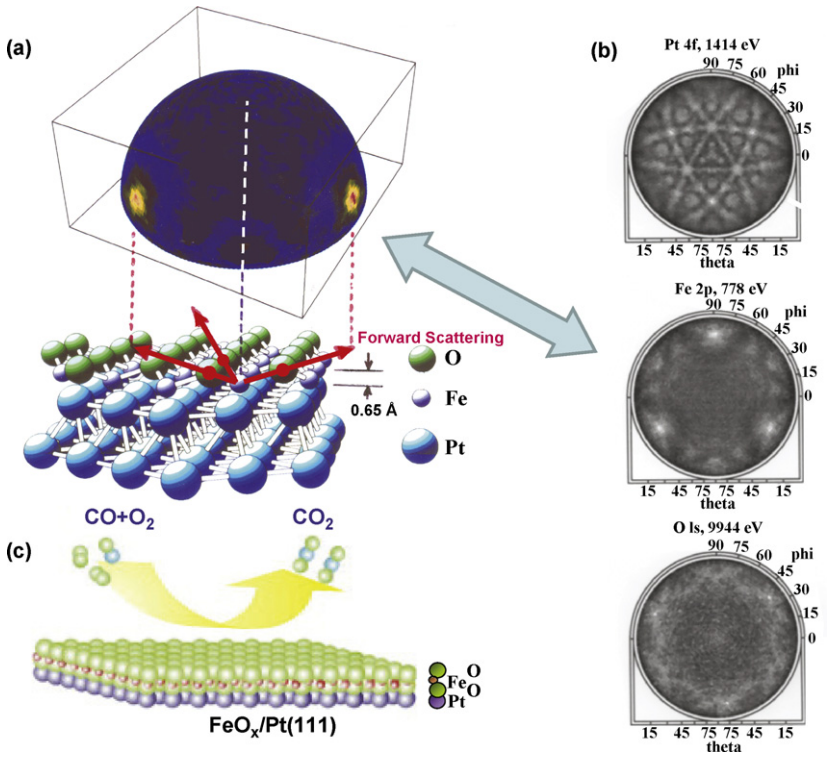

Fig. 11. X-ray photoelectron diffraction at 1486.7 eV excitation from a monolayer of FeO grown on Pt(1 1 1). (a) A full-hemisphere pattern for Fe 2p emission is shown, above the atomic geometry finally determined for this overlayer. (b) Two-dimensional projections of diffraction patterns simultaneously accumulated for emission from Pt 4f (kinetic energy 1414 eV), Fe 2p (778 eV), and O 1s (944 eV) (from Ref. [91]). (c) The O–Fe–O bilayer geometry to which this FeO overlayer is hypothesized to convert when it catalyzes the oxidation of CO (from Ref. [92]).

which has been linked to the O-to-Mn charge transfer discussed in connection with Fig. 7 [84,85], is difficult to discern with hard X-ray excitation. Beyond this, the changes in the Mn 3s multiplet splitting with temperature are found to be less with hard X-ray excitation [86]. Taken together, these results suggest that the effects seen in Fig. 7 are more localized near the surface, within approximately the first 30–40 Å. Combining soft and hard X-ray photoemission has thus been very useful in determining the effective depths of these effects.

Fig. 9 now shows the temperature dependence of the valence spectra from $La_{0.7}Sr_{0.3}MnO_3$ with hard X-ray excitation [86], and

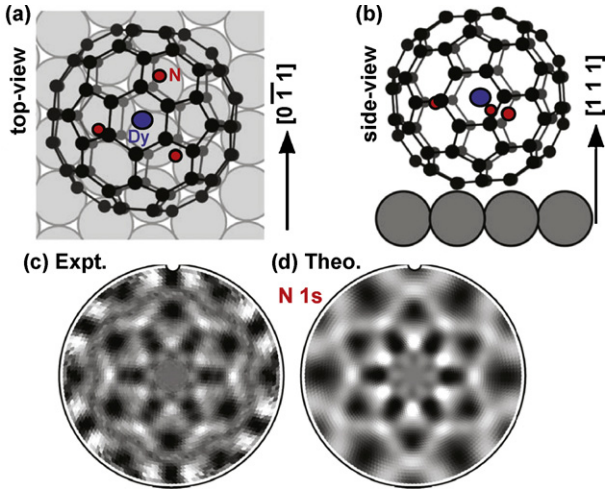

Fig. 12. (a) and (b) Two views of the adsorption geometry of the endofullerene DyN_3 in C_{80}, as determined from a combination of STM, XPD, and resonant XPD. (c) and (d) Experimental and theoretical diffraction patterns for emission from the three N emitters in the system, respectively (from Ref. [93]).

illustrates another useful aspect of such HXPS measurements: deriving information on valence population changes with temperature or composition. These spectra have been normalized to the combined Sr 4p, and La 5p core-level intensities nearby (see Fig. 6(b)), which are not expected to change with temperature. With this normalization, it is clear that the valence spectra change in relative intensity, exhibiting increased intensity at the higher temperature. Considerations of the relative magnitudes of the relevant valence atomic cross-sections at this energy for Mn 3d, Mn 4s, and O 2p, as well as the expected relative populations of these orbitals in the valence bands as estimated from local-density theory, leads to the conclusion that the increases in the valence-band intensity in this figure further confirm an increase in the Mn 3d population at high temperature, as first concluded based on the data in Fig. 7.

As a final aspect of the hard X-ray data for this manganite, Fig. 10(a) shows a survey spectrum including the valence levels and a number of core levels, with all peaks labelled [90]. The core peaks illustrate two different types of final-state effects: the Mn 3s and Mn 3p spectra exhibit multiplet splittings, and the La 4p region is distributed in a complex way over about 30 eV due to the mixing of final states with configurations $4p^5 4d^{10}$ and $4p^5 4d^9 E_F{}^1$, both well-known from previous studies [5,6]. The areas of various peaks connected with all of the atoms in the sample have been measured by subtracting the backgrounds shown, and being careful to include all final states associated with a given core hole. Thus all of the multiplet structure for Mn 3s and 3p, and all of the final-state mixing for La 4p have been included in estimating their respective intensities. In Fig. 10(b) is now shown a plot of these experimental intensities vs the concentration-weighted differential cross-section for each core level, assuming that, for this high-quality single crystal with a freshly fractured surface, the stoichiometry probed by photoemission is that of $La_{0.7}Sr_{0.3}MnO_3$. The resulting plot is linear, with most peaks falling within +/− 10% of a straight line, with no correction for the spectrometer transmission function. This illustrates other

advantages of HXPS: (1) to a good approximation, the spectrometer transmission will be constant over the valence and high-lying core region, as the retard ratio changes very little; in this case the electron kinetic energies in Fig. 10(a) vary only over electron kinetic energies of 7300–7700 eV, so for retardation to the energy of analysis of 200 eV used here, the retard ratio changed only from 0.0273 to 0.0259. (2) The inelastic mean free path, and thus mean emission depth, which is expected to vary roughly as $E_{kin}^{0.75-1.10}$, can also be assumed constant over this spectral range also, changing by only about 5% over the spectrum. Thus, quantitative analysis of spectra to determine stoichiometries in complex materials will be more reliable with hard X-ray excitation, while keeping in mind that all final states reached must be included in peak area determinations.

The further application of this type of combined soft and hard X-ray photoemission to other strongly correlated materials or complex multicomponent materials is thus a very promising area for the future.

8. Photoelectron diffraction and photoelectron holography

8.1. Application to oxide overlayer growth and fullerene adsorption

As one example of how XPD can be used, in what was a study with complementary information from STM and LEED, we show in Fig. 11(a) the full-hemisphere intensity distribution for Fe 2p emission at 778 eV kinetic energy from a monolayer of FeO grown on a Pt(1 1 1) surface [91]. At this energy, the forward-peaked nature of the electron scattering is observed to create strong peaks in intensity along the Fe–O bond directions, as well as first-order interference around these peaks (cf. Fig. 3(d) for 1 keV). The angle at which the forward scattering peaks are seen can furthermore be used to estimate the distance between the Fe and O atoms in the overlayer, and it is found to be only about half that for similar bilayer planes in bulk FeO, as illustrated in the bottom of Fig. 11(a). Fig. 11(b) also illustrates the element-specific structural information available from XPD. The Pt 4f XPD pattern from the same sample is rich in structure due to the fact that emission arises from multiple depths into the crystal, with forward scattering producing peaks and other diffraction features along low-index directions. The bands of intensity in the Pt pattern can be ascribed to Kikuchi bands, as discussed further below. The Fe 2p pattern is here just a projection onto 2D of the 3D image in Fig. 11(a). The O 1s pattern shows only very weak structure, as the O atoms are on top of the overlayer, with no forward scatterers above them, and only weaker side and back scattering contributing to the diffraction pattern. Comparing the Fe and O patterns thus immediately permits concluding that Fe is below O in the overlayer, rather than vice versa. It is also interesting to note that this FeO monolayer has very recently been found to be catalytically very active, in particular for the low-temperature oxidation of CO [92], suggesting future applications of such monolayer oxide catalysts. For the bilayer FeO case, it is further hypothesized that a double-layer O–Fe–O sandwich forms at the surface as it actually becomes involved in catalysis, as illustrated in Fig. 11(c) [92]. Doing O 1s XPD on this double-layer would immediately show by forward scattering peaks for emission from the bottom O layer due to both Fe and O in the layers above that this hypothesis is correct, an obvious interesting future experiment.

As another recent example of XPD as applied to a much more complex structure, a fullerene-based system, Fig. 12(a) and (b) shows two views of the atomic geometry expected when a C_{80} fullerene enclosing a DyN_3 molecule is adsorbed in an ordered array on Cu(1 1 1) [93]. Fig. 12(c) and (d) shows the experimental N 1s XPD pattern (a) and compares it to a theoretical pattern (b) that permits, together with separate resonant XPD patterns of the Dy MNN Auger intensities, concluding that the N atoms occupy very nearly the center of the C_{80} cage, while the endohedral DyN_3 unit takes at least two symmetry-inequivalent, but closely related, orientations in the C_{80} cages on the substrate surface. Even though there are in addition three slightly symmetry-inequivalent N-atom emitters for each DyN_3 unit in this system, the complex XPD pattern could be analyzed to derive useful structural results. It is also worth noting that, in this and other cases involving XPD from adsorbates, the simplification of using only a single-scattering cluster (SSC) type of theoretical modelling is found to be adequate. For emission from atoms in a bulk crystal or significantly below a surface, multiple scattering along rows of atoms must be considered for quantitative XPD modelling [45].

Many other examples of photoelectron diffraction in the study of clean surfaces, adsorbates, and nanostructure growth appear elsewhere [45,94,95], including discussions of an alternative method of PD measurement in which the geometry is held fixed and the photon energy is scanned [45,96], the principle focus of the article by Woodruff in this issue.

8.2. Hard X-ray photoelectron diffraction

As another future direction in XPD, we consider what might be possible by exciting with energies of several keV, as treated in a recent theoretical study [97] and demonstrated in some first experimental data [98,99]. Fig. 3 and Eq. (4) have already provided an introduction to the general systematics expected, with highly forward-peaked elastic scattering dominating the patterns, and any higher-order diffraction features being weaker and more closely spaced in angle. Beyond this, however, the higher inelastic mean free paths lead to the sampling of many more atomic layers in emission from a multilayer substrate, with effects of Bragg scattering from different sets of planes becoming visible. In this limit, the diffraction of the photoelectrons is better treated as a multiple Bragg scattering (also referred to as dynamical scattering) process leading to Kikuchi bands of intensity, as was in fact qualitatively recognized in the first XPD study [55]. From a theoretical point of view, this implies going from an atomic cluster formulation of the problem to one involving multiple scattering from Bragg planes, in what can be considered a time-reversed low-energy electron diffraction (LEED) picture with the surface explicitly included [97]. In fact, above around 5 keV, it begins to be difficult to use the cluster picture that is common in XPD algorithms [44], due among other things to the large number of scattering phase shifts (cf. Fig. 3) and the large atomic clusters required. For example, calculation times in the cluster approach scale roughly as ${N_{cluster}}^2\ (l_{\max}+1)^3$, where $N_{cluster}$ is the number of atoms in the cluster. A family of Bragg-based dynamical theoretical calculations over the energy range of 0.5–20 keV for emission from diamond is shown in Fig. 13(b) [97], where that for 1 keV can be directly compared to experiment in Fig. 13(a) [100]. The agreement between experiment and theory at 1 keV is excellent, including many fine-structure features. The expectation on going to higher energies is for sharper and sharper Kikuchi-band like features, as seen in the other panels of this figure. Further consideration of such calculations indicates that hard X-ray photoelectron diffraction (HXPD) should provide a very sensitive method for the element-specific bulk-sensitive determination of the positions of atoms in a complex lattice (for example, substitutional vs interstitial sites), as well as of lattice relaxations [97].

As an example of experimental HXPD, as well as hard X-ray ARXPS data obtained to date, Fig. 14 shows results of exciting Si 1s photoelectrons from clean Si(0 0 1) and Si(0 0 1) with 4 nm of native oxide on top with synchrotron radiation at 7.94 keV (panel (b)) and with monochromated Cr $K\alpha_{1,2}$ X-rays at 5.4 keV (panels (c) and (d)) [99]. These data have been obtained with a specially adapted commercial hemispherical analyzer–lens com-

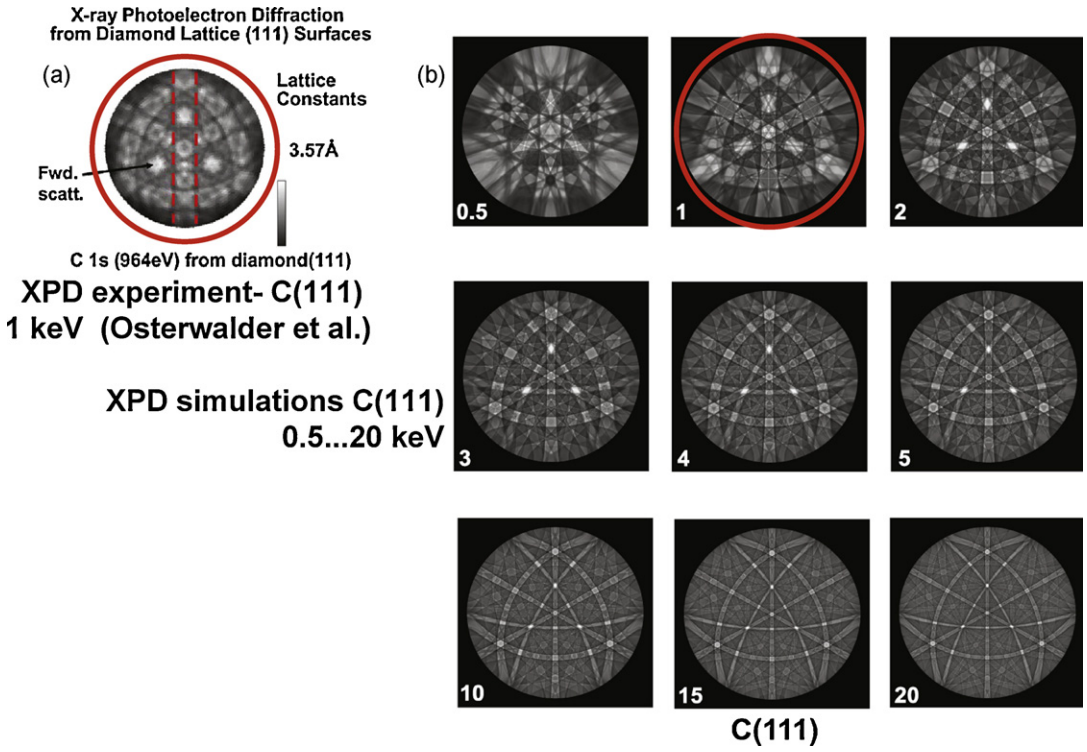

Fig. 13. (a) An experimental full photoelectron diffraction pattern from diamond (1 1 1) at 964 eV kinetic energy (from Ref. [100]). (b) Calculations using a Bragg reflection/Kikuchi band approach for photoelectron diffraction and going up to 20 keV in energy (from Ref. [97]).

bination that has been fitted with a wide-angle prelens and a bent-crystal X-ray monochromator in the Rowland circle geometry. Energy resolutions of ca. 0.26 eV at 7.94 keV and 0.50 eV at 5.4 keV and angular resolutions of 1° are achieved over approximately a large ±35° in detector θ (cf. Fig. 1). The Si^0 and combined $Si^{3+,4+}$ peaks in the presence of oxide are clearly resolvable in Fig. 14(a). In Fig. 14(b) a single detector image over the full angle range is shown for the oxidized sample. The relative enhancement of the oxide single relative to the normalized Si^0 signal is obvious, indicating that ARXPS can be performed quickly over a large-angle range with such an instrument, as also practiced with some commercial XPS spectrometers, but over a smaller angle range. Also, by rotating the sample in azimuth ϕ (cf. Fig. 1) and combining results, a large section of a hemispherical XPD pattern can be obtained. The Si^0 peak shows strong XPD effects in emission from the clean Si(0 0 1) surface in Fig. 14(c), with the clear presence of both forward scattering along low-index directions and Kikuchi bands (cf. Fig. 11(b) for Pt 4f and Fig. 13(a)). Fig. 14(d) illustrates the damping effect of the amorphous 4 nm layer of SiO_2, although there are residual Si XPD effects even with this relatively thick overlayer present. In other data, not shown here, the combined $Si^{3+,4+}$ peaks are found to show no XPD features, consistent with the expected amorphous character of the oxide.

HXPD and hard X-ray ARXPS experiments are thus just beginning, and this aspect of the technique awaits future development, but instruments such as that described above should make such data much more accessible, and the result should be a new tool for looking at local atomic structure in buried layers or in complex bulk materials. As one interesting type of experiment that awaits future trial, one can imagine tuning the hard X-ray incidence angle to an atomic-plane Bragg reflection, and then observing the HXPD patterns and the valence-band spectra as either the angle is varied over a rocking curve or the photon energy is scanned over the Bragg energy. This sort of "double-Bragg" experiment, in which both photons and electrons are Bragg scattering, but in general from different sets of planes, should permit even more precisely determining both local atomic structure and decomposing valence-band densities of state in an element-specific way.

8.3. Photoelectron holography

As noted earlier, a photoelectron diffraction pattern can also to a first approximation be considered a photoelectron hologram [101]. This has led to several studies in which diffraction patterns at various angles and/or various energies have been mathematically transformed so as to directly yield atomic positions in space. More precisely, if the photoelectron diffraction intensities $I(\vec{k})$ are measured over several angles and/or energies, equivalent to some volume in $\vec{k}$-space, and then normalized by subtracting out the smoother unscattered intensity profile I_0 corresponding to an unscattered reference wave to yield a function $\chi(\vec{k}) = [I(\vec{k}) - I_0(\vec{k})]/I_0(\vec{k})$, then the holographic image of the atoms neighboring the emitter $U(\vec{r})$ can be obtained from:

$$U(\vec{r}) = \left| \iiint \chi(\vec{k}) \exp[i\vec{k}\bullet\vec{r} - ikr] d^3k \right|, \quad (5)$$

where the exponential phase factor is that appropriate to the phase difference between the reference wave and an object wave scattered from point $\vec{r}$, and the integral is over the volume in $\vec{k}$-space covered by the data points.

As one example of this approach, I show in Fig. 15 a holographic image obtained using Cu 3p photoelectron intensities above a Cu(0 0 1) surface, with the emitter (e) as the central reference point [102]. These images were actually obtained using a differential approach in which two holograms at slightly different energies are subtracted from one another so as to suppress forward scattering effects, which are deleterious as far as holography is concerned. Using this approach, it is clear that one can image about 15 near-neighbor atoms below and to the sides of the emitter. Other future possibilities with photoelectron hologra-

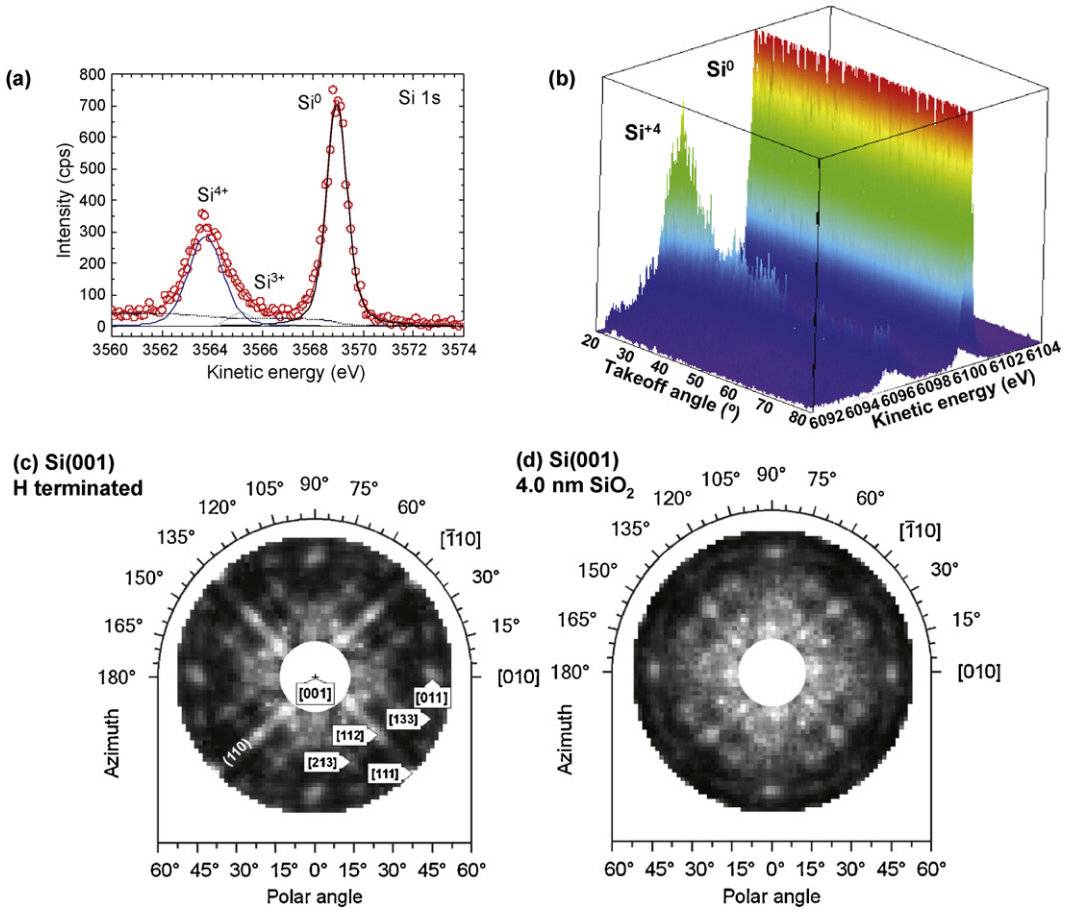

Fig. 14. Hard X-ray angle-resolved XPS (ARXPS-(b)) and X-ray photoelectron diffraction (HXPD-(c) and (d)). (a) A Si 1s spectrum from a Si sample with 4 nm of oxide on top, excited with monochromatized Cr Kα radiation at 5.4 keV, with different oxidation states labelled. (b) Multichannel Si 1s ARXPS data excited at 7.94 keV from a sample such as that in (a) and simultaneously obtained over a wide-angle range with a special prelens. (c) Large solid-angle hard X-ray XPD from Si^0 1s of Si(0 0 1) excited by Cr Kα and thus a kinetic energy of 3569 eV, with the data obtained from single detector images at various azimuthal orientations of the sample. (d) As (c), but with 4 nm of SiO_2 on top (from Ref. [99]).

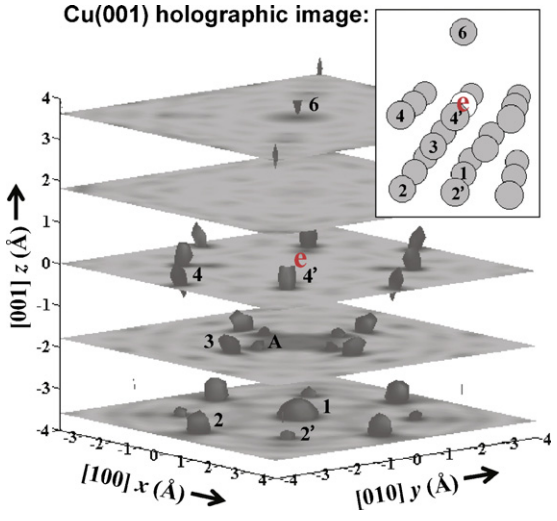

Fig. 15. Holographic image of the atoms neighboring a given reference Cu atom below a Cu(0 0 1) surface, based on a differential method in which holograms at two close-lying energies are subtracted from one another to reduce forward scattering effects. The typical reference emitter atom is noted by "e", and the neighboring atoms are indicated in the inset. The data yielding this image consisted of Cu 3p spectra at 25 kinetic energies from 77 to 330 eV and over 65 directions, thus representing about 1600 data points in k-space (from Ref. [102]).

phy, including making use of spin resolution and circular dichroism, are discussed elsewhere [57]. It should be noted, however that PH becomes more challenging at higher photoelectron energies due to the increasing importance of forward scattering and the weaker nature of the holographic fringes (cf. Fig. 3), although the differential approach mentioned above, and an alternative "near-node" approach in which the polarization vector is oriented such that the direct wave is near zero in the forward scattering direction [103], both can be used to compensate somewhat the deleterious effects on images of forward scattering [57].

It is also possible that PH could be used to directly image small molecules or local atomic clusters in a time-resolved mode, as discussed previously.

9. Photoemission with standing wave excitation and other X-ray optical effects

9.1. Basic methodology and the standing wave/wedge ("swedge") method

Carrying out measurements in an experimental geometry for which the reflectivity is high enough that the exciting radiation generates a significant standing wave represents a relatively newly developed method for selectively exciting at certain positions within the sample. As indicated in Fig. 16, the period of the square magnitude of the standing wave *E*-field will be given by $\lambda_{SW}(|E^2|) = \lambda_x/2\sin\theta_{inc}$, where λ_x is the X-ray wavelength. Going

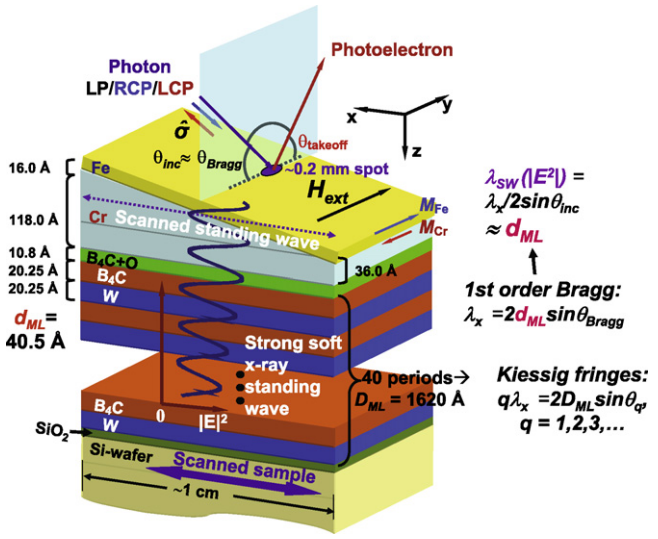

Fig. 16. Schematic illustration of the simultaneous use of an X-ray standing wave created by reflection from a multilayer mirror plus a wedge-profile overlayer sample to selectively study buried interfaces and layers—the "swedge" method. In the example here, a strong standing wave (SW) is created by first-order Bragg reflection from a multilayer made of repeated B_4C/W bilayers, and a Cr wedge underneath an Fe overlayer permits scanning the SW through the Fe/Cr interface by scanning the sample, and thus the X-ray spot, along the *x* direction. The two relevant equations for predicting the period of the standing wave along the *z* direction in conjunction with Bragg reflection from the multilayer are also shown. In addition, the equation for predicting Kiessig fringes in angular scans (rocking curves) is given. Other precise geometric parameters for the specific study in Ref [33] are also indicated (from Ref. [33]).

into a grazing-incidence total reflection geometry is one way to achieve high reflectivity [104]. Or, if the excitation is at a high enough energy (a short enough electron de Broglie wavelength λ_e) to permit Bragg reflection from crystal planes, then a standing wave parallel to a given set of Bragg planes $\{h\,k\,\ell\}$ can be generated; in this case, the SW period for first-order reflection is just the planar spacing $d_{h\,k\,\ell}$ [104–106]. In such a Bragg geometry, scanning the incidence angle over the Bragg angle, or scanning the photon energy over the Bragg energy, sweeps the SW vertically by about 1/2 to 3/4 of λ_{SW}, thus also moving it through the unit cell, and providing via core-level intensities information on atomic positions near a surface [31], or, by using both core and valence-level intensities, element-specific densities of states [32]. The latter is discussed by Zegenhagen in this issue. Another possibility is using reflection from a synthetic multilayer mirror to generate the SW, with this yielding in first-order reflection a SW period equal to the multilayer period d_{ML} (cf. Fig. 16) and permitting depth-resolved studies of nanometer-scale multilayer structures [33,104–106]. Finally, Fig. 16 indicates an additional type of fine structure that can be seen in scanned-angle or rocking curve measurements: Kiessig fringes. These result from the interference of waves reflecting from the top and bottom of the full multilayer, with thickness D_{ML}, leading to SW field maxima when $q\lambda_x = 2D_{ML}\sin\theta_q$, $q = 1, 2, 3\ldots$. Additional fine structure in a rocking curve can result from reflections at the top and bottom of the wedge, or some other thicker layer(s) in the sample, for which one simply replaces D_{ML} with $D_{effective}$ above.

The basic principle of the multilayer SW method, as amplified by including one wedge-profile layer in the sample, is illustrated in Fig. 16; this figure also includes some specific parameters for the first case studied: the Fe/Cr interface, a prototype system exhibiting giant magnetoresistance (GMR) [33]. A well-focussed soft X-ray synchrotron radiation (SR) beam at between 500 and 6000 eV energy is incident on a synthetic multilayer mirror at its first-order Bragg angle. This leads to a high reflectivity and a strong standing wave (SW) above the mirror. As noted above, if the bilayers making up the mirror (in this example composed of B_4C and *W*) have a thickness d_{ML}, then the period of the SW, as judged by the square of its electric field, also has a period of d_{ML}, as indicated in the figure. Beyond this, the fact that the SW modulation is the result of interference between the incident and reflected beams implies that its intensity will range over maximum limits set by $1 \pm 2\sqrt{R(\theta_{inc}) + R(\theta_{inc})}$, where *R* is the reflectivity at a given incidence angle. Thus, even a modest reflectivity at the Bragg condition of 1% will yield an overall SW modulation of $\pm 2\sqrt{R} \approx \pm 20\%$ via the middle term in this expression. The sample to be studied is then grown on top of the mirror, with its base layer (here Cr) in a wedge profile, and another constant-thickness layer (here Fe), plus perhaps other layers, grown on top of the wedge. The slope of the wedge is such that, over the full sample length along the *x* direction in the figure, it changes in height *z* by a few times the standing wave period d_{ML}. Since the X-ray beam size is ~0.1 mm and much smaller than the typical sample length of ~1 cm, scanning the sample relative to the beam along the wedge slope (the *x* direction) effectively scans the standing wave through the sample. It is important in this context to note that the SW phase is fixed relative to the multilayer during such a scan. Thus, photoelectron or X-ray emission signals from different atoms will exhibit oscillatory behavior that can, in a direct-space manner, be interpreted in terms of depth distributions, with the aid of X-ray optical calculations to accurately simulate the standing wave [107,108].

In practice, this standing wave/wedge (swedge) method is also combined with the more standard SW methods for determining depth-resolved information perpendicular to a set of reflecting planes: scanning the incidence angle over the Bragg reflection condition for a given fixed photon energy, so as to generate a rocking curve, and scanning the photon energy over the Bragg condition for a given fixed incidence angle. In both of these types of scans the SW modulation is negligibly small at the outset well off the Bragg condition, then grows in to a maximum at the Bragg angle, and then decreases to a small value again. Simultaneously, the phase of the SW moves vertically by about 1/2–3/4 of the SW period, thus causing significant changes in photoelectron or X-ray emission intensities. Both of these measurements, combined with appropriate X-ray optical simulations, can be used to determine the Bragg angle at the outset of a swedge experiment, and they also provide complementary depth-resolving information that has been used together with *x*-coordinate scans along the wedge to finally determine the thickness of the wedge for a given *x*-coordinate setting, as well as final depth profiles. A distinct advantage of the swedge approach however, is that several full periods of the SW can be scanned through the sample, and the resulting very nearly sinusoidal oscillations more quantitatively analyzed to determine depth profiles. One feature of such oscillations that is particularly useful is the phase shift between them for different species, which can directly be read as an approximate indicator of position with respect to the surface of the sample. We illustrate this now for a few examples below, including both soft X-ray and hard X-ray excitation.

9.2. Application to a giant magnetoresistive interface

The first results obtained with the swedge method were for the Fe/Cr interface, and they are summarized in Fig. 17. In Fig. 17(a), the two basic types of measurement performed are indicated: (i) a scan of sample position along *x* with the incidence angle fixed at or near the Bragg angle, as discussed previously; and (ii) a rocking-curve scan of incidence angle through the Bragg angle at fixed *x*, or equivalently fixed Cr thickness. The results of both types of scans on the Cr3p/Fe3p intensity ratio are presented in Fig. 17(b) and (c). The roughly sinusoidal oscillations of this ratio in Fig. 17(b) clearly

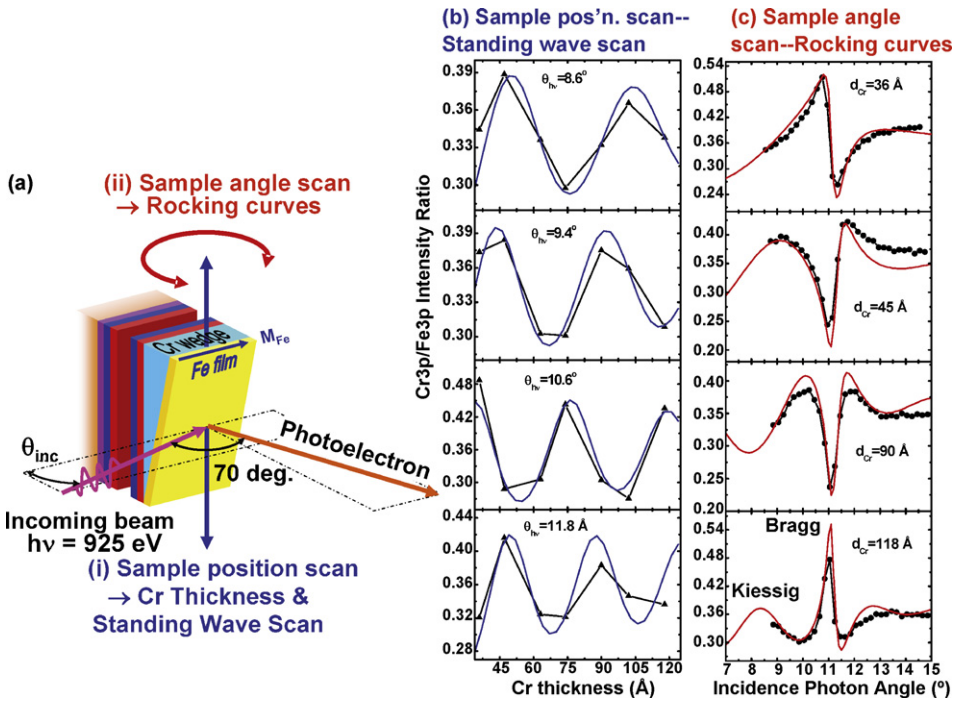

Fig. 17. (a) Two types of scans possible in the standing wave/wedge (swedge) method: (i) Scanning along x or wedge thickness with θ_{inc} fixed at the Bragg angle to yield a direct scan of the standing wave through the layers above the wedge, and (ii) scanning the incidence angle over the Bragg angle with x (or Cr thickness) fixed to yield a rocking curve. (b) and (c) Experimental (points) and calculated (curves) of the Cr3p/Fe3p ratios for these two types of scans, for the sample shown in Fig. 16 (from Ref. [33]).

reflect the passage of the standing wave through the interface. Fig. 17(c) shows the more complex forms that are characteristic of rocking curves, with dramatic changes in the ratio in this data also. There are easily measured modulations of approximately ±15 to ±25% in these ratios. Note also in Fig. 17(c) that the wings of the rocking curve contain Kiessig fringes that are observable in theory, and to a lesser degree in experiment, due to its limited angular range. Self-consistently analyzing the data in Fig. 17(b) and (c) with X-ray optical calculations of standing wave photoemission [107] and only two variable parameters (the depth of onset of the change in the Fe composition and the width of a linear gradient as the interface changes from pure Fe to pure Cr) yielded the excellent fit to both types of data shown in the figure, and permitted determining the position and thickness of the Fe/Cr interface [33]. Adding to this data Fe 2p, Fe 3p, Cr 2p, and Cr 3p MCD measurements (cf. Fig. 5(a)) as a function of position also permitted determining the depth profile of the magnetization of both atoms through the interface. Thus, in this first published example, the swedge method permitted non-destructively determining the concentration profile through an interface, as well as the variation of the element-specific magnetization contributions through it.

9.3. *Application to tunnel magnetoresistive interfaces*

As another example related to spintronics, we consider a prototypical magnetic tunnel junction (MTJ), in which two ferromagnetic layers (e.g. CoFe) are separated by an insulating layer (e.g. Al_2O_3 or MgO), and spin-dependent tunneling interactions can produce a large tunnel magnetoresistance (TMR). Fig. 18 summarizes photoemission data from a sample consisting of an Al_2O_3 wedge varying in thickness from 100 to 55 Å, a layer of CoFe of 25 Å thickness, a layer of CoFeB of 15 Å thickness, and a final protective cap of Al_2O_3 of 10 Å thickness [109]. In Fig. 18(a) is shown the B 1s spectrum, which is split into two components by a large chemical shift. These two components A and B can be verified as two chemically and spatially distinct species by either doing a rocking-curve scan and monitoring the two intensities A and B (Fig. 18(b)) or a scan along the wedge slope (Fig. 18(c)) in which the x position is fixed and the angle of incidence is varied, thereby sweeping the SW position through the sample. The two components A and B have markedly different behavior as a function of SW position. Analysis of the scans shown in Fig. 18(b) and (c), but in particular, the phase shift between the oscillations in Fig. 18(c), reveals that their mean depths are different by about 7 Å and that peak B originates from atoms closer to the surface. A quantitative X-ray optical analysis of both sets of data yields the concentration profiles responsible for these two peaks indicated in Fig. 18(d), and the conclusion that the boron of type B in the CoFeB layer has segregated out into the interface between CoFeB and the Al_2O_3 capping layer [109].

For the same MTJ sample type as in Fig. 18, it has also been possible to use several valence-band spectra obtained as the standing wave is scanned through the sample to yield layer-resolved densities of states, and in particular, to provide an understanding in terms of electronic structure of the marked increase in tunnel magnetoresistance (TMR) when the CoFe layer is decreased in thickness d_{CoFe} from 25 to 15 Å [110].

As another type of MTJ structure studied using the swedge method, we consider a system consisting of an Al_2O_3 wedge varying from 140 to 280 Å in thickness covered by a constant-thickness 15 Å Co layer and a 12 Å Ru cap [109]. One type of sample in this study was produced using a synthetic procedure involving a 30-s final plasma oxidation of the Al_2O_3 just before deposition of the Co, a procedure that has been thought to increase the desired TMR. For such a sample, the Co is found via Co 2p chemical shift analysis to be highly oxidized. Fig. 19(a) shows a reference Co 2p spectrum from the literature, with one sharp feature from metallic Co (Co^0) and two peaks from Co oxide (Co^{2+}) [111]. We find the same spectral features, as shown in the standing wave/wedge (swedge) scan in Fig. 19(b). In the same sense that the two boron species A and B in Fig. 18(a) have a phase shift in Fig. 18(c), so does the single Co metal component have a phase shift of about 16 Å relative to the two components from Co oxide in the Co^{2+} state, as shown clearly in Fig. 19(b). This shift is in turn in a direction indicating that the oxide is situated on average above the metallic Co, rather than below it

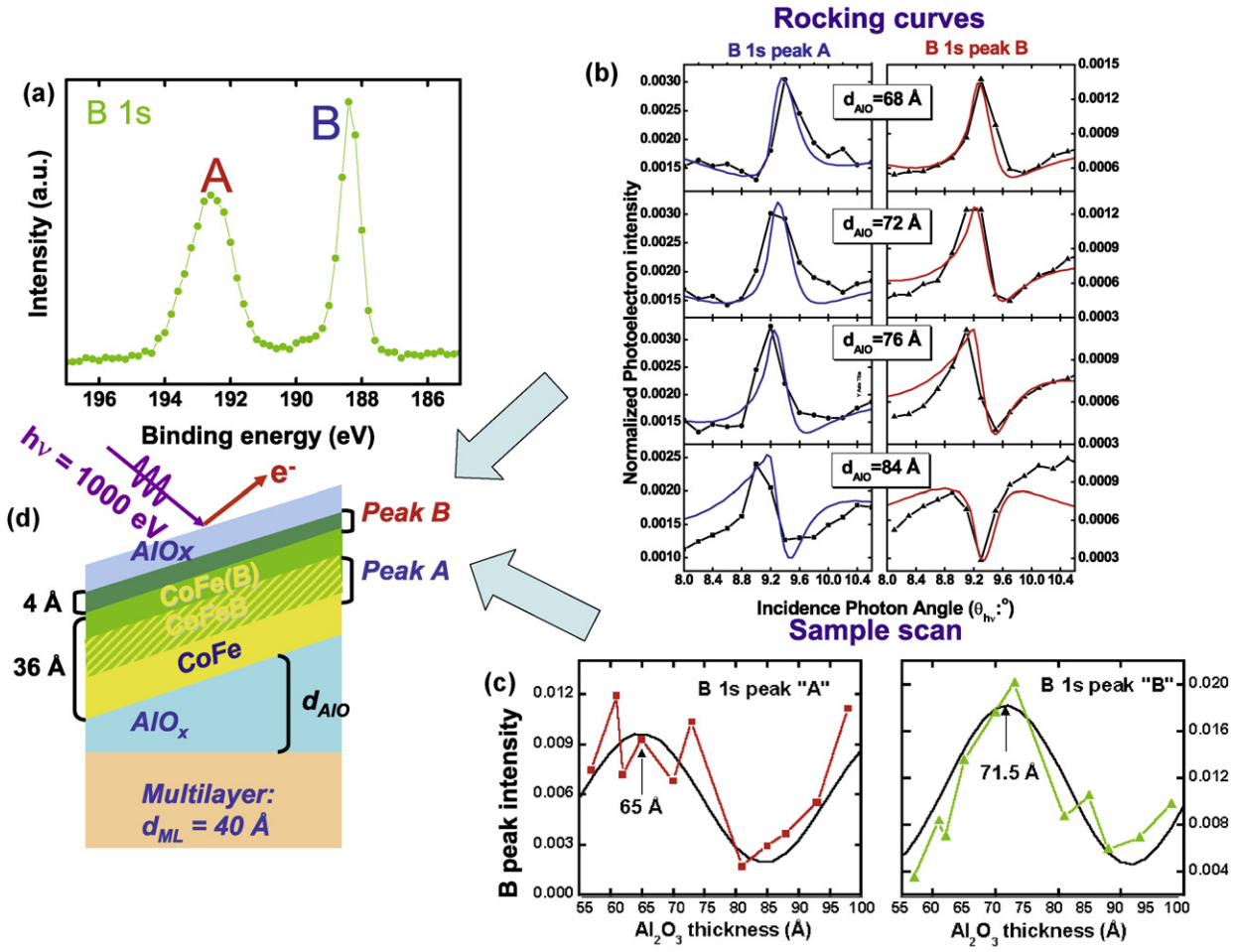

Fig. 18. (a) The boron 1s spectrum from a CoFeB layer on top of a sample with the configuration shown in (d). The photon energy was 1000 eV. (b) The intensity of the two components A and B in (a), obtained by rocking the sample, i.e., by scanning the X-ray incidence angle through the first-order Bragg reflection of the multilayer. (c) The variation of the intensities of peaks A and B as the standing wave is scanned through the sample by moving the sample in the *x* direction (a swedge scan). (d) The distribution of the two types of boron in the sample, as derived from a fit of X-ray optical calculations to the data, with the smooth curves in (b) and (c) representing best fits. Type A has segregated out at the top of the FeCoB layer, leaving a depleted FeCo(B) region. Type B represents boron in the FeCoB layer with original doping level (from Ref. [109]).

and adjacent to the Al_2O_3. Beyond this, the oscillatory patterns seen for the various core-level intensities of different atoms from this sample, as plotted in Fig. 20, yield a family of phase shifts which can be analyzed to determine depth distributions. For example, O 1s is split into what appears to be two metal-oxide components, one that is in phase with Co oxide and nearer to the surface, and one that is in phase with Ru that is below the surface. The metallic Co signal also seems to come from not very far below the Ru on average. These results thus point to a very strong intermixing and/or island formation in the Co and Ru layers, with the relative weakness of the Ru oscillations also suggesting that it has distributed itself over depths that must be approaching the wavelength of the standing wave, which was in this case 40 Å. An approximate picture of the sample profile is shown in the inset of Fig. 19(c), and it is very different from what might have been supposed from the synthetic recipe.

A final example, again of an MTJ structure, is of Fe/MgO and its interfaces, some further soft X-ray excited results from which are illustrated in Fig. 21 [112]. The sample configuration is shown in Fig. 21(a). An Fe wedge varying from 0 to 200 Å in thickness was grown on a Si/Mo multilayer mirror with 39.8 Å period, a 20 Å MgO layer was grown on top of this, and a 20 Å capping layer of Al_2O_3 was finally added to protect the MgO from radiation-induced chemical changes. In Fig. 21(b), the results of wedge scans of several core intensities, as well as the valence-band region are shown. Approximately two full cycles of passage of the SW through the sample layers are observed, with strong modulations of various features in the 20–30% range. Clear phase shifts of the peaks from Al, Mg, and Fe are seen, with these directly giving information on the relative depths of these species from the surface. Beyond this, the valence-band region shows clear changes as well, with the Fe-related DOS features near the Fermi level following the Fe 3p core level in modulation, such that the overlying oxide DOSs are more emphasized at points for which the Fe DOS is a minimum. Fig. 21(c) shows selected valence spectra from the data in (b), which make these changes more evident. Analyzing this data, together with MCD data for Fe 2p emission, has permitted deriving concentration and magnetization profiles through the Fe/MgO interface, as well as extracting the interface density of states for Fe, with the latter suggesting some Fe oxidation at the interface [112].

9.4. Standing wave photoemission with hard X-ray excitation

Beyond the studies mentioned before using Bragg scattering of harder X-rays from crystal planes to create a standing wave [31,32,104], another interesting area for future development is to use much harder X-rays for excitation of photoelectrons above a multilayer mirror, thus going from soft X-rays in the 500–1000 eV regime up to 5 or 10 keV. This would permit penetrating multilayer structures more deeply. It has been pointed out that standing

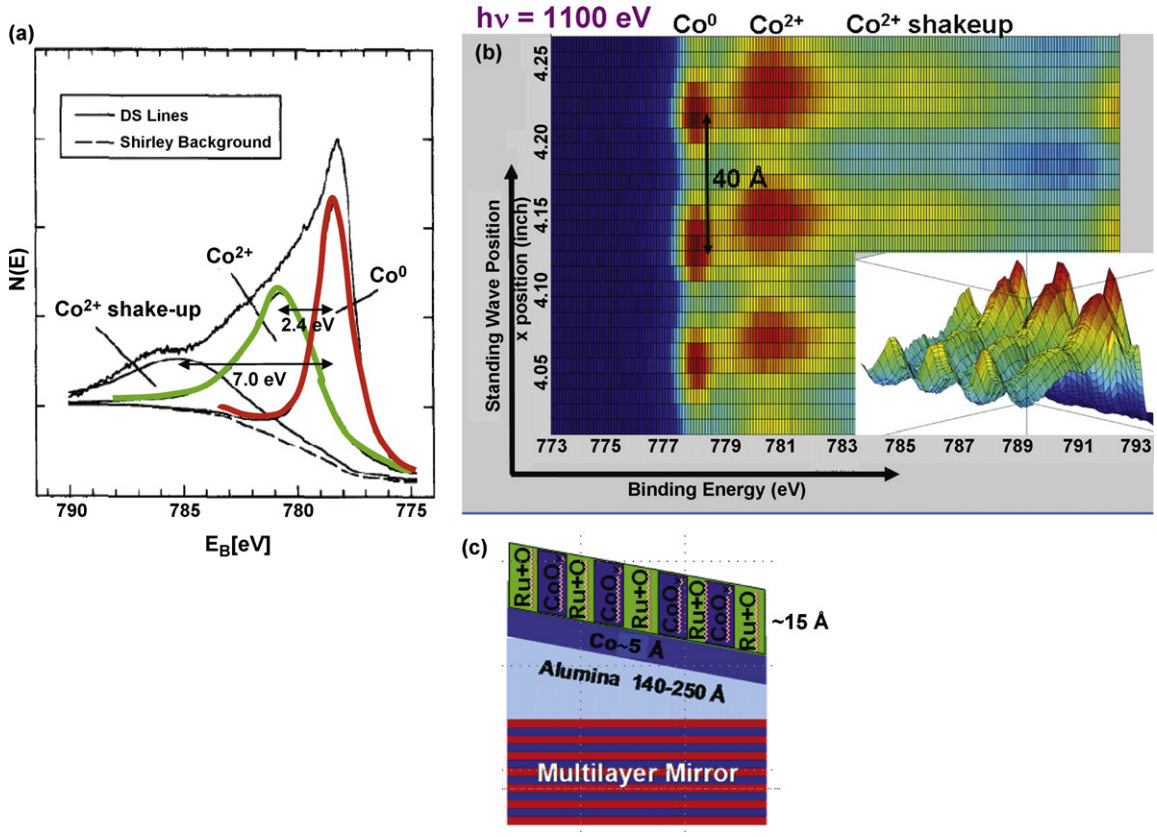

Fig. 19. (a) A Co 2p spectrum from oxidized Co, as obtained from the literature [111], indicating the three features expected: one from Co^0 and two from Co^{2+} (a main peak and a broad shake-up or screening satellite). (b) The effect of scanning the standing wave through a sample consisting of an Al_2O_3 wedge, a Co layer, and a Ru cap, on the Co 2p spectrum [109]. The photon energy was 1100 eV. Note the obvious phase shift between the Co^0- and Co^{2+}-associated peaks. (c) The approximate sample profile as deduced from the data in this figure and in Fig. 20 (from Ref. [109]).

waves above nm-scale multilayer mirrors should be even stronger in this higher-energy regime [113], and thus more accurate characterizations of even deeper structures should be possible. Some encouraging data of this type have in fact recently been obtained [114,115]. Fig. 22 summarizes some of the first data of this type for a sample with the configuration shown in panel (a), very close to that in Fig. 21. Photoelectrons were excited from this nanostructure with 4.0 keV photons [114]. As the X-ray beam is scanned along the wedge, Fig. 22(b) and (c) shows that there are strong oscillations of about 50% in magnitude in core photoelectron intensities arising from the oxide overlayers (Al 1s, O 1s (chemically shifted between the two oxides), and Mg 1s), with about four standing wave cycles

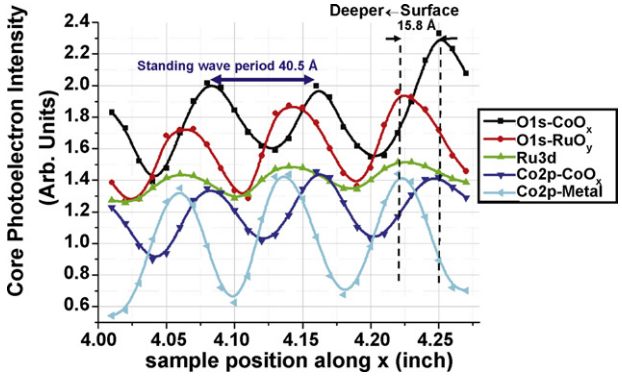

Fig. 20. (a) The oscillatory intensity variations of different core-level photoelectron intensities as the standing wave is scanned through a sample with the configuration shown in Fig. 19(c). The different peaks involved are indicated (from Ref. [109]).

being seen. The Fe oscillations are weaker, at only about 10% overall due to the greater thickness of the Fe wedge, the larger photoelectron IMFPs, and resultant averaging over a couple of SW cycles, but they are still visible, together with a phase shift due to the different effective sensing depths of Al, Mg and O, vs the Fe underneath. These data suggest another fruitful direction of development for HXPS in studying multilayer nanostructures, with applications already to Fe/MgO [114,115] and TiN/Si, a system of relevance to current semiconductor technology [116].

9.5. *Photoelectron microscopy in 3D with standing wave excitation*

As another possibility for the future, carrying out soft X-ray-excited photoelectron microscopy (PEEM) studies with standing wave excitation should provide a type of direct depth sensitivity to these laterally resolving synchrotron radiation based techniques, provided that one or more standing wave cycles can somehow be viewed in a single microscope image or series of images. Some first encouraging measurements of this type have in fact recently been carried out [117], as summarized in Fig. 23. As shown in Fig. 23(a), a multilayer-mirror substrate had grown on it a very narrow Ag wedge and then a bilayer of Co, then Au. This sample was then imaged in a photoelectron microscope, and the standing wave-induced variation of the intensity of a Ag wedge layer in the sample and a C contaminant overlayer could be seen in a single snapshot (Fig. 23(b) and (c)). The phase shift between the Ag and C images due to their different vertical positions relative to the SW is also seen in these figures. By further scanning the photon energy over the Bragg condition, the SW can be seen to move along the wedge

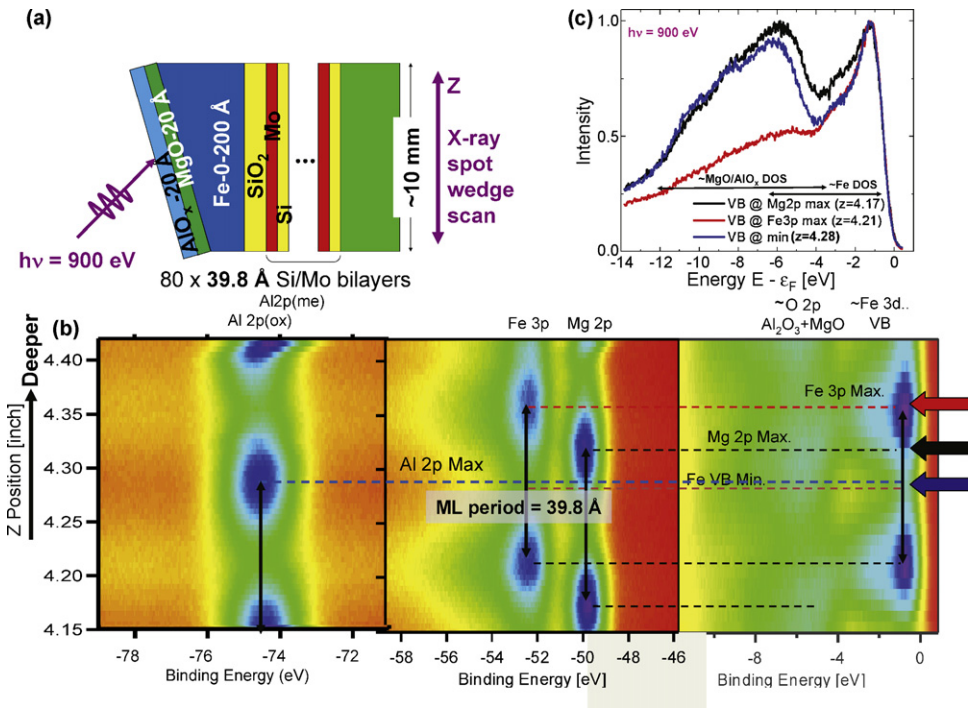

Fig. 21. Soft X-ray standing wave/wedge data for the MgO/Fe magnetic tunnel junction system, with excitation at 900 eV. (a) The sample configuration. (b) Variation of various core and the valence-band intensities as the X-ray spot is scanned along the wedge. The swedge geometry assures that adjacent maxima for a given level are spaced apart in height by precisely the SW period, here 39.8 Å. (c) Three selected valence-band spectra, at the points indicated by the arrows in (b), illustrating the different degrees of emphasizing the Fe DOS near the Fermi level vs the Al_2O_3 and MgO DOSs below their respective insulating band gaps (from Ref. [112]).

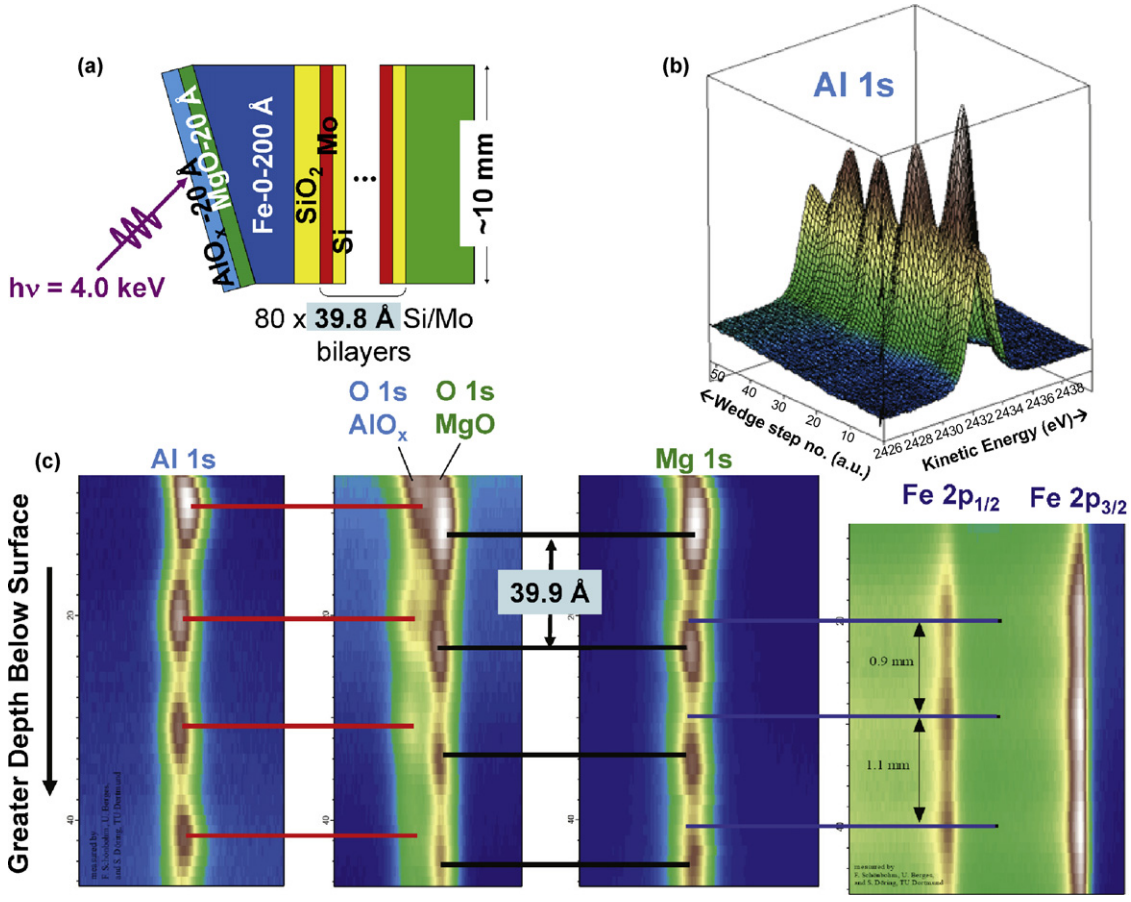

Fig. 22. Hard X-ray standing wave wedge data for the MgO/Fe magnetic tunnel junction system, with excitation at 4000 eV. (a) The sample configuration. (b) Variation of the Al 1s intensity as the X-ray spot is scanned along the wedge. (c) Variation of various core-level intensities as the X-ray spot is scanned along the wedge. The swedge geometry again assures that adjacent maxima for a given level are spaced apart in height by precisely the SW period, here 39.8 Å (from Ref. [114]).

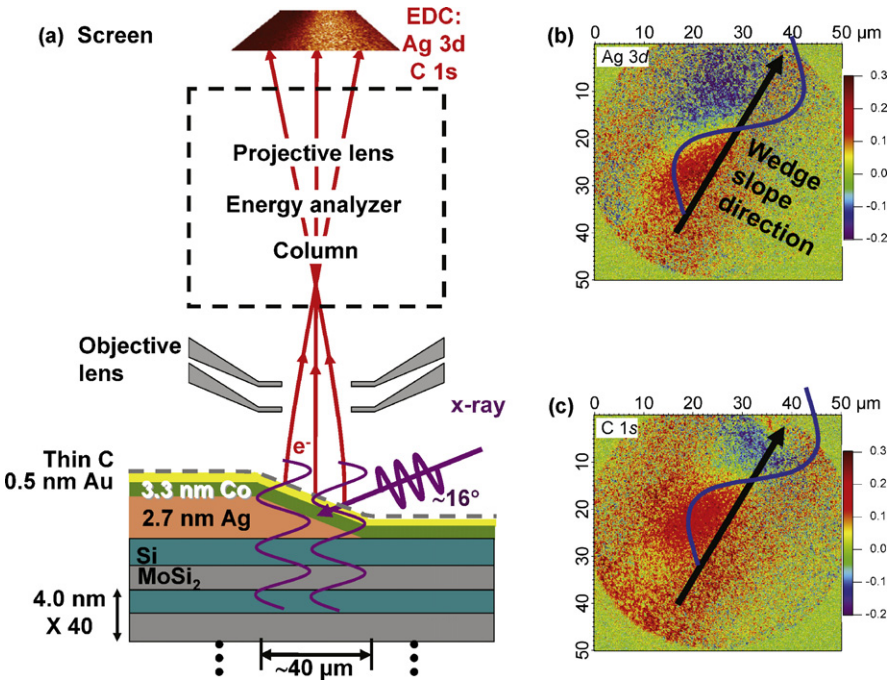

Fig. 23. (a) A schematic view of the first implementation of the standing wave/wedge (swedge) method in a photoelectron microscope, for the specific case of a Ag wedge below Co and Au layers, and with a C contaminant layer on top. (b) and (c) The difference of two PEEM images taken well above (602 eV) and on the Bragg reflection condition (590 eV), using the Ag 3d and C 1s intensities to produce the images in (b) and (c), respectively. The 590 eV photon energy is closest to the Bragg condition for the multilayer mirror. The difference images show ~20% modulation of photoemission intensity introduced by the SW. Note the phase shift between the two images due to the different vertical positions of Ag and C with respect to the multilayer mirror which generates the standing wave (from Ref. [117]).

[118]. In more recent experiments, simply scanning photon energy over the Bragg condition for a multilayer-based sample with no wedge present has also been found to yield a similar type of depth information [119].

Thus, the use of standing wave excitation in photoelectron microscopy should provide information on the third vertical dimension in images that have hitherto only been indirectly inferable from subtleties in core photoelectron or X-ray absorption spectra.

9.6. *Additional X-ray optical effects in XPS*

As an illustration of the rich variety of X-ray optical effects that can occur with hard X-ray excitation on a multilayer structure when the incidence angle is varied, Fig. 24 shows purely theoretical X-ray optical calculations for 6 keV X-rays incident on a model multilayer structure of relevance to exchange-bias, as shown in Fig. 24(a): a GaAs/AlAs multilayer with period 44.9 Å, on which is placed 200 Å of MgF_2 (modelling a seed layer for epitaxial growth), followed by 100 Å of FeF_2 (an antiferromagnet), 40 Å of Co (a ferromagnet), a 10 Å protective cap of Al, and finally a thin layer of oxygen contaminant to simulate the surface oxidation of Al [120]. In Fig. 24(b) and the blowup from it in Fig. 24(c), photoelectron intensities arising from all layers within the sample are plotted as a function of incidence angle, with various effects being seen: (1) rocking curves at the Bragg angle of 1.39°, (2) small closely spaced oscillations on either side of the Bragg rocking curve that are due to Kiessig fringes resulting from interference between waves reflecting from the top layer of the multilayer and from the bottom interface of it, and associated with the distance $D_{ML} = 60 \times 44.9\,Å + 40\,Å = 2694\,Å$, and (3) longer wavelength Kiessig fringes associated with the $MgF_2 + FeF_2 + Co$ layers, with an effective $D = 340$ Å. These fringes are evident in recent experimental rocking curve data using both soft X-ray (cf. Fig. 17(b)) and hard X-ray excitation, and can be used to check the thickness of the multilayer and the wedge + overlying layers, for example. As the onset of total reflection is approached at low incidence angles of ca. 0.5°, the photoelectron intensities rise due to a concentration of electric field near the surface, an effect first observed and explained by Henke [30a]. Finally, when total reflection is reached, they all fall to zero, but at different rates due to different onset angles of total internal reflection at buried interfaces that turn off the emission below them. Of course, this is also the regime in which total reflection XPS (TRXPS, GIXPS) is already being exploited [30], as overviewed by Kawai in this issue. It is now interesting to look at the precise form of the electric field squared as a function of depth at a few special points in angle. For angle "1" of 0.3° in the total reflection regime, as shown in (d), there is little penetration below the Co layer, and intensities would be sensitive to the Co/FeF_2 interface. For angle "2" of 0.375°, as shown in (e) the electric field exhibits a "waveguide" effect due to multiple scattering of the radiation at the top and bottom surfaces of the relatively low optical density MgF_2, and the field strength is much greater in this layer, with a resulting dramatic spike in the intensity from it in panel (b). The angle 0.375° is furthermore very close to the angle 0.298° which one gets for first-order multiple internal reflection inside the 200 Å-thick MgF_2 layer. Combined with the observed onset of total reflection at the top GaAs layer seen in Fig. 24(b) at very nearly the same angle, this explains semi-quantitatively the strong waveguide effect observed. Such waveguide effects have in fact been observed in hard X-ray fluorescence experiments previously [121]. For the last special case of the Bragg angle, as shown in Fig. 24(f), a strong standing wave with the period of the multilayer is created, with this being the topic of most of the prior discussion in this section. Although these results are based on theory only, they are expected to be an accurate representation of experiment in the absence of any threshold absorption resonance excitations. Thus, interesting variations in the field form with incidence angle such as those seen in Fig. 24 should also be very useful in future and soft and hard X-ray experiments on multilayer structures, permitting one to tailor the radiation profile so as to emphasize different por-

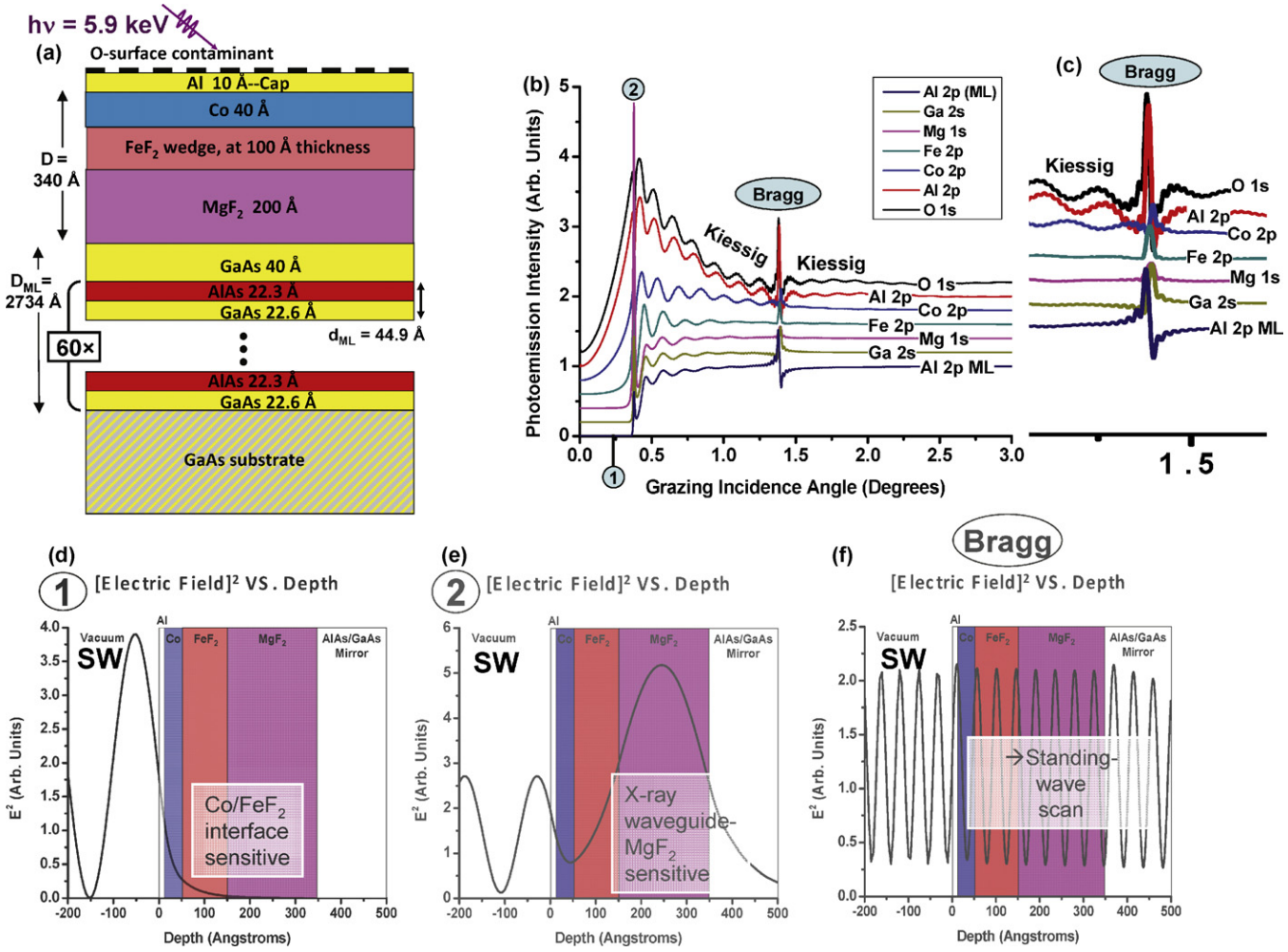

Fig. 24. Theoretical X-ray optical calculations using a program due to Yang [107] for the angular dependence of photoelectron intensities and electric field for 5.9 keV photons incident on a hypothetical sample involving exchange-bias between Co and FeF_2, and grown on a GaAs/AlAs multilayer of 44.9 Å period. (a) The sample configuration. (b) Photoelectron intensities from core levels in every layer of the sample, normalized to unity at 3.0° incidence angle, and shifted by 0.2 with respect to one another to avoid confusing overlap. (c) A blowup of the region around first-order Bragg reflection from the multilayer, indicating more clearly the two types of Kiessig fringes expected from such a structure, and associated with the distances D_{ML} and D in (a). (d) The depth dependence of the electric field squared for an incidence angle for which total reflection from the Co/FeF_2 interface has just turned on. (e) As (d), but for an incidence angle in which an X-ray waveguide effect has greatly enhanced the field inside the MgF_2 layer. (f) As (d), but for incidence at the first-order Bragg angle of the multilayer. Standing waves (SW) are created in all cases in the vacuum above the sample as well (from Ref. [120]).

tions of the sample. Carrying out such measurements does require a very narrow angular divergence of the incident beam, however, and thus such experiments are best done with synchrotron radiation.

10. Angle-resolved photoemission in the soft and hard X-ray regime

10.1. The basic ARPES measurement in the UPS limit

At lower energies of excitation, especially below roughly 100 eV, photoemission spectra are routinely used to map the band structure of solids and surfaces, and this is one of the most powerful applications of photoelectron spectroscopy. This ability is due to the fact that the excitation can be considered to be dominated by so-called "direct transitions" (DTs) in which an occupied initial one-electron Bloch-wave state $\varphi(E_i, \vec{k}_i)$ at energy E_i and wave vector $\vec{k}_i$ can in the dipole limit only make a transition to a final state with wave vector $\vec{k}_f = \vec{k}_i + \vec{g}_n$, where $\vec{g}_n$ is some reciprocal lattice vector associated with the crystal structure under investigation, and n represents a general set of $h\,k\,\ell$ indices. The relevant vector conservation equation is illustrated for the examples of soft X-ray and hard X-ray excitation from tungsten in Fig. 25. This figure also indicates that, as the photon energy is increased, one can no longer neglect the momentum of the photon $\vec{k}_{h\nu}$ in conserving wave vector, one manifestation of non-dipole effects in the excitation [25,26,122]. Determining $\vec{k}_f$ inside the surface from a measurement of $\vec{K}_f$ outside the surface (which will be slightly different from $\vec{k}_f$ inside due to crossing the inner potential V_0 at the surface) and then the set of $\vec{g}_n$ vectors which project $\vec{k}_f$ back into the reduced Brillouin zone (BZ) in which the band structure is usually described thus permits directly measuring $E_{binding}(\vec{k}_i) = E_i(\vec{k}_i)$, the band structure, or if final-state screening and many-electron excitations are taken into account, more properly the spectral function as calculated from some sort of many-electron theory [6]. A convenient expression of wave-vector conservation is thus:

$$\vec{k}_i = \vec{k}_f - \vec{k}_{h\nu} - \vec{g}_n. \tag{6}$$

If the final photoelectron state is high enough in energy, it can be approximated as a free-electron, with $E_f(\vec{k}_f) \approx p_f^2/2m_e = \hbar^2 k_f^2/2m_e$, where m_e is the electron mass.

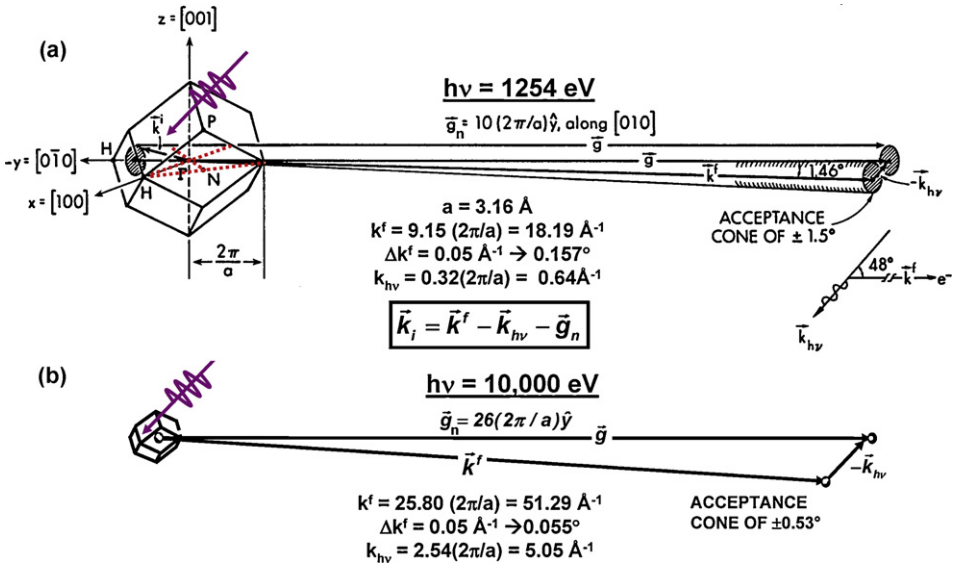

Fig. 25. Illustration of $\vec{k}$ conservation in valence photoemission from W at two different photon energies: (a) 1253.6 eV, a typical soft X-ray energy also available with laboratory sources, and (b) 10,000 eV, a hard X-ray energy that is of interest for the future. Note the basic wave-vector conservation law, which must include the photon wave vector for energies above ~100 eV (from Refs. [113,122]).

10.2. Hard X-ray angle-resolved photoemission (HARPES): densities of states and band mapping

We have already noted that the combined effects of phonon excitations during photoemission and angular averaging in the spectrometer often lead in measurements at 1 keV or higher excitation energies spectra that represent a matrix-element weighted density of states (DOS), the XPS limit (cf. Fig. 9). A measure of how completely phonon effects have contributed to this DOS limit is a temperature-dependent Debye–Waller factor ($W(T)$) calculated for the relevant $\vec{g}_n$, which roughly represents the fraction of direct transitions remaining [122]. This factor can be calculated from $W(T) \approx \exp[-g^2 < u^2(T) >]$, with $< u^2(T) >$ the one-dimensional mean-squared vibrational displacement at temperature T. To illustrate the XPS limit for very small $W(T)$, Fig. 26 shows two comparisons of experiment and theoretical densities of states for Au with excitation energies of 1487 eV (Al Kα) [123] and 5.5 keV in the hard X-ray regime [124]. The relevant $W(T)$ values are ~0.04 for 1487 eV excitation and $\sim 5 \times 10^{-6}$ for 5.5 keV, so one expects to be in the XPS limit in both cases. In both panels, the density of states as calculated from local-density theory is compared to experiment [125]. Although there are subtle differences between experiment and theory, probably due to matrix-element effects, it is clear that high-energy photoemission provides a rather direct measure of the DOS.

It is also important to note that, since the XPS limit in its simplest interpretation measures a matrix-element weighted DOS, the two panels in Fig. 26, or indeed in any comparison of spectra with soft X-ray and hard X-ray excitation, will represent different weightings of the atomic orbital character of the valence bands. More quantitatively for the case of Au, the relevant subshell photoelectric cross-section ratios between the two photon energies are: Au6s/Au5d = 0.012 at 1.5 keV and 0.028 at 6 keV [19], with the relative influence of Au 6s thus expected to be about 2.3 times higher at 6 keV. This is in fact seen in Fig. 26, via the enhanced relative intensity of the 6s-dominated region over about 0–1.5 eV binding energy, as compared to the 5d-dominated features over 2–8 eV binding energy. More generally, subshells with lower angular momentum quantum number ℓ are favored at higher energy, due to the increased number of oscillations in their radial wave functions, and thus better non-zero overlap with the strongly oscillatory photoelectron radial wave function in the calculation of a matrix element.

Beyond densities of states however, it is also interesting to assess whether more bulk-sensitive band mapping is possible by using energies beyond the usual ARPES range up to ~150 eV, and going up into the keV, or even multi-keV regime. Several papers exploiting this in the 500–1000 eV range have in fact already appeared [66,126–130]. As an example of the competing physics involved in doing this, we consider an intermediate case for which both band mapping and phonon smearing are involved: photoemission from tungsten with ~1 keV excitation. Fig. 27(a)–(d) shows a set of angle-resolved data from $W(1\,1\,0)$ obtained in near-normal emission with an intermediate energy of 870 eV, and at four different temperatures, which permits assessing the influence of phonons in a more quantitative way [66]. The four experimental panels all clearly show band-mapping features, and in fact can be shown by simple free-electron final-state calculations to sample along the Γ-to-N direction in the BZ, one of the directions highlighted in Fig. 25(a). It is also clear that raising the temperature stepwise from 300 to 780 K, or from 0.75 times the tungsten Debye temperature to 1.95 times that temperature involves a smearing of those features and a significant gain of intensity in other parts of the angle-resolved data. Also shown for comparison to experiment in Fig. 27(e)–(h) are the results of one-step photoemission calculations that go beyond the three-step model in many respects and include matrix-elements effects [131], a level of theory also discussed by Fujikawa in this issue. These calculations agree very well with the positions and intensities of all features seen in experiment, with some special points labelled 1, 2, ... 6 in experiment, and 1′, 2′ ... 6′ in theory. However, these calculations do not at their present level correctly predict the smearing of features at higher temperatures due to phonons [66]. Further work is clearly needed in the theory of X-ray excited ARPES so as to adequately describe these phonon effects; this would permit more quantitatively using such data to study bulk electronic structures in a variety of materials.

As a further example of such higher-energy ARPES, Fig. 28(a)–(b) compares experiment and one-step theory, again for $W(1\,1\,0)$, but this time with excitation at a higher energy using non-monochromatized Mg Kα radiation at 1253.6 eV and cooling to liquid nitrogen temperature to reduce the phonon effects [132].

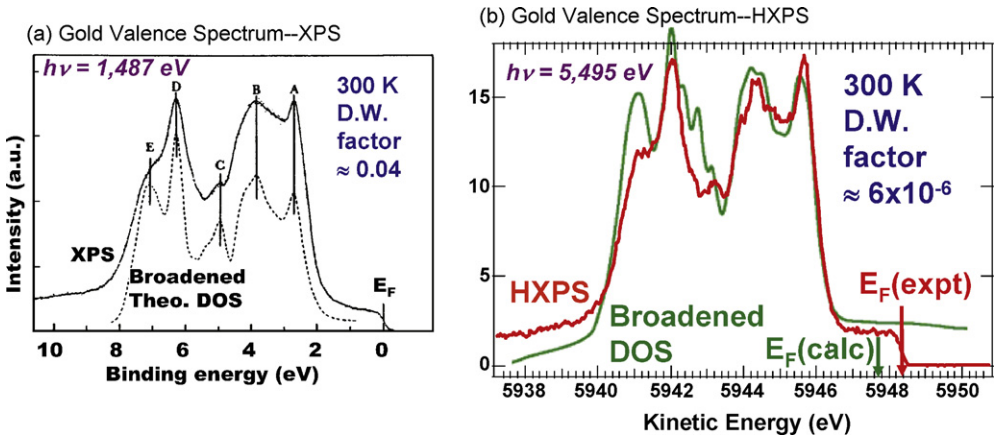

Fig. 26. Valence photoelectron spectra from the noble metal Au in the XPS or density of states (DOS) limit. In (a) and (b), Au spectra with 1.5 keV (from Ref. [123]) and 5.5 keV (from Ref. [124]) excitation, respectively, are shown. In both cases, the experimental results are compared with theoretical densities of states based on local-density theory; in (b) these are from Ref. [125].

In the measurements, the sample angle θ was varied in steps that were a little smaller than the ~20° window spanned by the detector in $\vec{k}$ (cf. Fig. 1), such that the detector images could be tiled together in an overlapping way over a range of about 50°. The agreement with one-step theory here is again excellent, both as to the positions and the relative intensities of the excitation from different bands. There is some disagreement in angular positions for the largest positive angles relative to the [110] surface normal, but this is probably due a slight misalignment of the crystal relative to that assumed in the calculations. Finally, in Fig. 28(c), the actual $\vec{k}_f$ excursion in this experiment is shown, as calculated based on simple free-electron final states. Over the angle range of the experiment, the reduced Brillouin zone is spanned about 5 times via five different reciprocal lattice vectors $\vec{g}_n$, $n = 1, 2, \ldots 5$, starting out for small angles along the face of the Brillouin zone along H-to-N-to-H and finally moving to scan more along H-to-Γ-to-H, as indicated by two additional dashed lines in the Brillouin zone in Fig. 25(a). These results make it clear that one can do three-dimensional band mapping in this way, and with greater bulk sensitivity. Varying photon energy for a fixed emission-angle

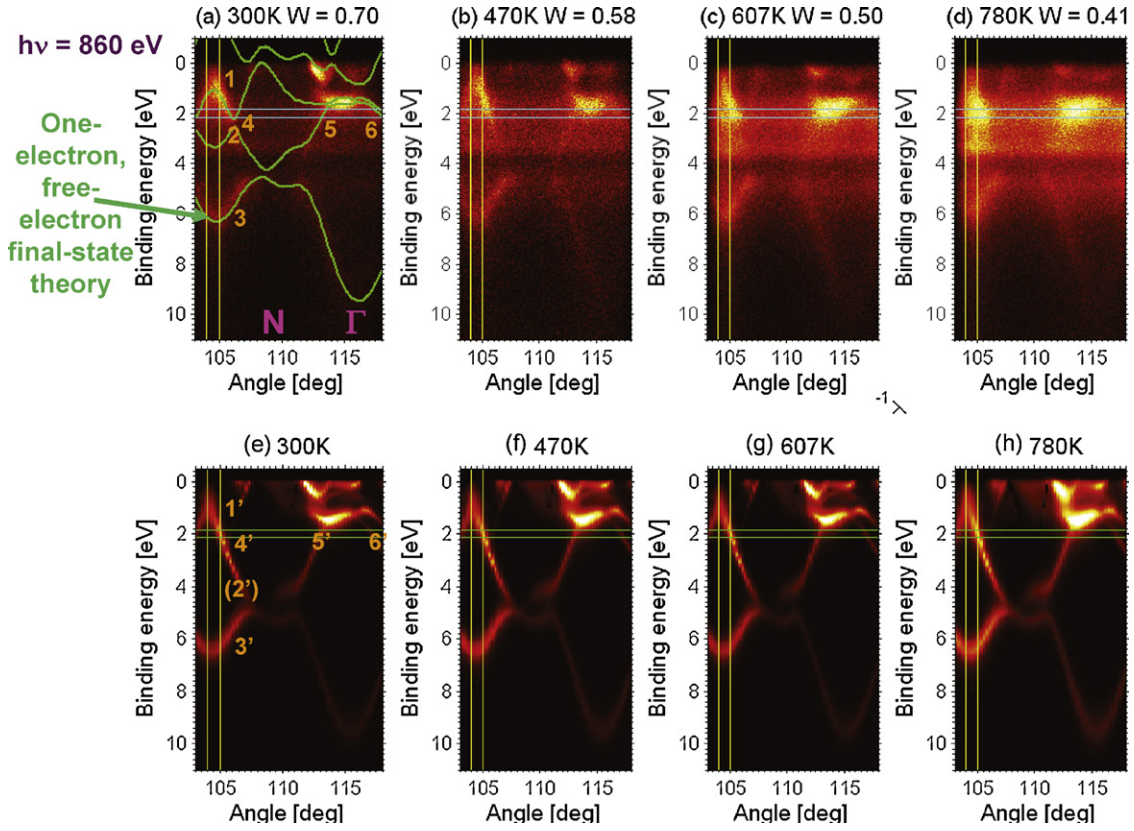

Fig. 27. Temperature-dependent angle-resolved photoemission data from $W(1\,1\,0)$ at an excitation energy of 860 eV. (a)–(d) Experimental energy-vs-angle (energy-vs-$\vec{k}$) plots at four temperatures, with phonon-induced smearing of features evident as T is raised. From left to right in each, the N-to-Γ line in the Brillouin zone (cf. Fig. 25(a)) is approximately sampled. In (a) the results of a simple free-electron final-state estimate of the spectra with no matrix elements included are shown as the green curves. (e)–(h) Theoretical calculations of these results based on a one-step model including matrix elements, and allowing for phonon effects via the approximation of complex phase shifts (from Ref. [66]).

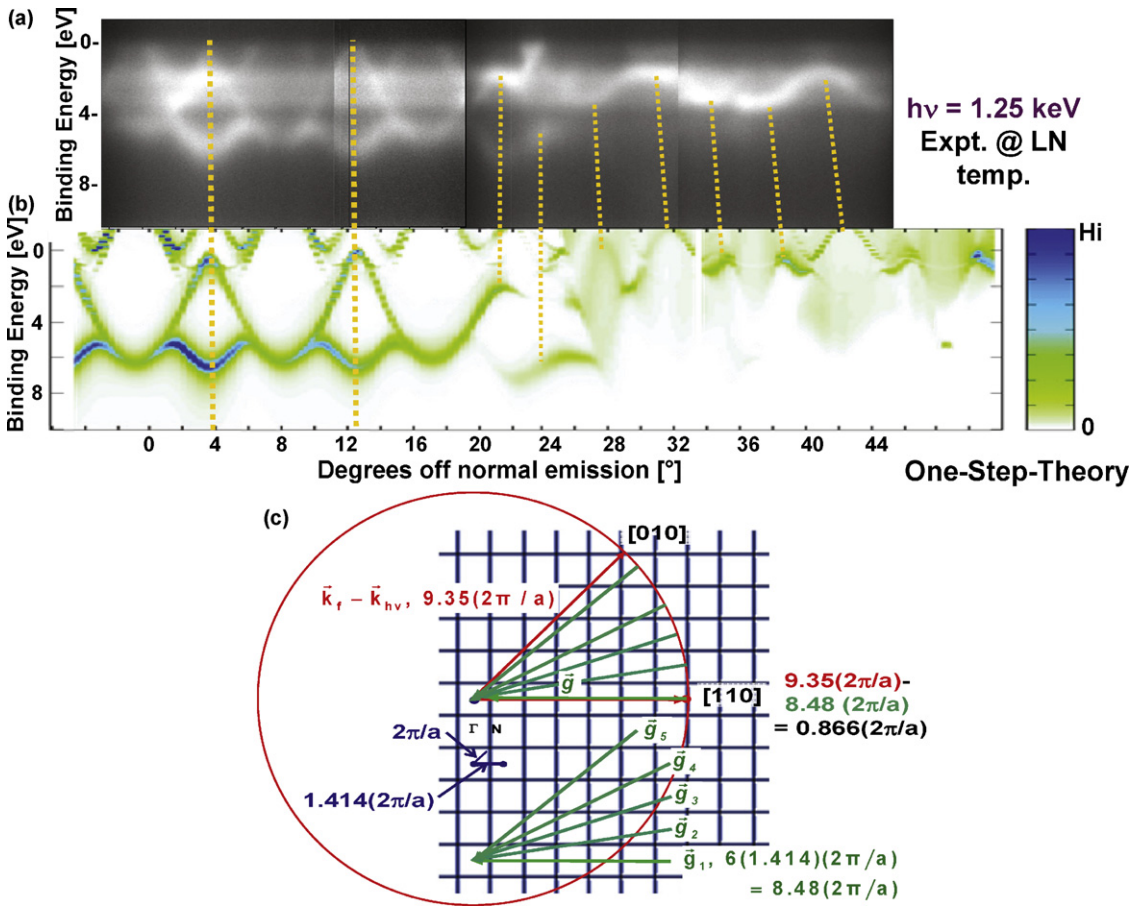

Fig. 28. Angle-resolved photoemission data obtained from $W(1\,1\,0)$ with non-monochromatized Mg Kα radiation and at 77 K. The experimental data in (a) were obtained by rotating the sample in θ and tiling several $E - \vec{k}$ images in the detector (cf. Fig. 1(c)). The one-step theory with matrix elements included in (b) is based on the same method used in Fig. 27 [66,131]. There is in general excellent agreement as to both positions and relative intensities, with the dashed lines being guides to the eye in comparing experiment and theory. Some angular shifts between them for larger angles are probably due to a slight misalignment of the crystal. (c) The region in $\vec{k}$-space spanned by these measurements. By thus scanning the emission direction over a range of about −5° to +45° relative to the [110] surface normal, the $\vec{k}$-point sampling in the Brillouin zone involves five different reciprocal lattice vectors $\vec{g}_n$ and thus five different sampling arcs, as indicated by 1, . . . 5 in the reciprocal space drawing (From Ref. [132]).

range is another method for doing three-dimensional band mapping.

As a final example here, we show in Fig. 29 truly hard X-ray ARPES from $W(1\,1\,0)$ as measured at two temperatures, 300 and 30 K, and excited by 5.9 keV photons obtained from the SPring8 synchrotron radiation source [133]. In the detector images shown, 39–40 channels equal 1°, so each image spans about 12°. Fig. 29(a) shows a detector image at 300K, for which $W \approx 0.09$, a situation expected to yield the XPS limit. Indeed, no dispersive features are seen, and the EDC at any angle is found to closely resemble the W DOS, with the three most prominent peaks indicated by arrows in the figure. Fig. 29(b) shows results after cooling to 30K, for which $W \approx 0.45$, and approximately half the intensity is thus expected to be involved with direct transitions. For this case, dispersive features clearly appear, although they are superposed with DOS features. However, in both panels (a) and (b), the DOS-like intensity exhibits modulations with angle that can be as much as 30%. These are simply hard X-ray photoelectron diffraction effects, as has been seen before with soft X-ray excitation of valence bands for cases in the XPS limit [134]. Thus, both dispersing band effects and XPD effects can be seen in the same dataset, with relative amounts depending on temperature and photon energy.

The raw low-temperature image in Fig. 29(b) has then been corrected with a two-step procedure that involves dividing by the detector window average over energy (to approximately correct for XPD effects) and by the window average over angle (to approximately correct for DOS effects) [135], with the final result being shown in Fig. 29(c). The dispersive features are much clearer in this corrected image, and suggest this procedure as a general method that should be useful for any systems for which W is less than approximately 0.5. Fig. 29(d) now presents one-step photoemission calculations with matrix-element effects included, and the agreement is very good. Finally, Fig. 29(e) shows the region in $\vec{k}$-space involved in these measurements. The image is expected to span the Γ-to-N-to-Γ direction, as indicated also in Fig. 29(c). Fig. 29(e) also shows that the effect of the photon momentum for this case is by chance to shift the image in $\vec{k}$-space by very nearly the Γ-N-Γ distance (4.35° compared to 4.21°, respectively), so the forward scattering peak along [110] in Fig. 29(a) lines up almost exactly with the Γ position in the dispersing bands. In general, this would not be true.

The results of Figs. 27–29, together with more recent results for GaAs(1 0 0) at 3.2 keV [133], thus clearly indicate that it should be possible to carry out more bulk-sensitive electronic structure studies at much higher photon energies than have been typically employed in the past. Estimates for a number of elements based on Debye–Waller factors in fact indicate that, with cryogenic cooling to suppress phonon effects, it should be possible to carry out more bulk-sensitive band mapping for many materials at up to a few keV, if not higher [66,136]. For example, Fig. 30 shows isocontour plots for $W = 0.5$, corresponding to an estimated 50% of direct transitions, at a sample temperature of 20 K that can be reached by many cryo-

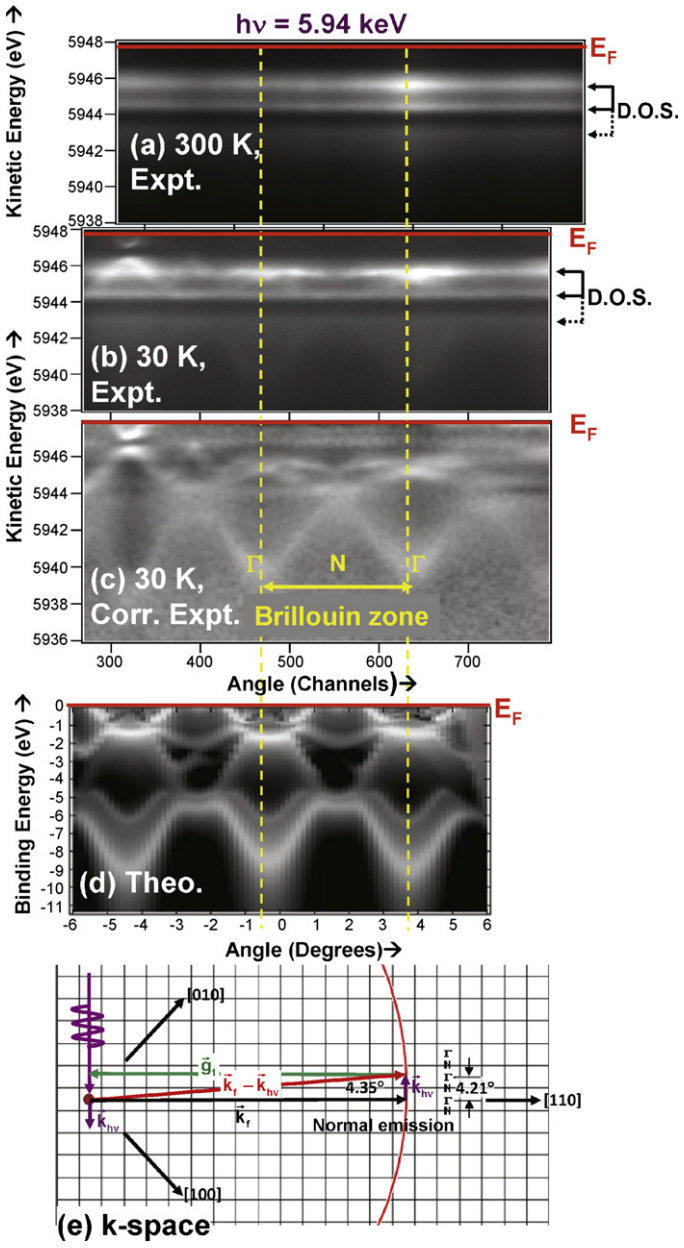

Fig. 29. The first hard X-ray angle-resolved photoemission data, for the specific case of $W(1\,1\,0)$ excited with 5.94 keV excitation. (a) Detector image as recorded at 300 K, very close to the XPS limit, and showing XPD modulation of the density of states (DOS), whose three primary peaks are indicated by arrows. (b) Detector image as recorded at 30 K, exhibiting both XPD-DOS and dispersive band features. (c) Corrected image from (b) after division by both the energy average and the angular average to enhance dispersive band features [135]. (d) One-step photoemission theory including matrix-element effects. (e) Free-electron final-state picture of the region sampled in $\vec{k}$-space (from Ref. [133]).

genic sample holders, as a function of photon energy and the two sample-related parameters Debye temperature and atomic mass. This plot can be used for any material for which the Debye temperature and the effective atomic mass are known. Also indicated by points are the actual values for about 34 elements. From this data, it is clear that band mapping should be possible in the 1–2 keV range, with the results for graphite also suggesting that layered materials may exhibit very different degrees of phonon involvement in-plane and perpendicular-to-plane. In addition, for GaAs, bands have been resolved with a lower W value of 0.35 [133], so the estimates in this figure are if anything conservative, with higher energies in the few keV range likely being usable for many systems. It is also expected that better procedures for correcting for the photon-associated DOS-like features will be developed, along with better microscopic theoretical treatments of such phonon effects [66], thus extending the energy range even further.

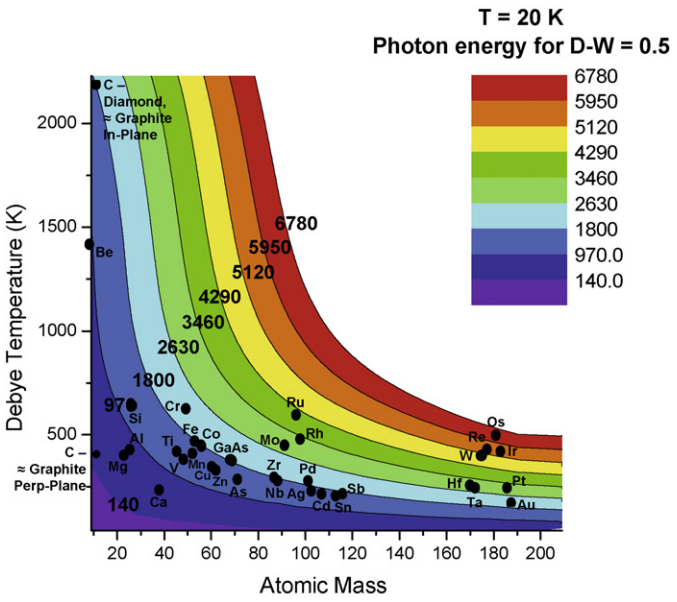

Fig. 30. Theoretical calculations of Debye–Waller factors W for angle-resolved photoemission, showing isocontours for $W = 0.5$ at a temperature of 20 K, as a function of Debye temperature, the atomic mass, and the photon energy. Results are shown for 34 elements, including three entries for carbon: diamond, graphite-in plane, and graphite-perpendicular-to-plane. The Debye temperatures used are for 300 K, with the exception of graphite (from Ref. [136]).

10.3. Nanometer-scale angle-resolved photoemission

As Fig. 1(g) indicates, other dimensions of photoemission involve adding *spatial resolution in the lateral dimensions x and y*, with one method for achieving additional resolution in the *vertical z dimension* via standing waves already being discussed in a prior section. Photoelectron microscopy or more generally "spectromicroscopy" is reviewed in detail by Margaritondo and by Oelsner in this issue, and in other recent overview articles [35–37]. Thus, we will here only specifically consider one future direction involving focussing the radiation to a small spot so as to do what has been termed "nano-ARPES" [135].

In Fig. 31(a), the basic idea of the experiment is presented [135]. A zone-plate lens is used to focus a soft X-ray synchrotron radiation beam down to a spot of the order of 100 nm. A spectrometer like that shown in Fig. 1 is then used to measure spectra from various regions of the sample by raster-scanning the sample in front of the beam in x and y. Both core and valence-level spectra can be accumulated in this way. Fig. 31(b) shows a micrograph from a cleaved sample of highly oriented pyrolytic graphite (HOPG) in which the intensity in valence-band spectra has been used as a contrast mechanism. Looking in more detail at the ARPES spectrum excited with 180 eV photons from the specific 300 nm region indicated reveals in Fig. 31(c) the band structure of the HOPG in that region. It is furthermore observed that the contrast comes about due to a slight tilting of different polycrystalline domains, with the brighter (yellow) regions corresponding to the so-called π-band of graphite being oriented towards the detector. Thus, one can look forward to taking advantage of much of what was discussed above with lateral spatial resolutions that should eventually reach 20 nm or better. In addition, spectromicroscopes making use of sophisticated electron optical elements promise to permit photoemission measurements below 10 nm, and perhaps at a few nm [137,138],

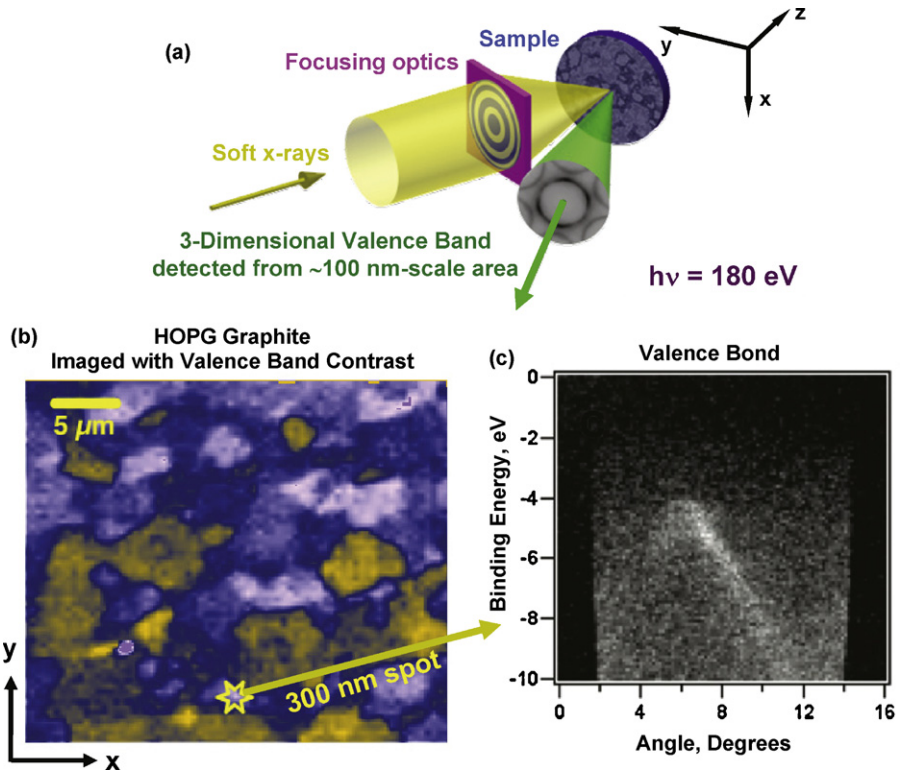

Fig. 31. Some first experimental results for spatial- and angle-resolved photoemission: nano-ARPES. (a) The basic experimental geometry, with a zone-plate used to focus the radiation into a small spot. (b) An image obtained by scanning the sample in front of the spot in *x* and *y*, with contrast provided by the intensity of the valence-band spectra, as excited by 180 eV radiation. (c) Angle-resolved photoemission results obtained from a 300 nm region indicated in (b) (from Ref. [135]).

although perhaps not with the energy and angular resolution of the zone-plate scheme in Fig. 31. Going to higher photon energies as discussed in the prior section should also yield more bulk-sensitive electronic structure, but with two-dimensional imaging.

10.4. Bonding interactions and band structures in core levels

As a final aspect of ARPES, we should note an only very recently discovered effect, the observation of weak bonding interactions in deep core levels of solids, and resultant "band structures" [139]. In particular, combined C 1s XPD and C 1s ARPES measurements on graphene show that, although C 1s is nominally a core level that is not involved in chemical bonding, there are interatomic interactions of sufficient strength to mix adjacent orbitals in bonding and anti-bonding combinations, thus forming long-range Bloch functions that exhibit dispersion with wave vector [139]. The magnitudes of these dispersions are small, at 60 meV overall, but nonetheless observable via high-resolution measurements at photon energies of 350–700 eV. Such effects are in fact not surprising, as they are the solid-state analogues of effects that have been known in simple molecules such as acetylene (H–C–C–H) [140] and N_2 for some time [141]. This phenomenon thus represents another example of the fruitful cross-fertilization that often takes place between atomic and molecular physics and condensed matter physics.

It is thus expected that such effects will be seen in high-resolution measurements of core levels in many other systems, and that they could in fact influence the overall linewidths in core spectra at the 50–100 meV level.

11. X-ray photoemission at high ambient pressure

I have previously mentioned XPS measurements at higher pressures in the multi-torr regime, but it is worthwhile here to consider a few illustrative examples of recent results.

As one aspect of XPS at higher pressures, we first consider the monitoring of surface chemical reactions in real time. Beginning with some first exploratory studies by Nilsson et al. in Uppsala [142] and by Grunze and co-workers [143], work in several laboratories has by now extended such reaction kinetics studies with synchrotron radiation excitation to faster timescales and more complex chemical reactions [144,145], as well as to higher effective ambient pressures [82,83,146], thus permitting studies of such systems as aqueous surfaces [146] and solutions [147] and catalytic reactions [148]. This represents yet another exciting and rapidly developing area for future studies with X-ray photoelectron spectroscopy.

As a technologically relevant example of these types of time-resolved reaction studies, Fig. 32(a) shows a high-resolution spectrum of an oxidized Si(0 0 1) surface, with the well-known resolution of at least five distinct chemical states from the element to that of SiO_2 [149]. Such spectra have previously been used to study the kinetics of oxidation of Si at pressures of about 10^{-6} Torr, with resolution in time of all of the oxidation states. As a more recent development, Fig. 32(b) shows a first high-pressure XPS system in which the sample could be separated from the exciting synchrotron radiation beam by a thin Al (or SiN) window and from the analysis section of the electron spectrometer by an electron lens with two stages of differential pumping [82]. This configuration permits having the sample region at up to a few torr in pressure during measurements. In this way, surface reactions can be studied at pressures that in some cases are much closer to the actual conditions of industrial processes or systems of relevance to environmental science, thus bridging what has been called the "pressure gap" between ultrahigh vacuum surface science research and real-world reaction conditions, and leading to the term "ambient pressure photoemission spectroscopy (APPS) for this technique [83]. As an example of the use of such a system, Fig. 32(c) shows several spectra from a very recent Si oxidation study at 450 C and 1 Torr which is of relevance

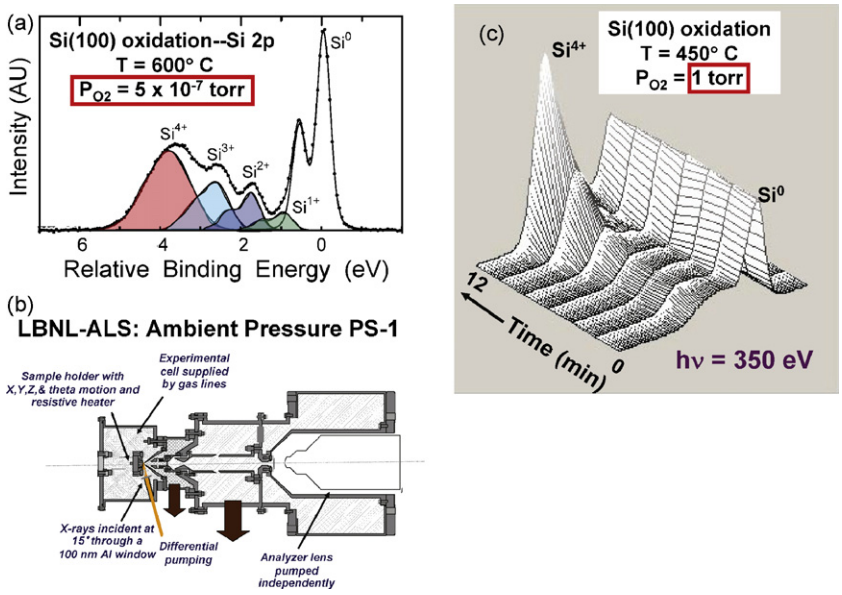

Fig. 32. (a) High-resolution Si 2p spectrum from a Si(0 0 1) surface that has been oxidized at 600 °C and an ambient pressure of 5×10^{-7} Torr (from Ref. [149]) (b) A spectrometer configuration in which the sample region is isolated from the radiation source by a thin window and from the spectrometer by differential pumping so as to permit ambient pressures up to 5–10 Torr (from Ref. [82]). (c) A series of Si 2p spectra taken at about 1 min intervals during the oxidation of Si(0 0 1) at 450 °C and an ambient pressure of 1 Torr (from Ref. [150]).

to the processing conditions used in the semiconductor industry [150]. Spectra here were recorded every 8 s, but are finally shown as binned in 1-min intervals for this plot. The SiO_2 thickness range covered is 0–25 Å. More detailed analysis of this data as shown in Fig. 33 indicates a clear division of the reaction rates into an initial rapid regime and a much slower quasi-saturated regime, with a break point between them that occurs when the SiO_2 is about 5–15 Å thick, depending on the ambient pressure. Current models for the reaction kinetics of this process do not describe this regime of thicknesses that is now crucially important in devices [150].

In another illustrative example of the power of ambient pressure XPS, it has recently been used to study the distribution of ions at the surface of an aqueous solution by measuring the intensity ratios of alkali and halide ions as a function of pressure (by going up to the point of deliquescence on a solid alkali halide surface) and photon energy (by varying the degree of surface sensitivity) [147]. Some of these results are summarized in Fig. 34. For KBr, with excitation at a more-surface-sensitive energy of 200 eV, Fig. 34(a) shows that

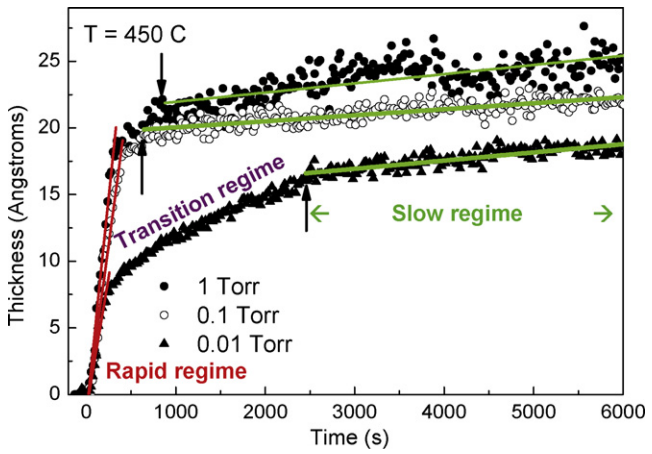

Fig. 33. Application of ambient pressure XPS to the time-dependent growth of SiO_2 on Si(0 0 1) at 450 °C and various pressures, as derived from the relative intensities of the Si^{4+} and Si^{0} peaks in spectra such as those in Fig. 32(c) (from Ref. [150])

the Br/K intensity ratio is constant until the deliquescence point is reached, at which it abruptly jumps by a factor of two due to an enhancement of the Br concentration at the surface. In Fig. 34(b), the effect of varying photon energy on this ratio at deliquescence is shown, and these results verify that, for either KBr or KI, the halide ion tends to segregate to a liquid surface, with the effect being more pronounced for the larger iodide ion. These results are also consistent with the expectations of molecular dynamics calculations. Such studies of liquid surfaces, either in the static high-pressure ambient mode described here [83], or via photoemission from a liquid jet as reviewed elsewhere [9], open the way to many studies of relevance to environmental and life sciences.

As one additional aspect of ambient pressure XPS studies, one can also look forward to being able to resolve band structures and molecular levels in the near-surface region as a function of time and gas exposure. For example, Fig. 35 shows a detector image like those in Fig. 1(c), and 27–30, but for an HOPG graphite surface in the presence of 0.2 Torr of CO at a photon energy of 120 eV [151]. The dispersing band states of the graphite are clearly seen as curved intensity profiles, together with the non-dispersing localized molecular states in the gas near the surface, and perhaps also adsorbed on the surface, which appear as flat lines. Thus, following the electronic structure of both substrate and adsorbate in detail during a surface chemical reaction should be possible. It is also clear that, if a core-level intensity is monitored in a situation such as that in Fig. 35, diffraction-produced modulations of intensity will be observable in the detector image; these would provide additional atomic structure information from XPD to the ambient pressure photoemission experiment, and represent another obvious direction for future experiments.

Looking ahead concerning ambient pressure XPS, we can expect that much higher pressures into the 15–20 Torr regime, shorter timescales in the millisecond range, and significantly better energy resolutions than those in Figs. 32(c) and 34(a) should be possible with a combination of better differential pumping, higher throughput spectrometers, brighter radiation sources, and more efficient multichannel detectors for photoelectrons that are under development [43]. Reaching 18 Torr is a particularly important goal, as this is the vapor pressure of water at room temperature. Being

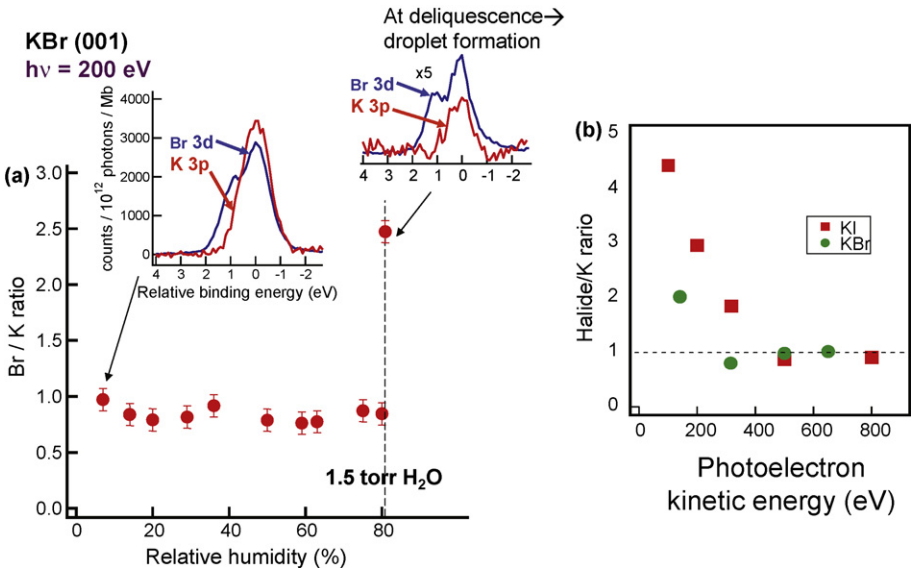

Fig. 34. Application of ambient pressure XPS to the concentration profiles at the surfaces of ionic solutions, in particular aqueous KBr and KI. (a) The variation of the normalized Br/K ratio obtained from a surface of KBr excited at 200 eV photon energy as a function of ambient water humidity, which varies from zero to the deliquescence point at which an aqueous solution forms. The insets show actual XPS spectra at the two end points. (b) The halide/K ratio for KBr and KI, as a function of the incident photon energy, or equivalently the degree of surface sensitivity (from Ref. [147]).

able to measure at such conditions would open up numerous applications in environmental and biological science. Subsequent generations of differentially pumped spectrometers beyond that in Fig. 32 are already operating and in fact beginning to be commercially available; these include, e.g. up to four stages of differential pumping. Using standing wave excitation in such ambient pressure experiments would also permit more selectively looking at the near-surface region, in particular at the depth profiles of species just below the surface and in the gas phase just above the surface. Finally, since one limit on pressure has to do with attenuation of the photoelectrons by inelastic scattering, using hard X-rays for excitation should permit operating at higher pressures, another advantage of this other new direction in XPS that has been discussed here.

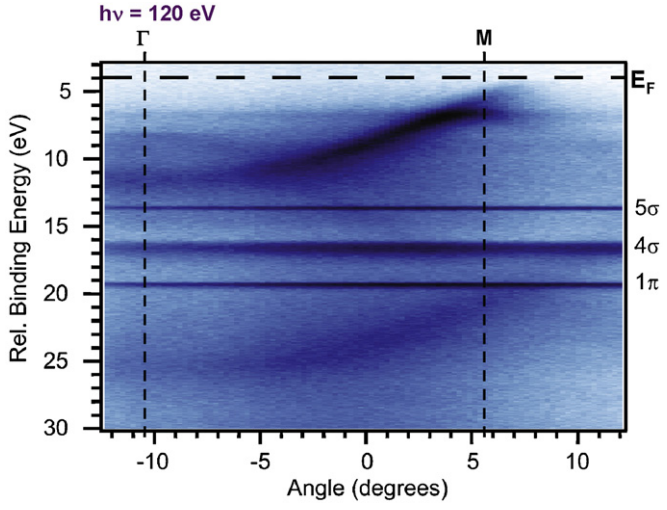

Fig. 35. Observation of bands and molecular levels in an ambient pressure XPS experiment. A sample of HOPG graphite was exposed to 120 eV photons in the presence of 0.2 Torr of CO. The resulting detector image of binding energy vs emission angle (cf. Fig. 1(c)) exhibits both the dispersing bands of graphite near the surface and the non-dispersing states of adsorbed and gas-phase CO (from Ref. [151]).

12. Concluding remarks

In this article, I have attempted to both overview the basic phenomena in XPS, in particular as discussed in more detail in other articles of this issue, and to consider several of its forefront areas for future development and exploitation, from those related to surface and interface analysis, which is in some sense the "bread and butter" application of the technique, to those related to more subtle measurements of surface and bulk electronic structure (densities of states and bands), magnetic properties, and time-resolved processes, including chemical kinetics. There are indeed many exciting new directions for XPS, with the promise that one will be able in the future to carry out experiments in which the properties of a given nanoscale sample are measured as a function of three spatial dimensions (e.g. via some combination of microscopy, variable photon energy into the multi-keV regime, and standing wave excitation), of time (via short-pulse sources and/or next generation ambient pressure systems), and of the electron spin (via next generation detectors). One can say that the "complete photoemission experiment" is within reach. It seems certain that Einstein would be pleased to see what has become of the humble photoelectric effect.

Acknowledgements

The work in the author's group described in this article was supported by the Director, Office of Science, Office of Basic Energy Sciences, Materials Sciences and Engineering Division, of the U.S. Department of Energy under Contract Number DE-AC02-05CH11231. The author also gratefully acknowledges the support of the Helmholtz Foundation, the Humboldt Foundation, and the Jülich Research Center. Various collaborators have also graciously permitted the inclusion of as yet unpublished results. Thanks also goes to A. Gray and two conscientious reviewers for helpful suggestions concerning this manuscript.

References

[1] A. Einstein, Ann. Phys. 17 (1905) 132.
[2] J.G. Jenkin, R.C.G. Leckey, J. Liesegang, J. Electron Spectrosc. Relat. Phenom. 12 (1977) 1;

J.G. Jenkin, R.C.G. Leckey, J. Liesegang, J. Electron Spectrosc. Relat. Phenom. 14 (1978) 477.
[3] K. Siegbahn, C. Nordling, A. Fahlman, K. Hamrin, J. Hedman, R. Nordberg, C. Johansson, T. Bergmark, S.-E. Karlsson, I. Lindgren, B. Lindberg, Atomic, molecular and solid-state structure studied by means of electron spectroscopy, Nova Acta Regiae Soc. Sci. Ups. 20.1-282, Almqvist and Wiksells, 1967.
[4] K. Siegbahn, C. Nordling, G. Johansson, J. Hedman, P.-F. Heden, K. Hamrin, U. Gelius, T. Bergmark, L.O. Werme, R. Manne, Y. Baer, ESCA Applied to Free Molecules, North-Holland, Amsterdam, The Netherlands, 1969, 200 pp.
[5] C.S. Fadley, in: C.R. Brundle, A.D. Baker (Eds.), Electron Spectroscopy: Theory, Techniques, and Applications, vol. II, Academic Press, London, 1978, Chap. 1; available also as a reprint at: http://www.physics.ucdavis.edu/fadleygroup/.
[6] S. Hűfner, Photoelectron Spectroscopy: Principles and Applications, 3rd ed., Springer, Berlin, 2003.
[7] C.S. Fadley, Surf. Interface Anal. 40 (2008) 1579.
[8] C.S. Fadley, Nucl. Inst. Methods A 601 (2009) 8.
[9] (a) H. Siegbahn, S. Svensson, M. Lundholm, J. Electron Spectrosc. Relat. Phenom. 24 (1981) 205;
(b) O.A. Baschenko, F. Bökman, O. Bohman, H. Siegbahn, J. Electron Spectrosc. Relat. Phenom. 62 (1993) 317–334;
(c) B. Winter, E.F. Aziz, U. Hergenhahn, M. Faubel, I.V. Hertel, J. Chem. Phys. 126 (2007) 124504;
(d) B. Winter, Nucl. Inst. Methods A: Accel. Spectrom. 601 (2009) 139.
[10] Y. Takata, Y. Kayanuma, M. Yabashi, K. Tamasaku, Y. Nishino, D. Miwa, Y. Harada, K. Horiba, S. Shin, S. Tanaka, K. Ikenaga, K. Kobayashi, Y. Senba, H. Ohashi, T. Ishikawa, Phys. Rev. B 75 (2007) 233404;
Y. Takata, Y. Kayanuma, S. Oshima, S. Tanaka, M. Yabashi, K. Tamasaku, Y. Nishino, M. Matsunami, R. Eguchi, A. Chainani, M. Oura, T. Takeuchi, Y. Senba, H. Ohashi, S. Shin, T. Ishikawa, Phys. Rev. Lett. 101 (2008) 137601.
[11] S. Suzer (Ed.), J. Electron Spectrosc. Relat. Phenom. 176 (1–3) (2010) (issue dedicated to charging effects in XPS).
[12] X.J. Zhou, B. Wannberg, W.L. Yang, V. Brouet, Z. Sun, J.F. Douglas, D. Dessau, Z. Hussain, Z.-X. Shen, J. Electron Spectrosc. Relat. Phenom. 142 (2005) 27.
[13] A. Pietzsch, A. Föhlisch, M. Beye, M. Deppe, F. Hennies, M. Nagasono, E. Suljoti, W. Wurth, C. Gahl, K. Döbrich, A. Melnikov, New J. Phys. 10 (2008) 033004.
[14] S. Hellmann, K. Rossnagel, M. Marczynski-Bühlow, L. Kipp, Phys. Rev. B 79 (2009) 035402.
[15] K. Tiedtke, et al., New J. Phys. 11 (2009) 023029.
[16] S.M. Goldberg, C.S. Fadley, S. Kono, J. Electron Spectrosc. Relat. Phenom. 21 (1981) 285.
[17] C.S. Fadley, S.-H. Yang, B.S. Mun, J. Garcia de Abajo, in: W. Schattke, M.A. Van Hove (Eds.), Solid-State Photoemission and Related Methods: Theory and Experiment, Wiley–VCH Verlag, Berlin GmbH, 2003.
[18] J.-J. Yeh, I. Lindau, Atomic subshell photoionization cross sections and asymmetry parameters: $1 < Z < 103$, Atom Data Nucl. Data Tables 32 (1) (1985), with these results also available in graphical form at: http://ulisse.elettra.trieste.it/services/elements/WebElements.html.
[19] P.H. Scofield, Theoretical photoionization cross sections from 1 to 1500 keV, Lawrence Livermore Laboratory Report UCRL-51326, 1973, out of print, but also available at: http://www.physics.ucdavis.edu/fadleygroup/Scofield.CrossSections.UCRL51326.pdf.
[20] M.B. Trzhaskovskaya, V.I. Nefedov, V.G. Yarzhemsky, Atom. Data Nucl. Data Tables 77 (2001) 97;
M.B. Trzhaskovskaya, V.I. Nefedov, V.G. Yarzhemsky, Atom. Data Nucl. Data Tables 82 (2002) 257;
M.B. Trzhaskovskaya, V.K. Nikulin, V.I. Nefedov, V.G. Yarzhemsky, Atom. Data Nucl. Data Tables 92 (2006) 245.
[21] The NIST Electron Inelastic-Mean-Free-Path Database (http://www.nist.gov/srd/nist71.htm) and the NIST Electron Effective-Attenuation-Length Database (http://www.nist.gov/srd/nist82.htm), which is available at no charge.
[22] C.J. Powell, A. Jablonski, I.S. Tilinin, S. Tanuma, D.R. Penn, J. Electron Spectrosc. Relat. Phenom. 98 (1999) 1.
[23] S. Tanuma, C.J. Powell, D.R. Penn, Surf. Interface Anal. 37 (2005) 1;
S. Tanuma, C.J. Powell, D.R. Penn, Calculations of electron inelastic mean free paths. IX. Data for 41 elemental solids over the 50 eV to 30 keV range, to be published.
[24] M.P. Seah, S.J. Spencer, J. Electron Spectrosc. Relat. Phenom. 151 (2006) 178.
[25] M.O. Krause, Phys. Rev. 177 (1969) 151.
[26] R. Guillemin, O. Hemmers, D.W. Lindle, S.T. Manson, Radiat. Phys. Chem. 75 (2006) 2258.
[27] A. Jablonski, C.J. Powell, Surf. Int. Anal. 20 (1993) 771.
[28] C.S. Fadley, Prog. Surf. Sci. 16 (1984) 275;
A. Herrera-Gomez, J.T. Grant, P.J. Cumpson, M. Jenko, F.S. Aguirre-Tostado, C.R. Brundle, T. Conard, G. Conti, C.S. Fadley, J. Fulghum, K. Kobayashi, L. Köver, H. Nohira, R.L. Opila, S. Oswald, R.W. Paynter, R.M. Wallace, W.S.M. Werner, J. Wolstenholmer, Surf. Interf. Anal. 41 (2009) 840–857 (summary of the 47th IUVSTA Workshop on Angle-Resolved XPS, Riviera Maya, Mexico, March 2007).
[29] (a) The SESSA program by W. Smekal, W. S. M. Werner, C.J. Powell, and described in Surf. Interf. Anal. 37, 1059 (2005), includes all of the effects mentioned here except surface refraction due to V_0 and can be used over a very broad range of photon energies. Further information on this is available at: http://www.nist.gov/srd/nist100.htm and http://www.iap.tuwien.ac.at/~werner/sessa.html.;
(b) An alternative program emphasizing the exact shape of spectra as produced by inelastic scattering is QUASES™ by S. Tougaard, with information on this available at: http://www.quases.com/.
[30] (a) B.L. Henke, Phys. Rev A 6 (1972) 74;
(b) J. Chester, T. Jach, S. Thurgate, J. Vac. Sci. Technol. B 11 (1993) 1609;
(c) J. Kawai, S. Hayakawa, Y. Kitajima, K. Maeda, Y. Gohshi, J. Electron Spectrosc. Relat. Phenom. 76 (1995) 313;
(d) E. Landree, T. Jach, D. Brady, A. Karemcheti, J. Canterbury, W. Chism, A.C. Diebold, in: D.G. Seiler, A.C. Diebold, T.J. Shaffner, R. McDonald, W.M. Bullis, P.J. Smith, E.M. Secula (Eds.), Proceedings of the 2000 International Conference on Characterization and Metrology for ULSI Technology, American Institute of Physics, CP550, 2001, pp. 159–163.
[31] D.P. Woodruff, Rep. Prog. Phys. 68 (2005) 743.
[32] J.C. Woicik, E.J. Nelson, D. Heskett, J. Warner, L.E. Berman, B.A. Karlin, I.A. Vartanyants, Phys. Rev. 64 (2001) 125115.
[33] S.-H. Yang, B.S. Mun, N. Mannella, S.-K. Kim, J.B. Kortright, J. Underwood, F. Salmassi, E. Arenholz, A. Young, Z. Hussain, M.A. Van Hove, C.S. Fadley, J. Phys. Condens. Matter 14 (2002) L406.
[34] N. Mårtensson, P. Baltzer, P.A. Brühwiler, J.-O. Forsell, A. Nilsson, A. Stenborg, B. Wannberg, J. Electron Spectrosc. Relat. Phenom. 70 (1994) 117.
[35] E. Bauer, C. Koziol, G. Lilienkamp, T. Schmidt, J. Electron Spectrosc. Relat. Phenom. 84 (1997) 201.
[36] G. Schönhense, H.J. Elmers, S.A. Nepijko, C.M. Schneider, Adv. Imaging Electron Phys. 142 (2006) 160.
[37] A. Barinova, P. Dudina, L. Gregorattia, A. Locatellia, T.O. Menteşa, M.Á. Niñoa, M. Kiskinova, Nucl. Instrum. Methods A 601 (2009) 195.
[38] T. Wakita., T. Taniuchi, K. Ono, M. Suzuki, N. Kawamura, M. Takagaki, H. Miyagawa, F. Guo, T. Nakamura, T. Muro, H. Akinaga, T. Yokoyay, M. Oshima, K. Kobayashi, Jpn. J. Appl. Phys. 45 (2006) 1886.
[39] T. Kinoshita, E. Ikenaga, J.J. Kim, S. Ueda, M. Kobata, J.R. Harries, K. Shimada, A. Ino, K. Tamasaku, Y. Nishino, T. Ishikawa, K. Kobayashi, W. Drube, C. Kunz, Surf. Sci. 601 (2007) 4754.
[40] M.P. Seah, I.S. Gilmore, S.J. Spencer, J. Electron Spectrosc. Relat. Phenom. 104 (1999) 73.
[41] N. Mannella, S. Marchesini, A.W. Kaya, A. Nambu, T. Gresch, S.-H. Yang, B.S. Mun, J.M. Bussat, A. Rosenhahn, C.S. Fadley, J. Electron Spectrosc. Relat. Phenom. 141 (2004) 45.
[42] A.W. Kay, F.J. Garcia de Abajo, S.-H. Yang, E. Arenholz, B.S. Mun, N. Mannella, Z. Hussain, M.A. Van Hove, C.S. Fadley, Phys. Rev. B 63 (2001) 115119 (and earlier references therein).
[43] J.-M. Bussat, C.S. Fadley, B.A. Ludewigt, G.J. Meddeler, A. Nambu, M. Press, H. Spieler, B. Turko, M. West, G.J. Zizka, IEEE Trans. Nucl. Sci. 51 (2004) 2341.
[44] The multiple scattering program EDAC due to J. Garcia de Abajo for calculating photoelectron diffraction is available at: http://csic.sw.ehu.es/jga/software/edac/index.html, with the methodology behind it described in F.J. Garcia de Abajo, M.A. Van Hove, C.S. Fadley, Phys. Rev. B 63 (2001) 075404.
[45] C.S. Fadley, in: R.Z. Bachrach (Ed.), Synchrotron Radiation Research: Advances in Surface and Interface Science, Plenum Press, New York, 1992.
[46] S. Hagstrom, C. Nordling, K. Siegbahn, Phys. Lett. 9 (1964) 235.
[47] S.B. Hagstrom, Obituary of Kai Siegbahn, Phys. Today (November) (2008) 74.
[48] J. Hedman, P.F. Hedén, C. Nordling, K. Siegbahn, Phys. Lett. 29A (1969) 178.
[49] C.S. Fadley, D.A. Shirley, A.J. Freeman, P.S. Bagus, J.V. Mallow, Phys. Rev. Lett. 29 (1969) 1397;
C.S. Fadley, D.A. Shirley, Phys. Rev. A 2 (1970) 1109.
[50] F. De Groot, A. Kotani, Core Level Spectroscopy of Solids, CRC Press, Boca Raton, FL, 2008, Together with a user friendly program for calculating spectrum for some cases. http://www.anorg.chem.uu.nl/people/staff/FrankdeGroot/multiplet1.htm.
[51] K.S. Kim, Phys. Rev. B 11 (1975) 2177.
[52] P.H. Citrin, P. Eisenberger, G. Wertheim, Phys. Rev. Lett. 33 (1974) 965.
[53] A. Föhlisch, J. Hasselström, O. Karis, D. Menzel, N. Mårtensson, A. Nilsson, J. Electron Spectrosc. Relat. Phenom. 101–103 (1999) 303.
[54] U. Hergenhahn, J. Phys. B: Atom. Mol. Opt. Phys. 37 (2004) R89.
[55] K. Siegbahn, U. Gelius, H. Siegbahn, E. Olson, Phys. Lett. 32A (1970) 221.
[56] S.Å.L. Bergstrom, C.S. Fadley, Phys. Lett. 35A (1970) 375.
[57] C.S. Fadley, M.A. Van Hove, A. Kaduwela, S. Omori, L. Zhao, S. Marchesini, J. Phys. Condens. Matter 13 (2001) 10517 (and earlier references therein).
[58] (a) C. Westphal, J. Bansmann, M. Getzlaff, G. Schönhense, Phys. Rev. Lett. 63 (1989) 151;
(b) H. Daimon, T. Nakatani, S. Imada, S. Suga, Y. Kagoshima, T. Miyahara, Jpn. J. Appl. Phys. 32 (1993) L1480;
(c) A.P. Kaduwela, H. Xiao, S. Thevuthasan, C.S. Fadley, M.A. Van Hove, Phys. Rev. B 52 (1995) 14927.
[59] T. Nakatani, T. Matsushita, Y. Miyatake, T. Nohno, A. Kobayashi, K. Fukumoto, S. Okamoto, A. Nakamoto, F. Matsui, K. Hattori, M. Kotsugi, Y. Saitoh, S. Suga, H. Daimon, Prog. Surf. Sci. 71 (2003) 217.
[60] L. Baumgarten, C.M. Schneider, H. Petersen, F. Schäfers, J. Kirschner, Phys. Rev. Lett. 65 (1990) 492.
[61] S. Ueda, H. Tanaka, J. Takaobushi, E. Ikenaga, J.-J. Kim3, M. Kobata, T. Kawai, H. Osawa, N. Kawamura, M. Suzuki, K. Kobayashi, Appl. Phys. Express 1 (2008) 077003.
[62] J.G. Menchero, Phys. Rev. B 57 (1998) 993.
[63] R. Hashimoto, A. Chikamatsu, H. Kumigashira, M. Oshima, N. Nakagawa, T. Ohnishi, M. Lippmaa, H. Wadati, A. Fujimori, K. Ono, M. Kawasaki, H. Koinuma, J. Electron Spectrosc. Relat. Phenom. 144–147 (2005) 479.

[64] P. Le Fèvre, H. Magnan, D. Chandesris, J. Jupille, S. Bourgeois, A. Barbier, W. Drube, T. Uozumi, A. Kotani, Nucl. Inst. Methods Phys. Res. A 547 (2005) 176.
[65] P. Krüger, S. Bourgeois, B. Domenichini, H. Magnan, D. Chandesris, P. Le Fèvre, L. Floreano, A. Cossaro, A. Verdini, A. Morgante, Surf. Sci. 601 (2007) 3952; H. Magnan, P. Le Fèvre, D. Chandesris, P. Krüger, S. Bourgeois, B. Domenichini, A. Verdini, L. Floreano, A. Morgante, Phys. Rev. B 81 (2010) 085121.
[66] L. Plucinski, J. Minár, B.C. Sell, J. Braun, H. Ebert, C.M. Schneider, C.S. Fadley, Phys. Rev. B 78 (2008) 035108.
[67] C.S. Fadley, D.A. Shirley, Phys. Rev. Lett. 21 (1968) 980; C.S. Fadley, D.A. Shirley, NBS J. Res. 74A (1970) 543.
[68] Y. Baer, P.-F. Hedén, J. Hedman, M. Klasson, C. Nordling, K. Siegbahn, Solid State Commun. 8 (1970) 517.
[69] M.A. Vicente Alvarez, H. Ascolani, G. Zampieri, Phys. Rev. B 54 (1996) 14703.
[70] F.-C. Tang, X. Zhang, F.B. Dunning, G.K. Walters, Rev. Sci. Instrum. 59 (1988) 504.
[71] R. Frömter, H.P. Oepen, J. Kirschner, Appl. Phys. A 76 (2003) 869–871.
[72] F.U. Hillebrecht, R.M. Jungblut, L. Wiebusch, C. Roth, H.B. Rose, D. Knabben, C. Bethke, N.B. Weber, S. Manderla, U. Rosowski, E. Kisker, Rev. Sci. Instrum. 73 (2002) 1229; J. Graf, C. Jozwiak, A.K. Schmid, Z. Hussain, A. Lanzara, Phys. Rev. B 71 (2005) 144429; T. Okuda, Y. Takeich, A. Harasawa, I. Matsuda, T. Kinoshita, A. Kakizaki, Eur. Phys. J. Spec. Top. 169 (2009) 181–185.
[73] G. Busch, M. Campagna, P. Cotti, H.C. Siegmann, Phys. Rev. Lett. 22 (1969) 597.
[74] H.-J. Kim, E. Vescovo, S. Heinze, S. Blügel, Surf. Sci. 478 (2001) 193.
[75] J. Zegenhagen, C. Kunz (Eds.), Nucl. Inst. Methods A 547 (2005) (special journal issue dedicated to photoemission with hard X-rays).
[76] Programs and abstract archives from three recent hard X-ray photoemission workshops: http://haxpes2006.spring8.or.jp/program.html; http://ssg.als.lbl.gov/ssgdirectory/fedorov/workshops/index.html; http://www.nsls.bnl.gov/newsroom/events/workshops/2009/haxpes/.
[77] K. Kobayashi, Nucl. Inst. Methods A 601 (2009) 32.
[78] R.X. Ynzunza, R. Denecke, F.J. Palomares, J. Morais, E.D. Tober, Z. Wang, F.J. Garcia de Abajo, J. Liesegang, Z. Hussain, M.A. Van Hove, C.S. Fadley, Surf. Sci. 69 (2000) 459.
[79] M. Pickel, A.B. Schmidt, M. Donath, M. Weinelt, Surf. Sci. 600 (2006) 4176.
[80] F. Banfi, C. Giannetti, G. Ferrini, G. Galimberti, S. Pagliara, D. Fausti, F. Parmigiani, Phys. Rev. Lett. 94 (2005) 037601.
[81] A. Landers, T. Weber, I. Ali, A. Cassimi, M. Hattass, O. Jagutzki, A. Nauert, T. Osipov, A. Staudte, M.H. Prior, H. Schmidt-Böcking, C.L. Cocke, R. Dörner, Phys. Rev. Lett. 87 (2001) 013002.
[82] D.F. Ogletree, H. Bluhm, G. Lebedev, C.S. Fadley, Z. Hussain, M. Salmeron, Rev. Sci. Inst. 73 (2002) 3872.
[83] M.B. Salmeron, R. Schlögl, Surf. Sci. Rep. 63 (2008) 169–199.
[84] N. Mannella, A. Rosenhahn, C.H. Booth, S. Marchesini, B.S. Mun, S.-H. Yang, K. Ibrahim, Y. Tomioka, C.S. Fadley, Phys. Rev. Lett. 92 (2004) 166401.
[85] N. Mannella, C.H. Booth, A. Rosenhahn, B.C. Sell, A. Nambu, S. Marchesini, B.S. Mun, S.-H. Yang, M. Watanabe, K. Ibrahim, E. Arenholz, A. Young, J. Guo, Y. Tomioka, C.S. Fadley, Phys. Rev. B 77 (2008) 125134.
[86] F. Offi, N. Mannella, T. Pardini, G. Panaccione, A. Fondacaro, P. Torelli, S. Huotari, M.W. West, J.W. Mitchell, C.S. Fadley, Phys. Rev. B 77 (2008) 174422.
[87] K. Horiba, M. Taguchi, A. Chainani, Y. Takata, E. Ikenaga, D. Miwa, Y. Nishino, K. Tamasaku, M. Awaji, A. Takeuchi, M. Yabashi, H. Namatame, M. Taniguchi, H. Kumigashira, M. Oshima, M. Lippmaa, M. Kawasaki, H. Koinuma, K. Kobayashi, T. Ishikawa, S. Shin, Phys. Rev. Lett. 93 (2004) 236401.
[88] H. Tanaka, Y. Takata, K. Horiba, M. Taguchi, A. Chainani, S. Shin, D. Miwa, K. Tamasaku, Y. Nishino, T. Ishikawa, E. Ikenaga, M. Awaji, A. Takeuchi, T. Kawai, K. Kobayashi, Phys. Rev. B 73 (2006) 094403.
[89] M. VanVeenendaal, Phys. Rev. B 74 (2006) 085118.
[90] F. Offi, T. Pardini, G. Panaccione, C.S. Fadley, unpublished results from the ESRF VOLPE facility.
[91] Y.J. Kim, C. Westphal, R.X. Ynzunza, Z. Wang, H.C. Galloway, M. Salmeron, M.A. Van Hove, C.S. Fadley, Surf. Sci. 416 (1998) 68.
[92] Y.-N. Sun, Z.-H. Qin, M. Lewandowski, E. Carrasco, M. Sterrer, S. Shaikhutdinov, H.-J. Freund, J. Catal. 266 (2009) 359.
[93] M. Treier, P. Ruffieux, R. Fasel, F. Nolting, S. Yang, L. Dunsch, T. Greber, Phys. Rev. B 80 (2009) 081403.
[94] T. Greber, J. Wider, E. Wetli, J. Osterwalder, Phys. Rev. Lett. 81 (1998) 1654.
[95] J. Osterwalder, A. Tamai, W. Auwarter, M.P. Allan, T. Greber, Chimia 60 (2006) A795 (And earlier references therein).
[96] D.P. Woodruff, Surf. Sci. Rep. 62 (2007) 1.
[97] A. Winkelmann, C.S. Fadley, F.J. Garcia de Abajo, New J. Phys. 10 (2008) 113002.
[98] S. Ueda, A. Winkelmann, C. Papp, L. Plucinski, A. Gray, B. Balke, K. Kobayashi, C.S. Fadley, unpublished results from SPring8 beamline 15XU.
[99] M. Kobata, Igor Píš, H. Iwai, H. Yamazui, H.Takahashi, M. Suzuki, H. Matsuda, H. Daimon, K. Kobayashi, to be published.
[100] O.M. Käuttel, R.G. Agostino, R. Fasel, J. Osterwalder, L. Schlapbach, Surf. Sci. 312 (1994) 131.
[101] A. Szöke, in: D.T. Attwood, J. Boker (Eds.), AIP Conf. Proc. Number 147, AIP, New York, 1986, p. 361.
[102] S. Omori, Y. Nihei, E. Rotenberg, J.D. Denlinger, S. Marchesini, S.D. Kevan, B.P. Tonner, M.A. Van Hove, C.S. Fadley, Phys. Rev. Lett. 88 (2002) 5504.
[103] T. Greber, J. Phys.: Condens. Matter 13 (2001) 10561.
[104] M.J. Bedzyk, Encyclopedia Condens. Matter Phys. 6 (2005) 330 (And earlier references therein).
[105] S.-H. Yang, B.S. Mun, C.S. Fadley, Synchrotron Radiat. News 24 (2004) 17.
[106] S.-H. Yang, B.C. Sell, C.S. Fadley, J. Appl. Phys. 103 (2008) 07C519.
[107] S.-H. Yang, specially written computer program for standing-wave photoemission from multilayer structures, available on request, and to be published.
[108] S. Döring, F. Schonbohm, D. Weier, F. Lehmkuhler, U. Berges, M. Tolan, C.S. Fadley, C. Westphal, J. Appl. Phys. 106 (2009) 124906.
[109] B.C. Sell, Ph.D. Thesis, UC Davis, 2007.; B.C. Sell, S.-H. Yang, C.S. Fadley, unpublished results from Advanced Light Source beamline 4.0.2.
[110] S.-H. Yang, B.S. Mun, N. Mannella, A. Nambu, B.C. Sell, S.B. Ritchey, F. Salmassi, S.S.P. Parkin, C.S. Fadley, J. Phys.: Condens. Matter 18 (2006) L259.
[111] B. Klingenberg, F. Grellner, D. Borgmann, G. Wedler, Surf. Sci. 283 (1997) 13.
[112] B. Balke, C. Papp, S. Döring, U. Berges, S.H. Yang, B.C. Sell, D. Buergler, J.B. Kortright, C.M. Schneider, C. Westphal, C.S. Fadley, unpublished results from Advanced Light Source beamline 4.0.2.
[113] C.S. Fadley, Nucl. Inst. Methods A 547 (2005) 24.
[114] S. Döring, F. Schonbohm, U. Berges, C. Papp, B. Balke, M. Gorgoi, D. Buergler, C. Schneider, C.S. Fadley, unpublished results from the BESSY HIKE facility.
[115] C. Papp, B. Balke, S. Ueda, H. Yoshikawa, Y. Yamashita, S.L. He, C. Sakai, K. Kobayashi, D. Buergler, C. Schneider, C.S. Fadley, unpublished results from SPring8, beamline 15XU.
[116] C. Papp, B. Balke, S. Ueda, H. Yoshikawa, Y. Yamashita, K. Kobayashi, G. Conti, C.S. Fadley, unpublished results from Spring8 beamline 15XU.
[117] F. Kronast, R. Ovsyannikov, A. Kaiser, C. Wiemann, S.-H. Yang, D.E. Bürgler, R. Schreiber, F. Salmassi, P. Fischer, H.A. Dürr, C.M. Schneider, W. Eberhardt, C.S. Fadley, Appl. Phys. Lett. 93 (2008) 243116.
[118] A video of standing wave motion in a photoelectron microscope is available at: http://www.physics.ucdavis.edu/fadleygroup/.
[119] F. Kronast, C. Papp, A. Kaiser, C. Wiemann, A. Gray, S. Cramm, B. Balke, R. Schreiber, D. Buergler, C. Schneider, unpublished results from BESSY spin-polarized photoelectron microscope.
[120] A. Gray, S.-H. Yang, C.S. Fadley, unpublished results.
[121] A. Gupta, N. Darowski, I. Zizak, C. Meneghini, G. Schumacher, A. Erko, Spectrochim. Acta 62 (2007) 622.
[122] Z. Hussain, C.S. Fadley, S. Kono, L.F. Wagner, Phys. Rev. B 22 (1980) 3750; R.C. White, C.S. Fadley, M. Sagurton, Z. Hussain, Phys. Rev. B 34 (1986) 5226.
[123] K. Siegbahn, private communication, 2003.
[124] Y. Takata, private communication, 2006.
[125] Z. Yin, W.E. Pickett, unpublished results for Au.
[126] B. Nielsen, Z. Li, S. Lizzit, A. Goldoni, P. Hoffmann, J. Phys.: Condens. Matter 15 (2003) 6919 (and references therein).
[127] A. Yamasaki, A. Sekiyama, S. Imada, M. Tsunekawa, A. Higashiya, A. Shigemoto, S. Suga, Nucl. Inst. Methods Phys. Res. A 547 (2005) 136.
[128] M. Yano, A. Sekiyama, H. Fujiwara, T. Saita, S. Imada, T. Muro, Y. Onuki, S. Suga, Phys. Rev. Lett. 98 (2007) 036405 (and references therein).
[129] N. Kamakura, Y. Takata, T. Tokushima, Y. Harada, A. Chainani, K. Kobayashi, S. Shin, Phys. Rev. B 74 (2006) 045127.
[130] F. Venturini, J. Minar, J. Braun, H. Ebert, N.B. Brookes, Phys. Rev. B 77 (2008) 045126.
[131] J. Braun, Rep. Prog. Phys. 59 (1996) 1267.
[132] C. Papp, J. Minar, L. Plucinski, J. Braun, H. Ebert, C.S. Fadley, unpublished results.
[133] S. Ueda, K. Kobayashi, C. Papp, A. Gray, L. Plucinski, J. Minar, J. Braun, H. Ebert, C.S. Fadley, unpublished results from Spring8 beamline BL15XU.
[134] J. Osterwalder, T. Greber, S. Hüfner, L. Schlapbach, Phys. Rev. Lett. 64 (1990) 2683; G.S. Herman, T.T. Tran, K. Higashiyama, C.S. Fadley, Phys. Rev. Lett. 68 (1992) 1204.
[135] E. Rotenberg, A. Bostwick, private communication, 2005.
[136] L. Plucinski, A. Gray, C.S. Fadley, unpublished results.
[137] T. Schmidt, U. Groh, R. Fink, E. Umbach, Surf. Rev. Lett. 9 (2002) 223.
[138] H. Marchetto, U. Groh, T. Schmidt, R. Fink, H.J. Freund, E. Umbach, Chem. Phys. 178 (2006) 325.
[139] S. Lizzit, G. Zampieri, L. Petaccia, R. Larciprete, P. Lacovig, E.D.L. Rienks, G. Bihlmayer, A. Baraldi, P. Hofmann, http://arxiv.org/abs/1001.4761, submitted to Nat. Mater.
[140] T.D. Thomas, N. Berrah, J. Bozek, T.X. Carroll, J. Hahne, T. Karlsen, E. Kukk, L.J. Sæthre, Phys. Rev. Lett. 82 (1999) 1120.
[141] U. Hergenhahn, O. Kugeler, A. Ru1del, E.E. Rennie, A.M. Bradshaw, J. Phys. Chem. A 105 (2001) 5704.
[142] D. Nordfors, N. Martensson, A. Nilsson, (1986), unpublished results; A. Nilsson, J. Electron Spectrosc. Relat. Phenom 126 (2002) 3 (discussion of Figure 14).
[143] H.J. Ruppender, M. Grunze, C.W. Kong, Surf. Int. Anal. 15 (1990) 245.
[144] A. Baraldi, G. Comelli, S. Lizzit, M. Kiskinova, G. Paolucci, Surf. Sci. Rep. 49 (2003) 169.
[145] R. Denecke, Appl. Phys. A 80 (2005) 977 (and references therein).
[146] H. Bluhm, D. Frank Ogletree, C.S. Fadley, Z. Hussain, M. Salmeron, J. Phys. Condens. Matter 14 (2002) L227.
[147] S. Ghosal, J.C. Hemminger, H. Bluhm, B.S. Mun, E.L.D. Hebenstreit, G. Ketteler, D.F. Ogletree, F.G. Requejo, M. Salmeron, Science 307 (2005) 5709; M.A. Brown, R. D'Auria, I.F.W. Kuo, M.J. Krisch, D.E. Starr, H. Bluhm, D.J. Tobias, J.C. Hemminger, Phys. Chem. Chem. Phys. 10 (2008) 4778.
[148] H. Bluhm, M. Hävecker, A. Knop-Gericke, E. Kleimenov, R. Schlögl, D. Teschner, V.I. Bukhtiyarov, D.F. Ogletree, M.B. Salmeron, J. Phys. Chem. B 108 (2004) 14340.

[149] Y. Enta, Y. Miyanishi, H. Irimachi, M. Niwano, M. Suemitsu, N. Miyamoto, E. Shigemasa, H. Kato, Phys. Rev. B 57 (1998) 6294;
Y. Enta, Y. Miyanishi, H. Irimachi, M. Niwano, M. Suemitsu, N. Miyamoto, E. Shigemasa, H. Kato, J. Vac. Sci. Technol. A 16 (1998) 1716.
[150] Y. Enta, B.S. Mun, Y. Enta, M. Rossi, P.N. Ross, Z. Hussain, C.S. Fadley, K.-S. Lee, S.-K. Kim, Appl. Phys. Lett. 92 (2008) 012110;
M. Rossi, B.S. Mun, Y. Enta, C.S. Fadley, K.S. Lee, S.-K. Kim, H.-J. Shin, Z. Hussain, P.N. Ross Jr., J. Appl. Phys. 103 (2008) 044104.
[151] M.E. Grass, P.G. Karlsson, F. Aksoy, M. Lundqvist, B. Wannberg, B.S. Mun, Z. Liu, Z. Hussain, results from Advanced Light Source beamline 9.3.2, submitted to Rev. Sci. Inst.